Design and Development of a Smart, Self-contained, Portable Negative Pressure Wound Therapy Device.

by

Ashin Modak

Submitted to the Department of Mechanical Engineering
in partial fulfillment of the requirements for the degree of

Doctor of Philosophy in Mechanical Engineering

at the

MASSACHUSETTS INSTITUTE OF TECHNOLOGY

June 2018

Signature redacted

Author .....
Department of Mechanical Engineering
May 4, 2018

Signature redacted

Certified by .....
Ian W. Hunter
Hatsopoulos Professor of Mechanical Engineering
Thesis Supervisor

Signature redacted

Accepted by .....
Rohan Abeyaratne
Chairman, Department Committee on Graduate Students

Design and Development of a Smart, Self-contained, Portable Negative Pressure Wound Therapy Device.

by

Ashin Modak

Submitted to the Department of Mechanical Engineering
on May 4, 2018, in partial fulfillment of the
requirements for the degree of
Doctor of Philosophy in Mechanical Engineering

Abstract

Negative pressure wound therapy (NPWT) is a commonly used treatment in which the application of a low vacuum (-20kPa) is used to accelerate the recovery of chronic, hard-to-heal wounds. Costs of chronic wounds such as diabetic foot ulcers are estimated to be $25 billion, with 6.5 million patients being affected. Improving the portability and efficacy of NPWT devices will allow a larger migration of patients from hospital stays to at-home care. Current portable NPWT devices have severe limitations due to their size, inability to dynamically modulate pressure or handle large volumes of wound exudate. The work in this thesis was to develop a more portable NPWT device in which all functional components are self-contained within the bandage itself. To accomplish this goal, a soft-material, fuel-cell based actuator was designed and incorporated into a self contained, compact pumping mechanism. Additonally graphene-oxide barriers were designed to allow for fluid management at the wound site. The designed bandage was able to mantain negative pressure even at worst-case scenario leak rates (6.7×10^{-2} mL/s) and an exudate rate of 5.6×10^{-5} mL/s. The contributions from this thesis are a novel, soft-materials based actuator for use in biomedical applications and the further characterization of graphene-oxide barriers.

Thesis Supervisor: Ian W. Hunter
Title: Hatsopoulos Professor of Mechanical Engineering

Acknowledgments

I would like to first thank my family, who have constantly showered me with love over my 28 years. How they deal with such an ungrateful, good-for-nothing son and brother such as myself is beyond me, but I appreciate their efforts. To my parents, Pramod and Winaya Modak, thanks for taking such an interest in my life. I love how our relationship has changed over the years: I consider you two my oldest friends. As for my sister, Nina Sarika Modak, you are my favorite. I could go on and on about how much you inspire me, but I'm afraid it'll go to your head. If it were in fashion to dedicate a master's thesis, I would dedicate this to you, but alas, this is not the case.

Thanks to all of my friends. To everyone back home, I miss you terribly. Knowing that you all are rooting for me gives me the energy to put forth my best effort. To all my friends in Boston, thanks for enduring the complaining, yelling, nose-flicks, and general injuries that come with being my friend. You all keep me happy.

Thanks to all the mentors in my life: Sam Christensen, Alex Isbell, Jim Adam, and Jim Birdsong. Some of you I have thanked properly, some I haven't. Your influences in my adolescence shaped my values to what they are today. Thanks to Dr. Jenni Buckley and the rest of my colleagues at the Biomechancial Testing Facility. I realize now how special our time together was. Working with you all shook me out of my general undergraduate apathy and gave my education a direction and motivation. I hope one day I will be able to impact someone as positively as you all have with me.

Lastly, thanks to Professor Ian Hunter for both the opportunities and education that he and the rest of the BioInstrumentation Lab has provided. I came into this lab knowing very little about anything, especially mechanical engineering. Thanks to Dr. Adam Wahab, Dr. Brian Hemond, Dr. Bryan Ruddy, Dr. Cathy Hogan, Dr. Eli Paster, Dr. Ellen Chen, James White, Dr. Jean Chang, Dr. John Liu, and Dr. Seyed Mirvakili for mentoring and bringing me up to speed.

Contents

List of Figures

List of Tables

Chapter 1

Background

Negative Pressure wound therapy (NPWT) is a commonly used treatment for chronic, hard to heal wounds. The idea itself is quite simple. Suction (or negative pressure) is applied to a wound site so that wound healing would be improved. The first modern NPWT system, credited to Louis Argenta[1] was quite simple: a vacuum source (generally a pressure pump) is used to generate a very low vacuum (negative pressure) on the wound. Initial results showed this application of negative pressure to be successful in treating lower leg ulcers[2], and it has been shown to be twice as effective in closing chronic wounds such as diabetic leg ulcers[3],[4]. The use of NPWT has since been expanded to include many other applications such as post surgical wounds [5][6],abdominal wounds[7], and burns [8].

1.1 Mechanisms of operation

While initially proposed as a way to bring the edges of the wound closer together[1], the success of NPWT has since been attributed to four distinct mechanisms: macro-deformation, micro-deformation, excess fluid removal, and maintenance of a proper wound environment [9] (see Figure 1-1).

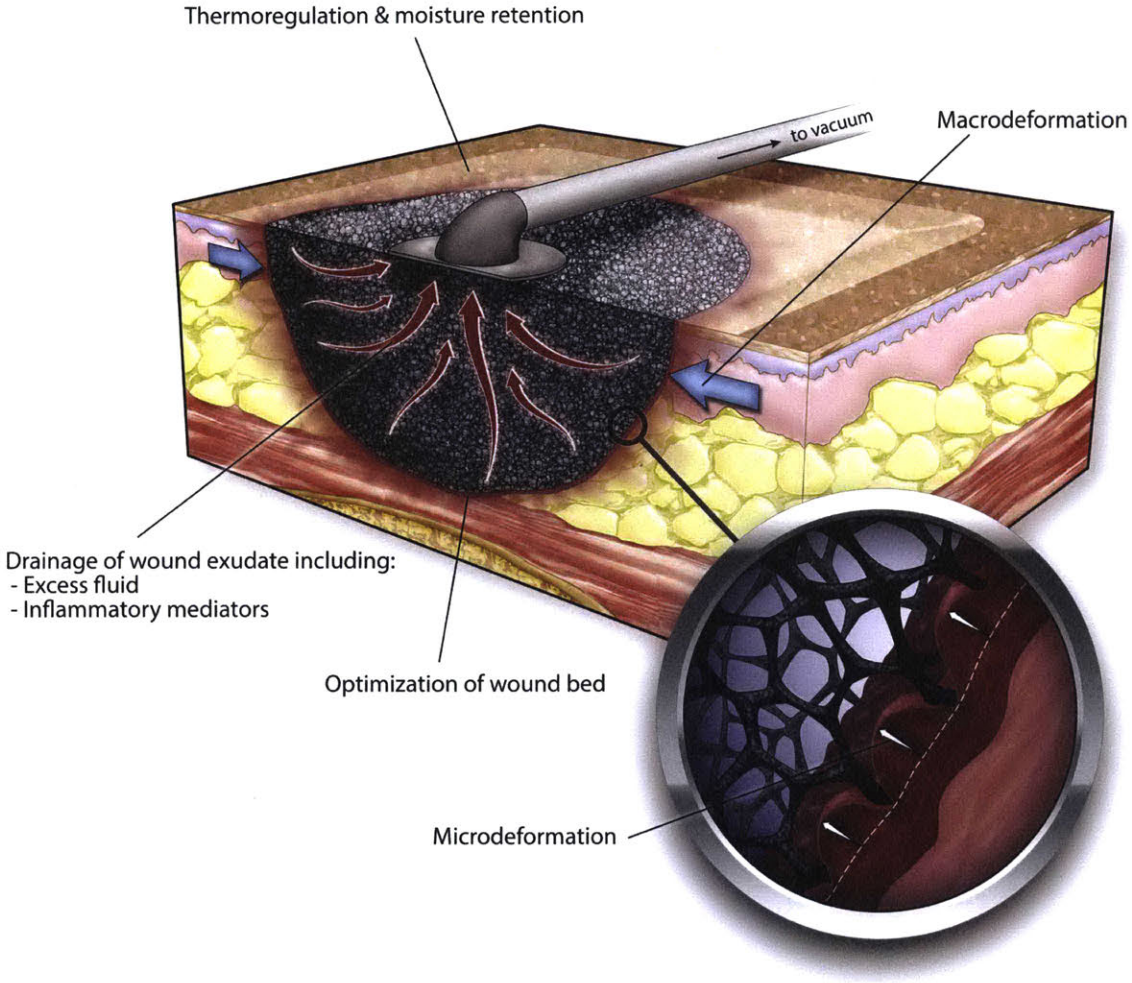

Figure 1-1: Different mechanisms of action of NPWT. NPWT aids wound healing via macro and micro deformation of the wound site, drainage of the wound bed, and moisture retention at the wound site. Image taken from [9]

1.1.1 Macro-deformation

On the most macro level, the contraction of the wound bed decreases the area of skin that has to be healed over. While the inherent tension in skin tissue will cause a wound to be stretched apart, application of negative pressure to the area will being the edges of the wound closer [9]. This effect is similar to the intent of surgical sutures in closing the wound area as much as possible.

1.1.2 Micro-deformation

On a more micro scale, the creation of a pressure difference will causes stresses at the wound interface. This results in more directed forces on the cells of the wound site, and these directed forces has been shown to increase cell proliferation, migration, and differentiation [9][10][11], meaning that wound healing will occur faster.

1.1.3 Fluid removal

Many wounds, especially chronic wounds, will secrete fluid (known as exudate) over time. As a negative pressure is applied, the resulting pressure gradient will begin to remove exudate from surrounding tissue. This has many compound effects. First, removal of fluid from surrounding tissue will reduce swelling and allow for easier closure of the wound. Additionally, less fluid pressure in the skin tissue will allow for higher blood flow through the microvasculature [2], which is a key component in delivery of the necessary wound healing factors. At the wound site, removal of excess fluid on the wound site will also prevent skin maceration, which would otherwise hinder wound healing. Finally, this removal of exudate will also remove potential factors inhibiting wound repair that can be found in chronic wounds.

1.1.4 Ideal Wound environment

Lastly, the device acts in the same way as a normal bandage: providing a protected, moist environment to promote wound healing. An ideal wound environment is both

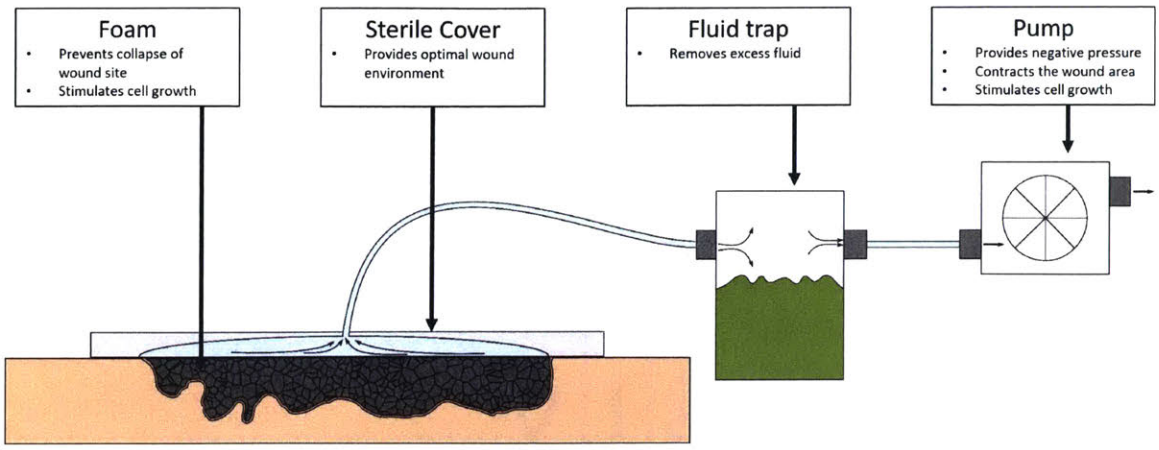

Figure 1-2: The main components of a NPWT device. A foam bed is kept inside the wound bed and covered with a sterile cover. A pump is used to create suction at the wound site, and excess exudate is caught inside a fluid trap.

sterile and will not allow for drying out of the wound. This function is similar to any bandage that is used as a wound covering.

1.2 Components of a NPWT System

A basic NPWT system can be broken into four components (see Figure 1-2) , each being used to provide one of the mechanisms of wound healing.

1.2.1 Pump

A pump, acting as a vacuum source, is the most essential part of a NPWT system, as it is the source of negative pressure generation for the device. This pumping mechanism is also used to remove fluid from the wound. While hospital vacuum lines have been used in the past to apply negative pressure, a dedicated pumping mechanism has been shown to be more reliable [12]. This pumping mechanism may be an actual pump[13][14], or mechanical devices such as a spring-piston assembly[15] or bellows-plunger system[16].

1.2.2 Fluid Trap

Traditionally a fluid trap is used to collect the exudate that is drawn from the wound site. This fluid trap is in line with the vacuum source so that the vacuum source will not be contaminated with exudate. This fluid trap may be either a simple canister or a fluid-absorbing gel [14].

1.2.3 Foam or Gauze

Foam and gauze serve multiple functions in the NPWT system. First, they prevent the wound from collapsing on itself when a negative pressure is applied. Secondly, they serve as a conduit for fluid transfer from the wound to the surface of the skin. Lastly, they serve as the interface on which micro-deformation of the wound occurs, and provide a directed stress for wound healing and cell differentiation.

1.2.4 Wound cover

The most basic function of a NPWT device is similar to any other bandage: it must provide a sterile cover to the wound. This cover must also prevent drying of the wound site to promote an ideal wound environment. Additionally, for NPWT this cover also often provides the seal between the device and the skin surface, which is critical to avoid air leaks into the wound site.

1.3 Recent Advances

While NPWT has shown to be successful in accelerating wound healing, advances have been made to further the overarching goal of NPWT: reducing the hospital costs associated with chronic wounds. Currently, costs of chronic wounds in the US alone are estimated to be $25 billion, effecting 6.5 million patients[17]. This goal of reducing this cost has been pursued by two avenues: incorporating advanced wound-healing features to devices to accelerate wound healing, and creating portable NPWT devices to allow patients to leave the hospital but still receive NPWT treatment.

1.3.1 Advanced Features

Various advanced features have been added to traditionally sized NPWT devices to accelerate wound healing. While these devices may still only be appropriate for in-patient therapy, the advanced are still able to accelerate wound healing and reduce hospital stays. These features include variable pressure therapy, wound cleaning, and wound sensing.

Variable pressure therapy

In lieu of continuous negative pressure therapy, recent advances have studied the use of variable or intermittent NPWT, in which the wound pressure is varied periodically. Variable pressure operation has been shown to improve wound healing [2][18][19][20][21], and it is hypothesized to be due to two mechanisms. First, intermittent relaxation of applied negative pressure allowed for greater blood flow in the surrounding region [2][18]. Additionally, variable pressure operation will induce dynamic variations in the micro-stresses exerted on the cell, which have been shown to further direct cell growth and differentiation[10][11]. In particular smooth, triangular waveforms (see Figure 1-3) have been found to be effective in stimulating wound growth without any discomfort of sudden pressure changes at the wound site. [19] Pressure variations have fallen in the range of 85-98 kPa at 0.001 to 0.005 Hz [2][18][19][20].

Wound Cleaning

While NPWT does succeed in managing a moist wound environment, it is often not successful in managing the bio-burden of the exudate, meaning that wound cleaning is necessary. Instillation of the wound with a cleansing fluid in combination with NPWT has been shown to greatly reduce bacterial load in chronic wounds [22] and up-regulate wound healing [23].

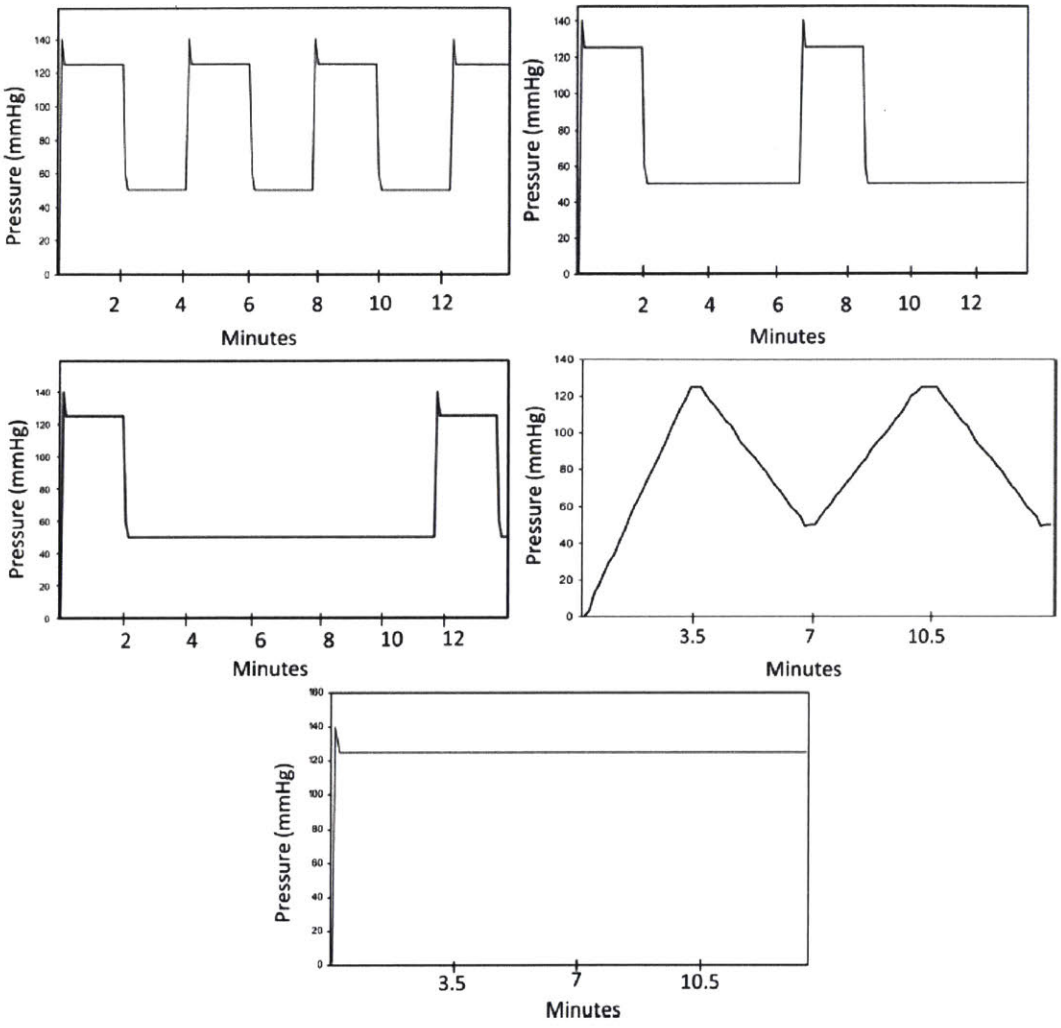

Figure 1-3: An example of various pressure profiles tested for NPWT by Dastouri, et al. Of the various pressure profiles, the triangular profile (middle right) was shown to be most effective in promoting angiogenesis at the wound site.Figure taken from [19].

Wound sensing

Future versions of NPWT have looked at incorporating sensors into the NPWT. Besides pressure sensing, the majority of sensors have focused on electrochemical techniques to measure wound pH [24][25], wound moisture [26][27][28], or the presence of bio-markers [29][30]. Sensing of wound pH and bio-markers are used to asses bacterial infection, while sensing of wound moisture is used to monitor dessication of the wound bed.

1.3.2 Portable Therapy

Another way of reducing hospital costs is to move NPWT from in-patient care to out-patient care. There are a handful of portable NPWT devices already available. The most compact are either electrically[31] or mechanically[32] powered, single use devices.These devices have been shown to be effective in treating chronic wounds [33][34], and have showed some innovations to reduces the size of the devices. While they still have external pumping mechanisms, some devices have been able to eliminate the use of a fluid trap through evaporation [35].

1.4 Current Shortcomings

While there have been many improvements to the efficacy of NPWT, there are still measurable improvement that can be made, particularly in the home-care setting. While the bulkier NPWT devices are able to provide advanced features such as wound pressure variation that can accelerate wound healing[18], these features are not present in portable devices. Inefficiencies and leaks within the pumps themselves increase the power requirements for even basic tasks such as maintaining wound pressure, resulting in rigid, bulky devices that cannot be self-contained within the bandage and have a limited battery life. Purely mechanical NPWT devices exist as well, but they are of similar size, and cannot provide any modulation either. The large size of the devices increase patient discomfort and embarassment due to the bulk of the pumping

mechanism/canister and the tangling of connective tubing [36], as well as the noise of the device. Furthermore, the inability of current devices to handle large exudate flow and provide variable pressure to the wound site limits the type of wounds for which they may be used. Additionally, lack of control on some of the devices caused device failure due to leakage [37].

By improving the portability of current NPWT devices, while also incorporating sensing and decision-making, we hope to create a smart NPWT bandage that will allow for effective self-regulation and home-use of these devices. While NPWT does accelerate wound healing, a full transition to home-use of these devices would further decrease hospital stays, bringing the down costs of chronic wounds significantly.

1.5 Aims of this thesis

The aims of this thesis is to develop a self-contained NPWT device that will allow for variable pressure application and higher exudate flow. Inclusion of variable pressure application and higher exudate flow will open up a larger class of wounds to portable NPWT, further reducing operating costs, while a self contained device will improve patient compliance by removing tubing and bulkiness.

1.6 Desired Metrics

A successful portable NPWT device must be discreet enough to not cause discomfort, while still being versatile, effect and robust in its treatment of various wound types. Investigation into these metrics will allow for development of Functional Requirements and Design Paramters for design.

1.6.1 Target Wounds Types

While there are numerous wounds that benefit from the use of NPWT, portable NPWT is not appopriate for many of them. For large sized the wounds, the patient will be immobile, and will be able to use a larger, bed-side device. Additionally,

wounds with a very large exudate rate will also not be ideal candidates for portable, self contained NPWT, as these high exudate levels will often require cleaning of the wound along with fluid removal. Target wound types must be speficied.

Venous Leg ulcers

Venous leg ulcers account for 40-70% of all chronic wounds in the lower extremities [38], and are caused by obstruction of venous blood flow [38]. The mean area of a venous leg ulcer is 1.5×10^{-3} m^2 [39] [40] (approximately 40 mm in diameter), and 20 mm deep [35] and they occur usually between the knee and the ankle [38]. These wounds are generally have moderate levels of wound exudate, up to 1.1 $mL/cm^2/24$ hours [35][41].

Diabetic Foot Ulcers

Diabetic foot ulcers, also known as neuropathic ulcers account for 15-25% of leg ulcers [38]. They are caused by excessive wear on the feet, due to a patient's loss of sensation in that region. The mean area of a diabetic foot ulcer is much smaller, $1.5 \times 10^{-4} m^2$ (approximately 15 mm in diameter), but they often occur in troublesome areas, such as the soles of the foot [38]. They generally exude very little.

Surgical Closure

NPWT has also been used in post surgical wounds to help contract the wound area more effectively. While the location of the wounds vary greatly, NPWT is often used for post surgical wounds with areas of $1.5\text{-}2.5 \times 10^{-3} m^2$ (up to 60 mm in diameter), and a depth of 10-20 mm [5].

1.6.2 Wound Volume

Based on all the wounds used, a wounds size of 20 mL was designed for. While some venous leg ulcers and ther high exudating wounds may be up to 45 mL [42], the value

of 20 mL will still represent a large fraction of venous leg ulcer, diabetic foot ulcers, and surgical incisions.

1.6.3 Wound Area

Wound area is important to define, as exudate level is based on wound area. A reasonable wound size is the median for leg ulcers, about 1.5 to 2 $\times$ 10^{-3} m^2[39]. This will be estimated as a circular wound 60 mm in diameter.

1.6.4 Desired Pressure

While a negative pressure of 125 mm Hg (15 kPa) is the standard for NPWT, pressures as low as -10 kPa (90 kPa absolute, or -70 mm Hg [35]) to -20 kPa (80 kPa absolute, or -150 mm Hg [43]) have been reported to be effective To be conservative a desired wound pressure of 80 kPa was chosen as a design parameter.

1.6.5 Advanced Features

In accordance with research with triangular pressure waveforms [19], the minimum variable pressure operation in a range of $\pm$ 10 kPa at a 0.003 Hz frequency was desired. Wound cleaning was outside the scope of the device. Based on the recomended amount of instillation fluid needed and period of wound cleaning performed [22], over 400 mL of instillation fluid is needed in one 24 hour cycle, precluding the possibility of any self-contained NPWT device. Wound pressure sensing will be incorporated to allow for closed loop pressure control, and humidity and temperature measurements will be used for wound monitoring. Only non-contact wound measurements were used in the current iterations of the device.

1.6.6 Fluid Rate

As mentioned earlier, exudate flow rate is based on wound area. While exudate flow can be as high as 1.17 $\times$ 10^{-2} mL/s [44], the target exudate flow will match that of

previous literature, of 47.2 $\times$ 10^{-5} mL/s [35] This is slightly higher than the expected exudate rate of venous leg ulcers, which are 2.78 to 27.8 $\times$ 10^{-5} mL/s r[41] for a 1.5 $\times$ 10^{-3} m^2 area.

1.6.7 Leak Rate

Leakage of air into the wound site, either through the skin, or the skin-bandage interface is the main source of NPWT failure. As will be seen later, leak rate is the primary factor to the power and energy requirements of a NPWT device. While well-sealed wounds have leak rates of 1.67 to 16.7 $\times$ 10^{-3} mL/s [31][16], difficult wound applications may be much worse: Leak rates as high of 50 $\times$ 10^{-3} mL/s [31] of air (STP) have been reported in case studies. While work has been done to reduce leak rates through the use of special sealants or skin adhesives, this was not taken into account. Not all wounds can be neatly sealed, and older patients in particular are sensitive to the use of such skin adhesives.

1.6.8 Bandage Size

While the Bandage itself can be quite large, it was estimated that a 75$\times$75$\times$15 mm size for all hard components would be sufficient in maintaining a small enough profile to be discreet enough for portable use.

1.6.9 Battery Size and Charging

A 13 kJ, (3.7 Wh) Lithium Polymer battery was chosen as the energy source for the device. The energy density of a 13 Lithium Polymer battery is 1-2.5 GJ/m^3, meaning that the volume of the necessary battery would be between 5 and 13 $\times$ 10^{-6} m^3 (or 50 mm by 50 mm by 5 mm). While the patient is expected to be mobile, a 24 hour battery life was deemed sufficient, as the patient would be able to swap batteries or recharge the device every evening without worry. For comparison, current portable NPWT devices have battery life of about 9 hours [45], so a 24 hour battery life was deemed acceptable.

Metric	Functional Requirements	Design Parameters
Wound Types	Venous Leg Ulcers Diabetic Foot Ulcers Small Surgical Closures	20 mL volume 50 mm diameter
Desired Negative Pressure	Full range	-10 kPa to -20 kPa
Advanced Features	Variable Pressure	± 10 kPa at 0.003 Hz
Fluid Rate	Low to moderately high	2.78 to 27.8 $\times$ 10^{-5} mL/s
Air Leak Rate	Low to moderately high	1.67 to 50.0 $\times$ 10^{-3} mL/s
Battery Size and Life	1 day	13 kJ LiPo for 24 hours
Bandage Size	Low Profile	75 mm $\times$ 75 mm $\times$ 15 mm
Total Weight	Light (less than phone)	$<$ 100 g

Table 1.1: Summary of Functional Requirements and Design Parameters for the Bandage

1.7 Proposed strategy

A self contained NPWT device must be able to combine vacuum generation and fluid handling, two normally external components, into the sealing layer of the bandage itself. As these are the two sources of bulkiness of the NWPT device, this will be the two components that this thesis will focus on improving.

Chapter 2

Physics of NPWT

The most critical module of any portable negative pressure device will be the pump, as it is what will be generating the negative pressure on the wound bed. To better choose the optimal type and size of this pump, it is helpful to look at the energy requirements necessary.

2.1 Energy requirements of the pump

To get a better idea what the energy requirements the NPWT pump must be able to provide, an abstract model of a wound bed in conjunction with a pump is constructed. At any instant, the amount of work the pump must perform is

$$W = [P_{atm} - P_w(V_{rem})]dV_{rem}, \tag{2.1}$$

where V_w is defined as the wound volume, P_w is the pressure at the wound site, P_{atm} is the atmospheric pressure, and dV_{rem} is defined as the volume of gas as measured at the exit of the pump (assumed to be atmospheric pressure).

The pump will be able to reduce the pressure at the wound site by removing gas molecules from the wound site and expelling them into the atmosphere. We can express the the moles of gas that have been removed from the wound site, dn as a

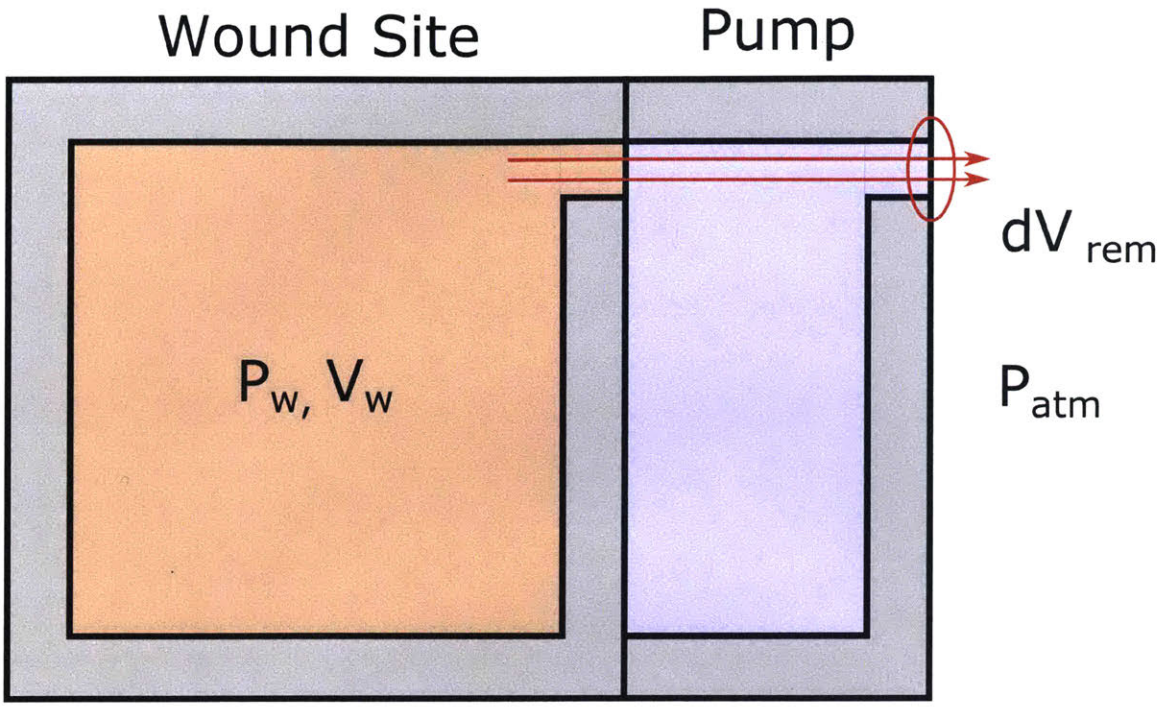

Figure 2-1: A wound of volume V_w is at a pressure P_w, because of a pump. The volume of gas that is removed instantaneously by the pump, dV_{rem}, is measured at the outlet, which is at atmospheric pressure.

function of the volume of gas removed, dV_{rem}:

$$dn = \frac{P_{atm} * dV_{rem}}{RT}, \tag{2.2}$$

where R is the ideal gas constant, and T is the temperature of the system. Assuming a constant wound volume, the total work necessary to reduce the pressure of the wound site to the desired pressure, P_{wdes}, will be

$$W = \int_0^{n_{tot}} [P_{atm} - P_w(n_{rem})] \frac{RT}{P_{atm}} dn, \tag{2.3}$$

where. n_{tot} is the total moles of gas that must be removed from the wound site, and n_{rem} is the moles of gas that has already been removed. n_{tot} is defined as

$$n_{tot} = \frac{(P_{atm} - P_{wdes})V_w}{RT}. \tag{2.4}$$

Additionally, we can define P_w as a function of n_{rem}:

$$P_w = \frac{P_{atm}V_w - n_{rem}RT}{V_w}. \tag{2.5}$$

Plugging into the integral gives the total work necessary to reduce the wound site to the desired pressure as

$$W = \int_0^{n_{tot}} [P_{atm} - \frac{P_{atm}V_w - n_{rem}RT}{V_w}] \frac{RT}{P_{atm}} dn. \tag{2.6}$$

Solving this equations gives us

$$W = \frac{(n_{tot}RT)^2}{2P_{atm}V_w}, \tag{2.7}$$

which solving this equations gives us

$$W = \frac{(P_{atm} - P_{wdes})^2 V_w}{2P_{atm}}. \tag{2.8}$$

To reduce the pressure of the wound with volume V_w= 20 mL from atmospheric pressure to P_{wdes}=80 kPa will only need 0.04 J.

While this value is small, air leaks in the wound site cause the energy load to be much higher. The power, **P**, needed to maintain a specific pressure P_{wdes} while allowing for an air leak $\dot{V}_{leak}$, will be

$$\mathbf{P} = P_{wdes}\dot{V}_{leak}. \tag{2.9}$$

In the worst case scenario of air leakage ($\dot{V}_{leak}$= 50.0 $\times$ 10^{-3} mL/s), the power required is 0.1 W, and the energy required for 24 hours of operation will be 86.4 J. We can solve for the necessary electromechanical efficiency, n_{mech} of the pump by comparing this energy to our supplied energy

$$n_{mech} = \frac{W_{charge}}{E_{stor}}, \tag{2.10}$$

where W_{charge} is the amount of work that must be done between charges, and E_{stor} is

the amount of stored energy available. For a 13 kJ battery and 24 hour charge cycle, this will mean that the pumping efficiency must be 0.6%. In addition the pump must be able to provide in the worst case scenario 0.1 W of power.

2.2 Other Pump Considerations

Other pump considerations include both its size (height and footprint) as well as size. Since this pump will be self contained within the bandage, it must be small: a bounding box of 75 mm $\times$ 75 mm $\times$ 10 mm was chosen. Additionally, because this pump will be part of the bandage, it would be ideal if this pump be 10 grams or less, so that the weight will not be noticeable by the patient. Lastly, the pump should be operable at low voltages, ($<$4.2 V) so that it is easily able to interface with a rechargeable lithium battery, and will not accidentally short in the possibly conductive wound environment.

2.3 Pump comparisons

Existing pumping mechanisms on portable negative pressure therapy devices have been compared below. The three types of pumping mechanisms were a electromagnetic diaphragm pump [46][47], a piezoelectric diaphragm pump [48] and a passive constant force spring pump[15].

Metric	Desired Quality	Electromagnetic Pump	Piezoelectric Pump	Spring-Piston Assembly
Mechanical Efficiency	>0.6%	32%	0.4%	-
Mechanical Power	> 1 mW	98 mW	0.8 mW	-
Footprint (rigid components)	< 75 mm × 75 mm	20.7 mm × 32 mm	75 mm × 75 mm	50 mm × 150 mm
Profile	< 10 mm	13.15 mm	3.8 mm	30 mm
Weight	<10 g	11 g	2 g	85 g
Controllability	Closed-Loop and Bidirectional	Needs one for each direction	Needs one for each direction	No
Operating Voltage	< 4 .2 V	< 4 V	250 V	-

Table 2.1: Comparison of various pumps being used for NPWT Electromagnetic pump specifications was from Parker[46], Piezoelectric pump specifications were from Bartels Mikrotechnik[48], and sprint-piston assembly was from SNAP system [15]

As can be seen in Table 2.1, all pumps exhibited a few short comings. Neither the electromagnetic or piezoelectric pumps can provide variable pressure wound therapy without requiring a second device. Additionally the electromagnetic pump was too large for our requirements, and the piezoelectric pump cannot provide enough power at high leak rates. The passive constant-force-spring pump is too large, and does not provide the opportunity for closed loop control.

2.4 An in depth pump model

To get a better idea of why no pump available is able to satisfy the functional requirements, the abstract wound model from before has been expanded to now include a positive displacement pump. A detailed look at the forces and energy requirements through this process will elucidate sources of inefficiency.

The wound volume from before is now in conjunction with a positive displacement pump, which has some stroke volume V_p, and piston area A_p. There are two check valves between the pump and the atmosphere, and the wound bed and the pump, with cracking pressures of P_{crack1}, and P_{crack2} respectively. The pump is actuated by an actuator that can travel from height h_0 to h_{max}, and supplies a force F through an area A_c.

Generally, the force supplied by the actuator will be at any particular height, h will be

$$F = P_{pump}(h)A_p - P_{atm}(A_p - A_c), \tag{2.11}$$

and the general equation for work ,W, done by as the actuator moves from h0 to hf will be

$$W = \int_{h_0}^{h_f} P_{pump}(h)A_p - P_{atm}(A_p - A_c)dh. \tag{2.12}$$

There are four regions of operation of this pump (see Figure 2-3). 1) The pump is pushing forward and creating enough pressure until the cracking pressure of the check valve 1. 2) After check valve 1 is opened, the pump will push out air in the chamber

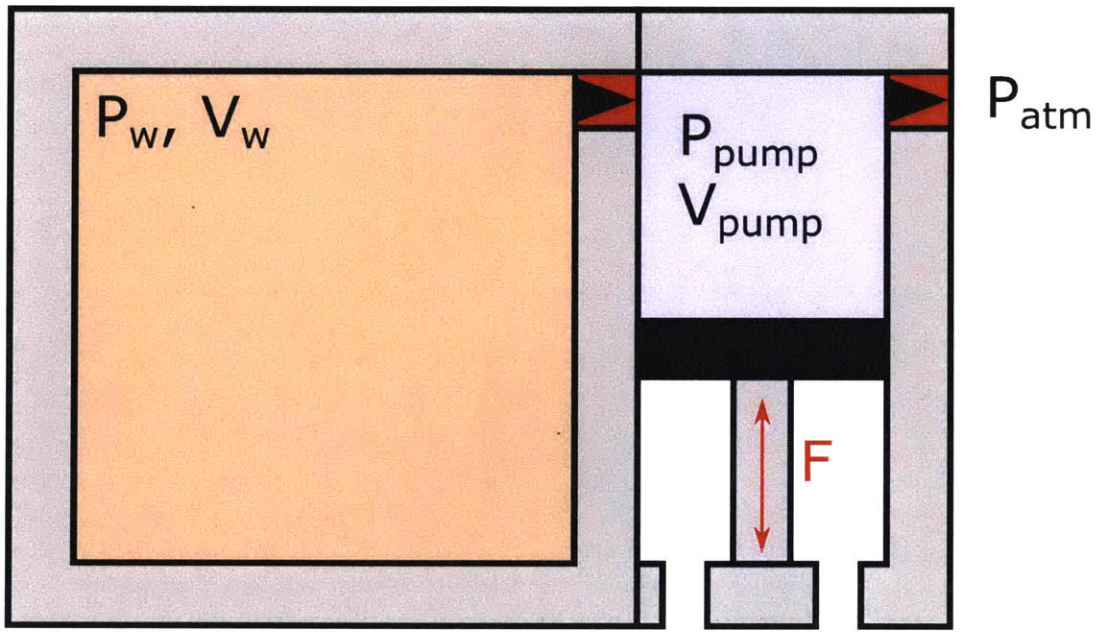

Figure 2-2: A wound of volume V_w is at a pressure P_w. When the pump extends, the pressure of the reciprocating pump, P_{pump} in the pump chamber V_{pump} will become larger than atmospheric pressure P_{atm} and air will flow through the check valve 1 into the atmosphere.Next, when the pump retracts, P_{pump} in the pump chamber V_{pump} will become less than P_w, and air will flow through check valve 2 into the pump chamber.

until it is fully extended. 3) After being fully extended, the pump will retract until it reduces pressure enough such that it overcomes the cracking pressure of check valve 2. 4) After check valve 2 is opened, the pump will continue to retract until it is either fully retracted, or it has reached the desired wound pressure.

2.4.1 Region 1

During this case, the volume in the chamber is decreasing as a function of the pump travel, h. This will cause the pressure in the pump to increase as follows:

$$P_{pump}(h) = P_{atm}\frac{(h_{max} - f_p h_0)}{(h_{max} - f_p h)}, \tag{2.13}$$

where h_{max} is the maximum extension of the pump, and h_o is the initial position of the pump, and f_p is the "space filling efficiency" of the pump (A standard srying in piston assembly has a efficiency of 1, while a telescoping mechanism may have a lower efficiency). Pressure will increase until the pump reaches a position h_1, at which the pressure difference between the pump and the atmosphere is greater than the cracking pressure of the check valve. This position, h_1 will be:

$$h_1 = \frac{1}{f_p}[h_{max} - \frac{P_{atm}}{P_{atm} + P_{crack1}}(h_{max} - f_p h_0)], \tag{2.14}$$

and the total work in this region will be

$$W_1 = -P_{atm}(A_p - A_c)(h_1 - h_0) + A_p(h_{max} - f_p h_0)P_{atm} ln(\frac{h_{max} - f h_0}{h_{max} - f_p h_1}), \tag{2.15}$$

which will simplify to

$$W_1 = -P_{atm}(A_p - A_c)(h_1 - h_0) + A_p(h_{max} - f_p h_0)P_{atm} ln(\frac{P_{atm} + P_{crack1}}{P_{atm}}) \tag{2.16}$$

2.4.2 Region 2

In this region, the pressure of the pump chamber is constant, as it must maintain a pressure differential higher than the cracking pressure of the check valve to expel

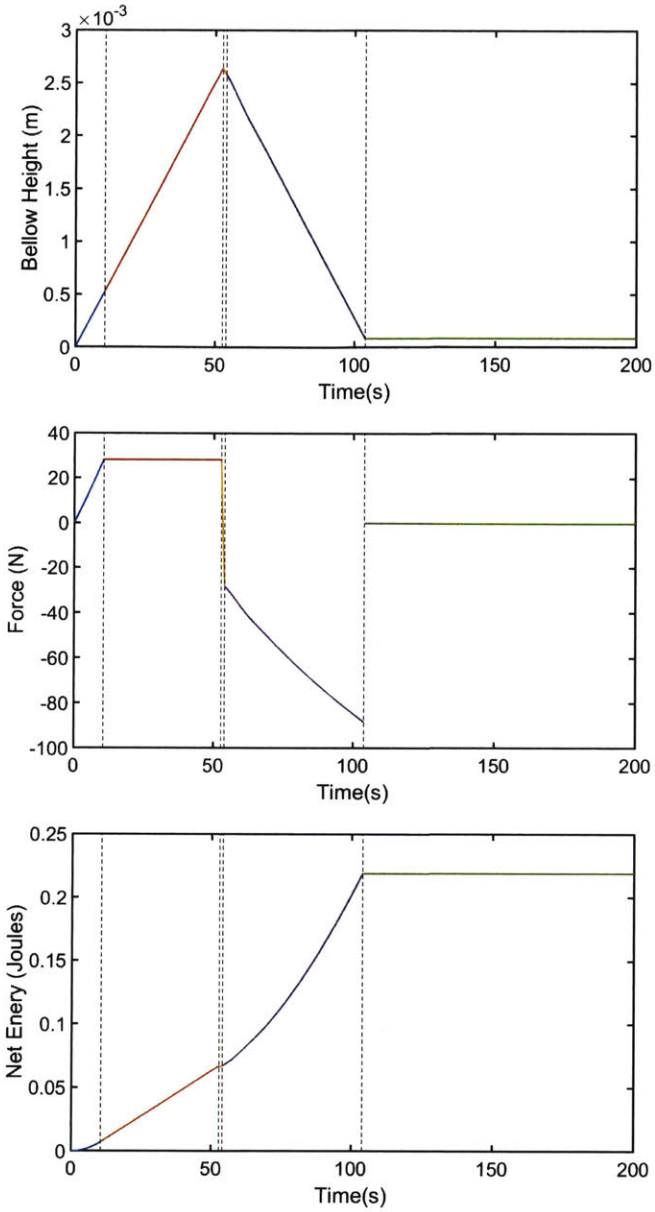

Figure 2-3: In region 1 (blue) pressure in the pumping chamber is increased until it reaches the cracking pressure of check valve 1, at which the pump enters region 2 (orange). After reaching the maximum height, the pump is retracted (region 3, purple) until the pressure within the pump falls enough for air to flow through check valve 2 into the pump (region 4, orange). This continues until the wound bed reaches the desired pressure, at which the pressure is held constant (orange). For the simulation used, a perfectly sized actuator was simulated for a wound volume of 20 mL, with 90% space filling efficiency, and a point force being applied by the pumping actuator. Cracking pressure of all check valves were 10 kPa

air. In reality, this pressure will also be related to the flow rate desired, which will be especially noticable when pumping fluids such as water. However for air, the first order model will ignore those contributions. The pressure in the pump can be defined as

$$P_{pump}(h) = (P_{atm} + P_{crack1}) * A_p \tag{2.17}$$

and the pump will continue to push forward until it reaches a maximum height, h_2, which may be slightly less than h_{max} due to manufacturing tolerances. This would mean that the total work in this region will be

$$W_2 = -P_{atm}(A_p - A_c)(h_2 - h_1) + (P_{atm} + P_{crack1})(A_p)(h_2 - h_1), \tag{2.18}$$

or

$$W_2 = -P_{atm}(A_p - A_c)(h_2 - h_1) + (P_{atm} + P_{crack1})(A_p)(h_2 - \frac{1}{f_p}[h_{max} - \frac{P_{atm}}{P_{atm} + P_{crack1}}(h_{max} - f_p h_0)]). \tag{2.19}$$

2.4.3 Region 3

Once the pump has finished extending, it will begin to retract. Now the pressure in the pump chamber will start to decrease from its initial pressure, $P_{atm} + P_{crack1}$ as a function of the position of the pump.

$$P_{pump}(h) = (P_{atm} + P_{crack1})\frac{(h_{max} - f_p h_2)}{(h_{max} - f_p h)}. \tag{2.20}$$

This will continue until it reaches a height, h_3, at which the pressure in the chamber will be low enough to overcome the cracking pressure of the check valve between the wound and the pump (check valve 2)

$$h_3 = \frac{1}{f_p}[h_{max} - \frac{P_{atm} + P_{crack1}}{P_{wi} - P_{crack2}}(h_{max} - f_p h_2)], \tag{2.21}$$

where P_{wi} will be the initial pressure state of the wound for the ith stroke of the pump. The total work in this region will be

$$W_3 = -P_{atm}(A_p - A_c)(h_3 - h_2) + A_p(h_{max} - f_p h_2)(P_{atm} + P_{crack1})ln(\frac{h_{max} - f_p h_2}{h_{max} - f_p h_3}). \tag{2.22}$$

which will simplify to

$$W_3 = -P_{atm}(A_p - A_c)(h_3 - h_2) + A_p(h_{max} - f_p h_2)(P_{atm} + P_{crack1})ln(\frac{P_{wi} - P_{crack2}}{P_{atm} + P_{crack1}}). \tag{2.23}$$

2.4.4 Region 4

In this region, the pump and wound bed are in fluid communication with each other, meaning that pulling back on the piston will decrease the pressure in both. The difference between pump pressure and the wound pressure must always be greater than the cracking pressure of the check valve, meaning that

$$P_{pump}(h) = P_w(h) - P_{crack2}. \tag{2.24}$$

While the pump is retracting the reduce pressure, gas molecules will move from the wound bed to the pump chamber. However, the total number of gas molecules will always be constant, meaning that

$$P_{pump}(h)A_p(h_{max} - f_p h) + (P_{pump} + P_{crack2})V_w = (P_{wi} - P_{crack2})A_p(h_{max} - f_p h_3) + P_{wi}V_w, \tag{2.25}$$

or

$$P_{pump}(h) = (P_{wi} - P_{crack2})\frac{V_w + A_p(h_{max} - f_p h_3)}{V_w + A_p(h_{max} - f_p h)}. \tag{2.26}$$

The piston will continue to retract until it either reaches it original starting position, h_0, or it reaches the desired wound pressure and will stop at position h_f. h_f

can be expressed as

$$h_f = \frac{1}{f}[\frac{V_w}{A_p} + h_{max} - \frac{P_{wi} - P_{crack2}}{P_{wdes} - P_{crack2}} \frac{V_w + A_p(h_{max} - f_p h_3)}{A_p}]. \tag{2.27}$$

The total work in this region will be

$$W_4 = -P_{atm}(A_p - A_c)(h_f - h_3) + [V_w + A_p(h_{max} - f h_3)](P_{wi} - P_{crack2}) ln(\frac{V_w + A_p(h_{max} - f_p h_3)}{V_w + A_p(h_{max} - f_p h_f)}, \tag{2.28}$$

which will simplify to

$$W_4 = -P_{atm}(A_p - A_c)(h_f - h_3) + [V_w + A_p \frac{P_{atm} + P_{crack1}}{P_{wi} - P_{crack2}}(h_{max} - f_p h_2)](P_{wi} - P_{crack2}) ln(\frac{P_{wdes} - P_{crack2}}{P_{wi} - P_{crack2}}). \tag{2.29}$$

2.4.5 Total Energy

The total energy over 1 stroke will be

$$W_{stroke} = W_1 + W_2 + W_3 + W_4, \tag{2.30}$$

which will equate to

$$\begin{aligned} W_{stroke} = & -P_{atm}(A_p - A_c))(h_f - h_0) \\ & + A_p(h_{max} - f_p h_0) P_{atm} ln(\frac{P_{atm} + P_{crack1}}{P_{atm}}) \\ & + A_p(P_{atm} + P_{crack1})(h_2 - \frac{1}{f_p}[h_{max} - \frac{P_{atm}}{P_{atm} + P_{crack1}}(h_{max} - f_p h_0)]) \\ & + A_p(h_{max} - f_p h_2)(P_{atm} + P_{crack1}) ln(\frac{P_{wi} - P_{crack2}}{P_{atm} + P_{crack1}}) \\ & + [V_w + A_p \frac{P_{atm} + P_{crack1}}{P_{wi} - P_{crack2}}(h_{max} - f_p h_2)](P_{wi} - P_{crack2}) ln(\frac{P_{wdes} - P_{crack2}}{P_{wi} - P_{crack2}}). \end{aligned} \tag{2.31}$$

While this equation is unwieldy, it can be used as a good starting point for analysis. Simplifications of this equation will allow for design decisions to be made. First, for a perfectly sized pump, meaning that its final stroke position is the same as its initial

stroke position with full extension ($h_0 = h_f$ and $h_2 = h_{max}$), the equation will simplify to

$$\begin{aligned} W_{stroke} = \; & A_p(h_{max} - f_p h_0) P_{atm} ln(\frac{P_{atm} + P_{crack1}}{P_{atm}}) \\ & + A_p(P_{atm} + P_{crack1})(h_{max} - \frac{1}{f}[h_{max} - \frac{P_{atm}}{P_{atm} + P_{crack1}}(h_{max} - f_p h_0)]) \\ & + A_p h_{max}(1 - f_p)(P_{atm} + P_{crack1}) ln(\frac{P_{wi} - P_{crack2}}{P_{atm} + P_{crack1}}) \\ & + [V_w + A_p h_{max} \frac{P_{atm} + P_{crack1}}{P_{wi} - P_{crack2}}(1 - f_p)](P_{wi} - P_{crack2}) ln(\frac{P_{wdes} - P_{crack2}}{P_{wi} - P_{crack2}}). \end{aligned} \tag{2.32}$$

This implies that the total energy will be dependent on eight variables: the cracking pressure of the two check valves, P_{crack1} and P_{crack2}, the final desired pressure and volume of the wound site,P_{wdes} and V_w, the initial dead volume of the pump $A_p h_0$, the final maximum volume of the pump $A_p h_{max}$ and the space filling factor of the pump, f. Lastly, this equation must be solved for the total number of strokes needed to reach pressure.

It is important to note that as the amount of strokes needed increases, the energy required will decrease and approach the theoretical limit calculated earlier(see Figure 2-4). However, even a modest cracking pressure will skew the inequality such that a single stroke pump would be more efficient. The effect will be explored in the following sections.

2.5 Reasons for inefficiency

Thus far, the model created has still been fairly idealized. There are many sources of inefficiencies that will could affect the energy cost of the system, and can be used to inform design decisions. A closer look at the reasons for inefficiency will help determine ideal design of a NPWT pump.

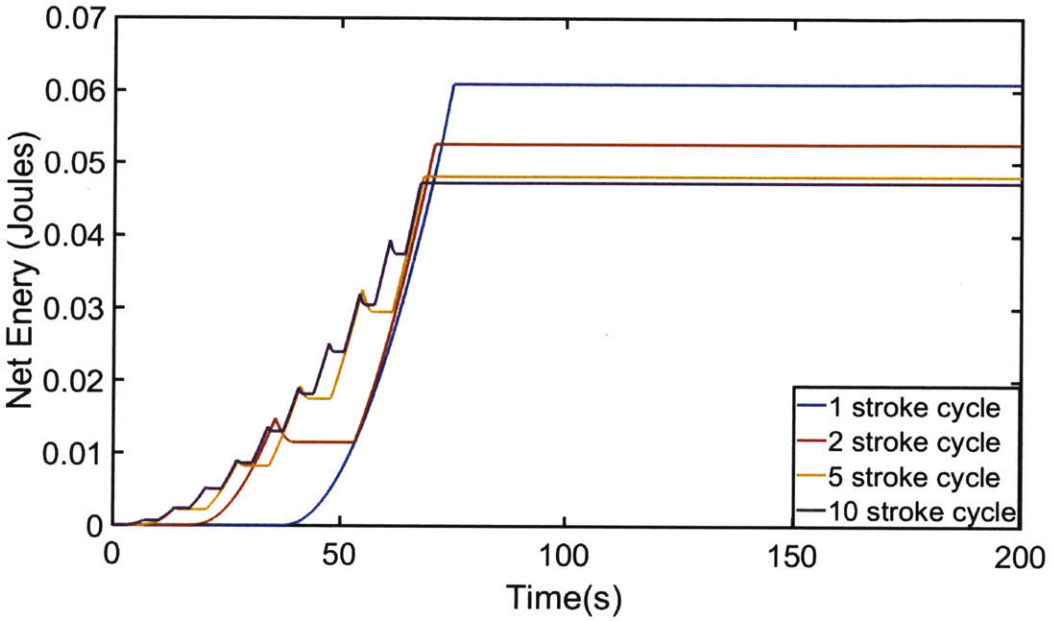

Figure 2-4: A simulation of how varying stoke length affects total energy required to reduce pressure wound pressure to 80 kPa. A perfectly sized actuator was simulated for a wound volume of 20 mL, with perfect space filling, and a point force being applied by the pumping actuator. Cracking pressure of all check valves were 0

2.5.1 Leak Rates

As mentioned before, leakage ($\dot{V}_{leak}$) into the bandage creates a dramatic increase in the amount of energy needed to maintain pressure. However, it will also affect the amount of energy needed to reduce pressure, as the effective wound volume, V_{weff} will be larger than expected. Depending on how many strokes are necessary to reduce pressure, the effective volume that must be generated will be

$$V_{weff} = kT\dot{V}_{leak} + V_w, \tag{2.33}$$

where T is the period of one stroke of the pump, and k is the fraction of the stroke cycle that a leak will be present. This will be 0.5 for a single stroke pump, and will approach 1 for a multiple stroke pump. The faster the pump can create the desired negative pressure, the less effective volume will be created. Additionally the pump must be faster than the leak rate of the wound for any negative pressure to be generated at all.

2.5.2 Check valves

Check valves are necessary for the pump to be able to continuously generate a negative pressure. However, they are a cause of inefficiencies. There are three ways in which a check valve can contribute to inefficiency: cracking pressure, leakage, and response time. Additionally, the presence of a check valve between the wound and the pump chamber (check valve 2) eliminates the ability to provide variable pressure with just one pump.

It be seen from Equation 2.34, the cracking pressure of the check valve is an extra force our actuator must work against when traveling along its stroke. The two solutions to this problem are to first minimize the cracking pressure as much as possible, and to eliminate the check valve between the wound and pump chamber (check valve 2) from the system. This offers a number of advantages: First it can be seen that check valve 2 contributes significantly to the additional energy cost of the system. Secondly, removing check valve 2 allows direct bidirectional communication

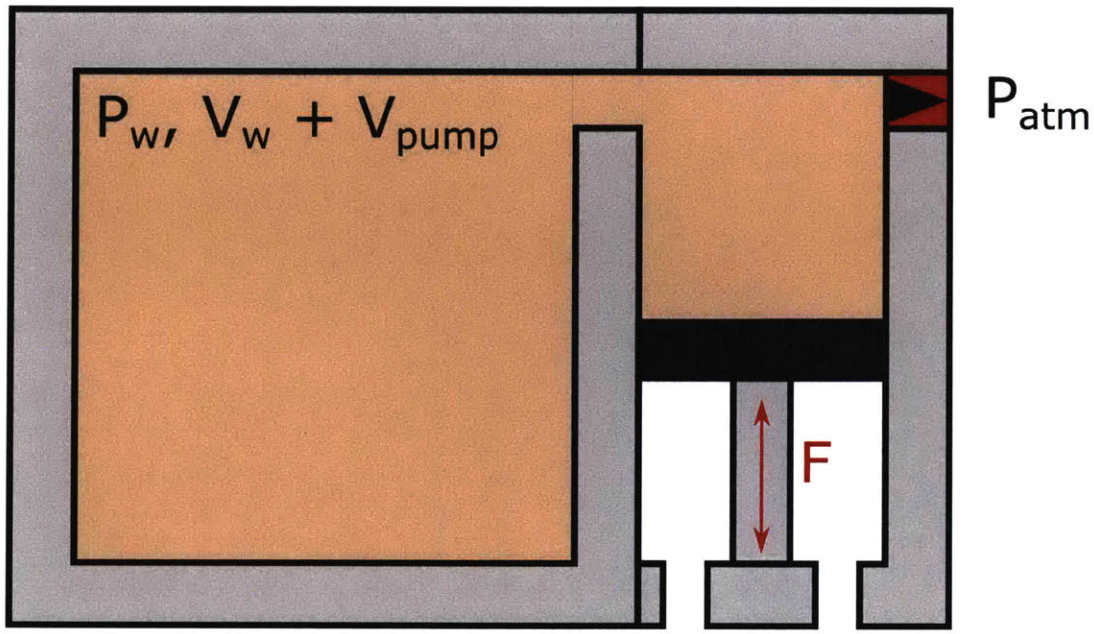

Figure 2-5: A wound of volume V_w is at a pressure P_w. When the pump extends, the pressure of the reciprocating pump, P_{pump} in the pump chamber and wound bed, $V_{pump} + V_w$ will become larger than atmospheric pressure P_{atm} and air will flow through the check valve 1 into the atmosphere.Next, when the pump retracts, the pressure both in the pump and the wound bed, P_w,will decrease

between the pump and wound bed, allowing for variable pressure applications without the need of a second pump. This simplifies the total energy over a single stroke for a perfectly sized pump to the following equation:

$$\begin{aligned} W_{stroke} = \; & [V_w + A_p(h_{max} - f_p h_0)]P_{atm} ln(\frac{P_{atm} + P_{crack1}}{P_{atm}}) \\ & + A_p(P_{atm} + P_{crack1})(h_{max} - \frac{1}{f_p}[h_{max} - \frac{P_{atm}}{P_{atm} + P_{crack1}}(h_{max} - f_p h_0)]) \\ & + [V_w + A_p h_{max}(1 - f_p)\frac{(P_{atm} + P_{crack1})}{P_{atm}})]P_{atm} ln(\frac{P_{wdes}}{P_{atm} + P_{crack1}}). \end{aligned} \tag{2.34}$$

Additionally, the maximum pump height can be calculated as well

$$h_{max} = \frac{(P_{wdes})(V_w - A_p(f_p h_0)) - (P_{atm} + P_{crack1})V_w}{A_p((P_{atm} + P_{crack1})(1 - f_p) - P_{wdes})}. \tag{2.35}$$

The total energy will be dependent on six variables: the cracking pressure of the two check valves, P_{crack1} and P_{crack2}, the final desired pressure and volume of the wound site,P_{wdes} and V_w, the initial dead volume of the pump $A_p h_0$, the space filling factor of the pump, f_p.

Secondly, the check valve can have its own internal leaking. This leak can be modeled by lumping into the leak rate of the entire system, raising the energy required of the system. The solution to this is straightforward in theory, but hard to implement in practice. It has been found that leakage is highly dependent on sealing pressure[49]. A higher sealing pressure will reduce leakage (but most likely at the cost of a higher cracking pressure).

Lastly the check valve, being made of an elastomeric material, will have its own time response to opening and closing. If the piston starts to retract before check valve 1 has fully closed, air will leak into the wound site. To solve this issue, the pumping frequency must be lowered, meaning that the stroke length of the pump must increase for the same power output. A conservative estimate of 10 minutes per pumping cycle is used to ensure no leakage due slow closure of the check valve.

As previously mentioned, a single stroke cycle pump will theoretically be less efficient than a multi stroke pump. However, an addition of a check valve will increase the necessary work per stroke, and if the cracking pressure of the check valve is sufficiently high, any efficiencies from multiple strokes are no longer realized if the single stroke pump can eliminate one of the check valves in the design (see figure 2-5).

2.5.3 Holding Force

While removing the check valve is helpful in reducing the energy needed over a pump cycle and allowing for variable negative pressure therapy without the need of a second pump, it introduces the problem of a necessary holding force for the actuator when it is maintaining a pressure. This force could be supplied by the actuator itself, or through friction. Unfortunately, both these options contribute highly to inefficiencies. A better solution would be to use an actuator that has a catch-state (such as types of mollusk muscle[50]) or expend very little energy in its holding state (such as a

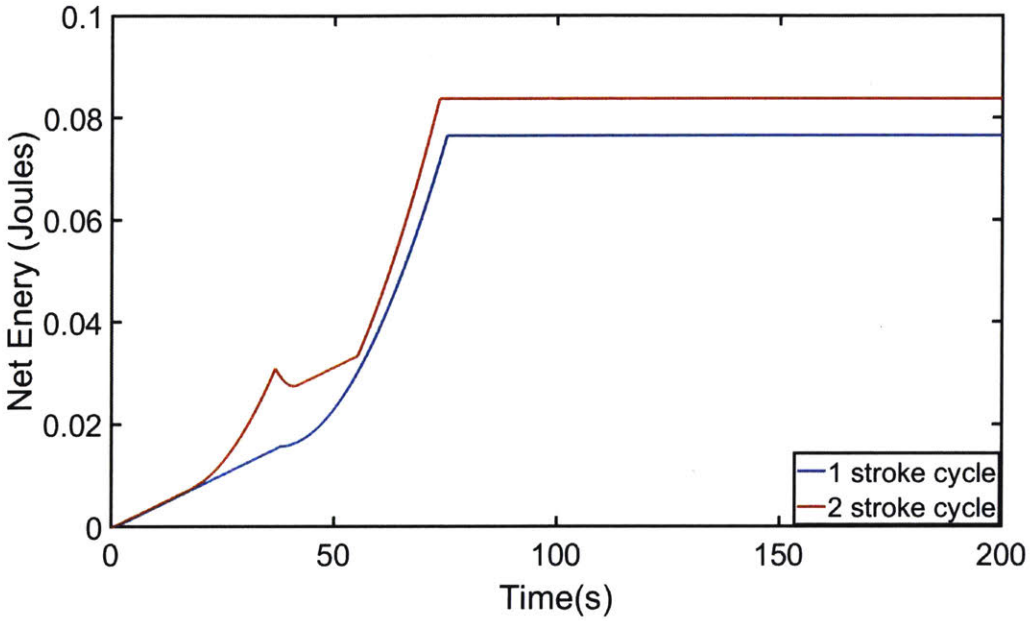

Figure 2-6: A simulation of how varying stoke length affects total energy required to reduce pressure wound pressure to 80 kPa. A perfectly sized actuator was simulated for a wound volume of 20 mL, with perfect space filling, and a point force being applied by the pumping actuator. Cracking pressure of all check valves were 3 kPa, but the 1-stroke pump did not require check valve 2

piezoelectric element).

2.5.4 Friction in Sliding Seals

As alluded to earlier, friction can quickly lead to energy usage much higher than the actuator itself. However friction is often encounter in sliding-seal elements such as that between a piston and cylinder in a syringe. While friction forces can be reduced by maintaining sealing pressure to a minimum, the use of sliding seals in general will cause a degradation of this seal over time, creating leaking, or needing an unnecessarily high sealing pressure [51]. Due to the low force requirements of the pump in NPWT, the friction of the sliding seals will end up being more than the energy of the pumping cycle itself. Friction-less actuation such as through a bellows mechanism avoids this problem, but adds its own, as studied next:

2.5.5 Wasted space in actuator extension

In general, any dead space in the actuator motion is a hindrance in two ways: it increases the length the actuator must travel to displace a certain volume, and adds to the effective wound volume whose pressure must be reduced. For a perfectly sized actuator, the stroke of the pump, V_{stroke}, needed becomes

$$A_p h_{max} = V_{stroke} = V_w \frac{P_{atm} - P_{wdes}}{P_{wdes} - (1 - f_p) P_{atm}}. \tag{2.36}$$

The change in energy will be approximately proportional to the space-filling factor, f_p. While a bellow with a low fill factor may lead to inefficiencies and an increase in the stroke length of the actuator, it will still compare favorably to a sliding-seal mechanism (see Figure 2-7)

2.5.6 Actuator Efficiencies

Another source of inefficiency is the efficiency of the actuator driving the pump. The electromechanical efficiency describes the amount of mechanical work that can be

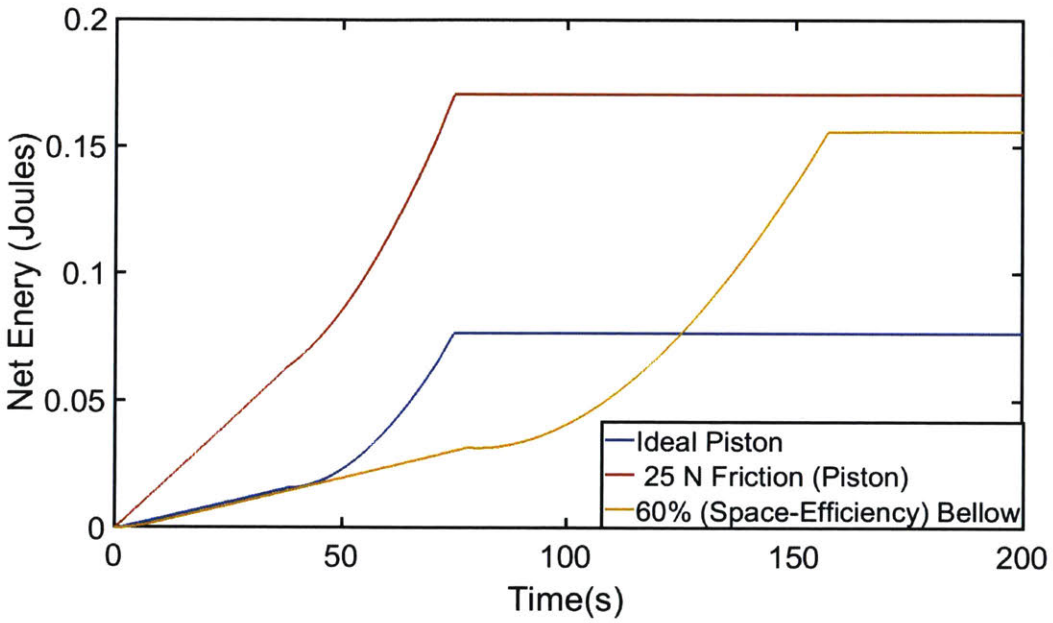

Figure 2-7: A simulation of how friction affects total energy required to reduce pressure wound pressure to 80 kPa. A perfectly sized single stroke actuator was simulated for a wound volume of 20 mL, with a point force being applied by the pumping actuator. Cracking pressure of all check valves were 0 kPa. The friction case had a friction of 25 N with perfect space filling, while the bellows case had no friction, but only 60% space filling efficiency

obtained per unit of electrical energy delivered to the actuator.

The electrical energy that is not transferred to mechanical work is transferred to two different elements. First, some energy will be lost through dissipative elements such as internal resistances or damping. Such an example would be a badly geared electric motor, in which a lot of power is dissipated through the resistive element of the motor coils. However, there will also be some initial electrical energy that will be transferred to an energy storage element, such as a spring or capacitor. Such an example would be the capacitive charge held by a piezo. During a round trip (extension and retraction of an actuator), this energy can be recovered, improving the efficiency of the device. One model for this energy flow can look as follows

$$n_{tot} = \frac{n_f n_{mech}}{1 - n_r(1 - n_{mech})}, \tag{2.37}$$

where n_f is the forward efficiency of the actuator where energy is converted to either mechanical work or stored energy, n_{mech} is the theoretical electromechanical efficiency of the actuator assuming no losses, and n_r is the reverse efficiency of the actuator where stored energy is being recovered. While high energy storage efficiencies (n_f, $n_r \geq 90\%$) will boost performance of our actuator when it is working as a pump, at modest energy storage efficiencies (n_f, n_r = 20%-60%), the round trip efficiency will still be in the same order of magnitude as our electromechanical efficiency.

2.5.7 Contact area of the Actuator

At first glance, it may seem that the net energy needed to generate a negative pressure is independent of the contact area between our actuator and piston. While this may be true in idealized systems with perfectly efficient energy transfer, this is not the case. It is helpful to see the energy needed to be provided by the actuator during the different regions of operation (see Figure 2-8).

As the contact area of the actuator takes up a larger area of the total area of the piston, more force must be applied (and energy exerted) to initially to push the piston forward. This same equation implies, however that there is less force required

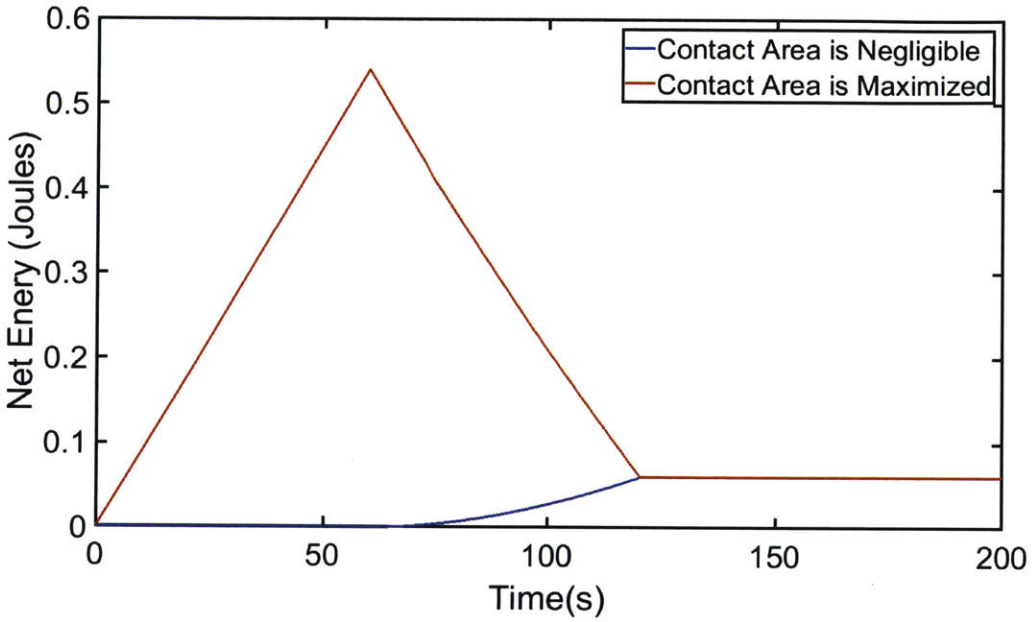

Figure 2-8: A simulation of how varying contact area of the actuator affects total energy required to reduce pressure wound pressure to 80 kPa. A perfectly sized single stroke actuator was simulated for a wound volume of 20 mL, with perfect space filling, and a point force being applied by the pumping actuator in the negligible contact area case, and the with the contact area of the actuator equal to the piston area in the maximum case. Cracking pressure of all check valves were 0 kPa. While the final energy of both instances were the same, the maximum contact area case required more energy in region 2, but recovered energy in region 4.

to pull the actuator backwards. In fact, for a particular area, energy can be recovered in this process, as work will be done by the air in the wound bed, on the actuator.

It is unrealistic to assume that all this work will be recovered by the actuator. In the worst case scenario, none of this work is recovered as energy. In this case, it is ideal that the contact area of the actuator be as small as possible. However, in practice manufacturing constraints make this difficult. A larger contact area will affect the efficiency of our pumping mechanism by increasing the energy requirements of our actuator in the forward stroke, with the risk of not fully recovering all the extra energy exerted.

2.5.8 Wound deformation

Current models have assumed that the wound volume will stay constant. Unfortunately, this is not the case. Though foam is present to prevent wound collapse, application of negative pressure will cause the wound volume to decrease. This decrease in volume can be estimated by dividing the negative pressure generated by the bulk modulus of human tissue. At a bulk modulus of 1 MPa, the 20 kPa pressure differential will result in a 2% deformation. For simplicity, wound deformation has been left out of our calculations.

2.6 Desired Actuator Characteristics

After a thorough investigation into the power, energy and space requirements, an actuator can be chosen. The key actuator characteristics and their desired values will now be described.

2.6.1 Size and Mass Considerations

The size of the NPWT device will primarily be determined by the size of the pumping system. For a bandage less than 15 mm in height, and less than 75 mm $\times$ 75mm, 50% of this volume can be conservatively allocated to the actuator, with the rest

for supporting electronics, energy storage, fluid handling mechanisms, and structural components. This limits the maximum volume the actuator can take up (in its fully extended state) to 42 mL. This limit on the maximum volume will inform the minimum strain, work density, and power density requirements of our actuator. The mass of our actuator is desired to be less than 10 grams. This was chosen as a value that would not be noticeable by the patient. This will inform actuator choice by setting a minimum limit on the mass density, specific power, and specific work of the actuator.

2.6.2 Mass and Density

If the actuator must weigh less than 10 grams, and at its fully extended form can take up 42 mL of space, the density of the actuator must be 238 kg/m^3.

2.6.3 Power Density and Specific Power.

The power the actuator can provide is critical, as it is a necessary requirement to maintain the desired negative pressure. Based on the calculations done earlier, in the worst case scenario 1 mW is needed to maintain a negative pressure of -20 kPa. Given the size and weight requirements, this corresponds to a power density of 0.023 kW/m^3. Similarly, the specific power must be greater than 0.1 W/kg.

2.6.4 Stress and Strain.

While the specific utilization of the actuator may affect the maximum stress that must be provided, in the simplest configuration, the actuator should be able to provide 20kPa, the maximum negative pressure differential that would be desired. The maximum strain will determine the pump stroke of the actuator. A larger pump stroke will help minimize check valve inefficiencies by allowing for a longer pumping period (and greater relaxation time for the check valves), or even eliminating the check valve between the wound bed and pump altogether. The calculation of maximum strain, ϵ_{max} can be found as a function by first relating the volume of stroke,

V_{stroke} needed to reduce pressure for an effective wound volume, which can be found in Equation 2.36.

Next, the strain can be found by comparing this desired stroke volume to the total available space of the actuator, V_{tot}

$$\epsilon_{max} = \frac{V_{stroke}}{V_{tot} - V_{stroke}}. \tag{2.38}$$

For a 20 mL wound volume, and 50% efficiency in space filing, the maximum strain of the actuator to allow for variable pressure therapy must be 50%. However, if we want to limit the pumping period to a 10 minute cycle at maximum leak rate, the effective volume of the wound increases. To allow for negative pressure to still be able to be applied,the maximum strain needed will be 280%.

2.6.5 Work density

The combination of the maximum stress and strain needed gives the work density requirements. Using the requirement that the 42 mL actuator must weigh less than 10 grams, this can also be converted to specific work. The minimum work density required for a 10 minute stroke cycle will be 56 kJ/m^3.

2.6.6 Electromechanical Efficiency

Based on the requirements of 1 charge every 24 hours, and a power requirement of 1 mW, and a 13 kJ battery, the minimum electromechanically efficiency must be 0.6% for continuous pressure holding, and 0.3% for repeated cycling of the pump. However, it is important to note inefficiencies from check valves, wound contraction, friction, and dead space in the pump will decrease the efficiency of the entire system.

2.6.7 Nominal Voltage

Similar to the bandage requirements, actuator voltage would ideally be under 4 volts, allowing for both safe operations in a potentially conductive environment, and easy

operation with Lithium batteries.

2.6.8 Bidirectionality and Controllability

An actuator that is controllable in both directions will allow for controlled variable pressure therapy, as well as cut down on space requirements for springs or other force-restorative elements.

2.6.9 Latch State

A latch state is critical in reducing energy consumption when the actuator is moving slowly or stopped, without having to rely on friction or some sort of active locking mechanism.

2.6.10 Scaling limits

The smallest dimension of the actuator (height) will be approximately 10 mm. It is important that manufacturing limits do not prevent efficient actuator operation at these sizes.

2.7 Comparison of actuators used currently

A compilation of the desired actuator characteristics along with a comparison of the current actuator types[50] used in these pumping applications is shown below:

Metric	Desired Quality	Electromagnetic Actuator	Piezoelectric Actuator	Constant Force Spring
Mechanical Efficiency	0.6%	80-90%	1-10%	-
Power Density	0.023 kW/m^3	100 kW/m^3	70 kW/m^3	-
Specific Power	0.1 W/kg	200 W/kg	10 W/kg	-
Work Density (10 min cycle)	56 kJ/m^3	20 kJ/m^3	35 kJ/m^3	56 kJ/m^3
Max Strain (10 min cycle)	280%	100%	0.1%	2000%
Nominal Voltage	< 4.2 V	< 12 V	> 100 V	Passive
Controllable in both directions	Yes	Yes	Yes	No
Catch State	Yes	No	Yes	No
Smallest dimension	< 10 mm	13.15 mm	3.8 mm	30 mm

Table 2.2: Comparison of various actuators for NPWT application. Electromagnetic and Piezoelectric specifications were from Hollerbach, et al[50].

All actuators currently being used are unable to satisfy all the requirements necessary. Neither eleecromagnetic of piezoelectric actuators can provide the strains necessary for efficient operation. Additionally electromagnetic actuator have no inherent latch state, and are difficult to scale to the dimensions desired. Piezolectric actuators have such a small strain, that their power output in pumping requirements is greatly hindered by inefficiencies in check valvues. Additionally, they require large voltages to operate. While constant force springs satisfy both energy and power requirements, they are inherently passive devices. With no satisfactory actuator choice, an electrolytic actuator was developed, which will be covered further in the next chapter.

Chapter 3

An electrolytic actuator

3.1 Inspiration

As covered in the last chapter, the challenge towards making a portable NPWT device is an actuator problem: high leak rates require higher power requirements for our pumping mechanism, and very large strains are necessary for variable pressure therapy. Additionally it was desired that the number of hard components be minimized. Using a gas as a working medium is desirable: a gas filled pouch is inherently soft, and is inherently light. Three different methods of increasing gas pressure were initially studied: increasing gas temperature, phase change of liquid to gas, and chemical reaction of liquid to gas.

3.1.1 Temperature change

Temperature change of a gas was found to be insufficient to create the pressure differences necessary. For example, even for a fixed volume, a temperature change of 60 °C is needed to create 20 kPa of pressure. Additionally, this mechanism would not have any possible latching feature, as energy would be needed to constantly keep the gas at a particular chamber.

3.1.2 Phase change

Phase change of liquid to gas appeared much more promising. The evaporation of water from liquid to gas creates approximately a 1300× change in volume at atmospheric pressure. In addition, the energy needed to convert water to gas is relatively low: the molar heat of vaporization of water, ΔH_{vap}, is 40.7 kJ/mol. The amount of PV work that can be done for an idea gas is

$$\Delta(PV) = \Delta(n)RT, \tag{3.1}$$

where R is the ideal gas constant (8.314 J/(mol K)), and T is the standard room temperature (298 K). This will correspond to 2.48 kJ/mol. The electromechanical efficiency will be:

$$n_{mech} = \frac{RT}{\Delta H_{vap}}, \tag{3.2}$$

which will result in an electromechanical efficiency of 6%. Unfortunately, the one large draw back is that such a method is not easily controllable in both directions, as cooling of the water vapor back to liquid is difficult to control in a metered way due to the influence of external heat sources and sinks in the environment. For the same reasons, a latch state is difficult to achieve, as any heat to and from the actuator will cause water vapor to turn back to liquid.

3.1.3 Chemical reactions

Gas production via chemical reaction is most promising. Gas production from liquid or solid reactants would once again produce a very high change in volume. In addition, if the chemical reaction was an electrochemical reduction-oxidation reaction, the rate of reaction could be controlled easily in both directions by the application of an electrical potential. Maintaining a particular voltage would allow for an easy latch state, as well as possible energy recovery.

3.2 Electrolytic Actuator

3.2.1 Basic Working principle

The electrochemical reaction chosen for actuation was electrolysis of water into hydrogen and oxygen. The hydrogen gas can be stored and used to push out the actuator. The oxygen gas can be stored separately, or vented to the atmosphere.

$2\,H_2O + 4\,e^- \longrightarrow 2\,H_2 + O_2 + 4\,e^-$, ΔG° = 237.1 kJ/mol

The reverse reaction will cause the hydrogen gas to be converted back into water. This is the reaction that occurs in a hydrogen fuel cell, and can be used to recover energy from our device.

$2\,H_2 + O_2 + 4\,e^- \longrightarrow 2\,H_2O + 4\,e^-$, ΔG° = -237.1 kJ/mol

The general structure of a fuel cell is shown below. Since this reaction is a reduction-oxidation reaction, there must be a transfer of electrons and protons in the reaction. Generally, protons will flow through an electrolyte solution, while electrons will flow through a conducting metal.The anode loses both the protons and electrons (oxidation), while the cathode gains both protons and electrons (reduction). In electrolytic mode the anode is the oxygen electrode, and the cathode is the hydrogen electrode, while in fuel cell operation the cathode is the oxygen electrode, and the anode is the hydrogen electrode. While the anode and cathode of the cell may flip depend on the direction of current flow, the oxygen electrode will always have a positive potential with respect to the hydrogen electrode. If a sufficient positive voltage is applied on the oxygen electrode with respect to the hydrogen electrode, electrical energy will be converted to chemical (and mechanical) energy, as water is split into hydrogen and oxygen (see Figure 3-1). Conversely, if no voltage is applied, the hydrogen and oxygen will recombine to water, turning chemical energy back into electrical energy in the process (see Figure 3-2).The rate of hydrogen gas formation/consumption can be related to the current flowing through the cell in either direction as follows:

$$\dot{n_{H_2}} = \frac{i}{2F}, \tag{3.3}$$

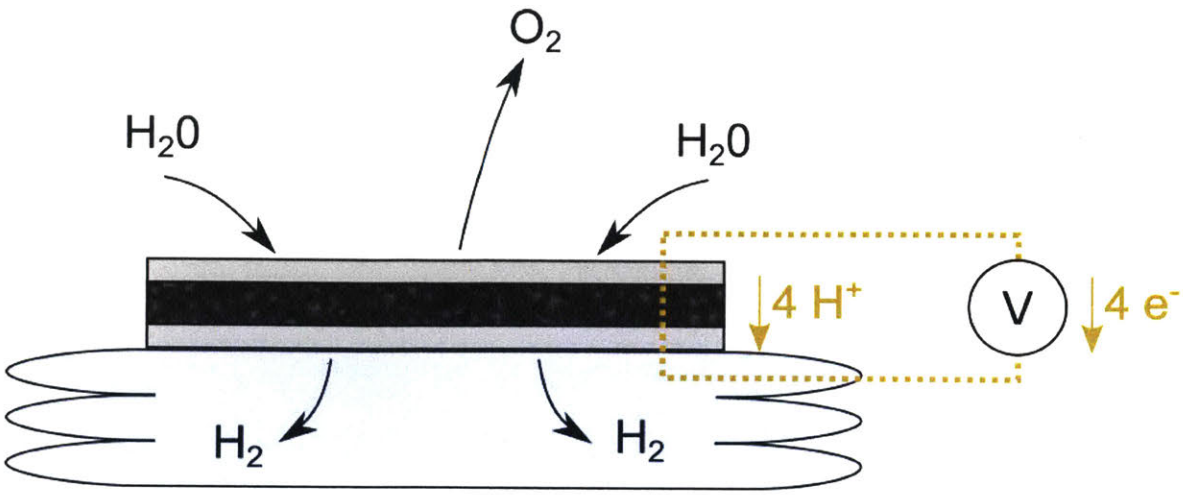

Figure 3-1: Illustration of electrolytic actuator in electrolytic operation. When expanding, 4 electrons are transferred to convert 2 molecules of H_2O to 2 molecules of H_2 and 1 molecule of O_2.

where i is the current through the cell, F is Faraday's constant (96485 C/mol).

The gas formation relationship was confirmed via video analysis of a custom made bubble flowmeter as seen in Figure 3-3. The measured flow rate was within 1% of the the expected flow rate.

3.2.2 History

Electrolytic actuators have been used in the past for very low power operations. Work has been done by CG Cameron[52] in explaining basic principles of an electrolytic actuator, and Sheybani et all have developed a bellows based metering pump on this principle [53]. However, none of the work before have shown true bidirectionality of the actuator. While electrolysis performance has been well documented, retraction of the actuator in a controllable manner via fuel cell operation has not been demonstrated.

3.2.3 Thermodynamics

The Gibbs free energy of the electrolysis reaction can be calculated from the standard enthalpies and heats of formation for hydrogen, oxygen and water, and is +237.1 kJ/mol, meaning that electrolysis of water into hydrogen and oxygen will require

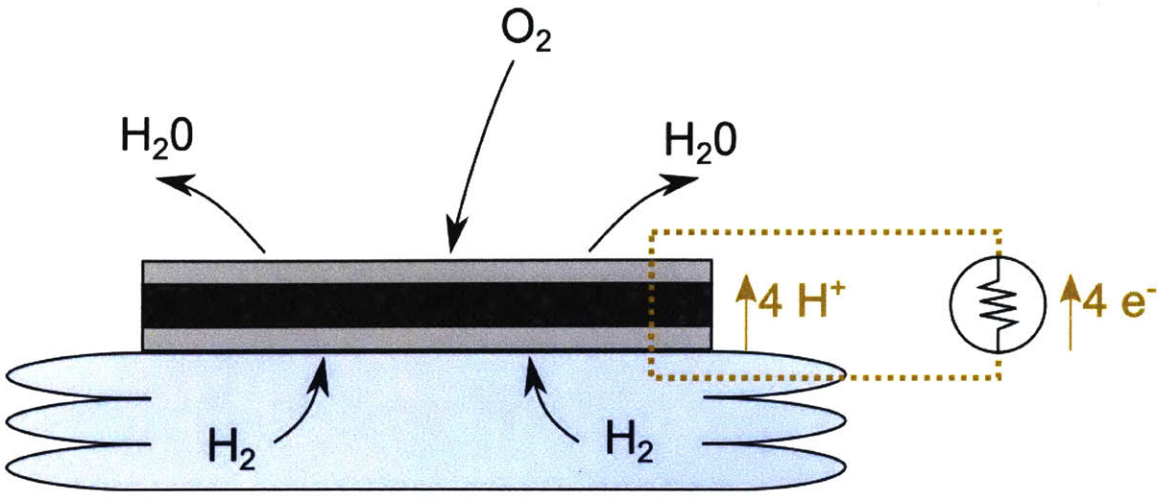

Figure 3-2: Illustration of electrolytic actuator in fuel cell operation. When retracting, 4 electrons are transferred the other way to convert 2 molecules of H_2 and 1 molecule of O_2 to 2 molecules of H_2O.

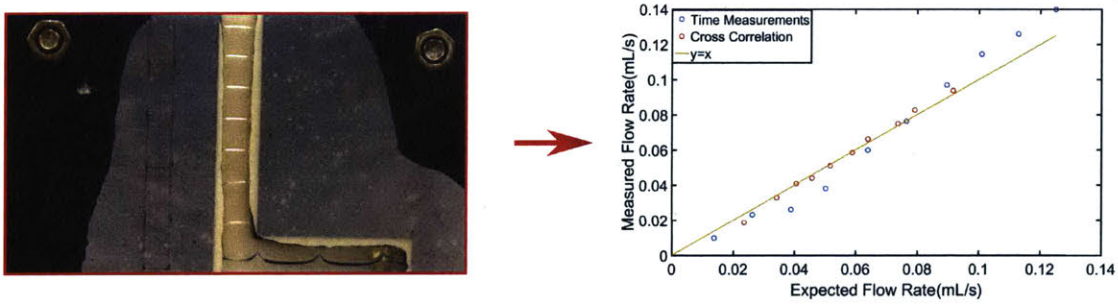

Figure 3-3: Video analysis of a custom bubble flowmeter was performed to ensure flow rate was as expected.

energy, while the reverse reaction will provide energy.The amount of mechanical work (PV work) that this reaction provides will be the same as before in equation 3.1. The efficiency will now be based on the Gibbs free energy of the reaction:

$$n_{mech} = \frac{RT}{\Delta G^{\circ}}. \tag{3.4}$$

This means when used in electrolysis mode, the upper limit of the electrochemical efficiency will 1%. However, if the energy during fuel cell operation is recovered, efficiencies can be much higher. The most general formula will be that of Equation 2.37, reproduced here:

$$n_{tot} = \frac{n_f n_{mech}}{1 - n_r(1 - n_{mech})}. \tag{3.5}$$

As energy storage efficiencies increase, mechanical efficiency over a cycle will approach 1. However, inefficiencies in both charging and discharging the fuel cell will affect this value.

3.3 Electrolytic Actuator Inefficiencies

3.3.1 Theoretical Cell Voltage

The theoretical cell voltage, or standard potential, available in fuel cell operation (or that must be supplied for electrolysis can be found from the Gibbs free energy of the reaction

$$E^\circ = \frac{\Delta G^\circ}{zF}, \tag{3.6}$$

where z = the number of electrons transferred in the reaction (which is 2), and F is Faraday's constant (96485 C/mol). This cell voltage of a hydrogen-oxygen fuel cell is 1.23 V. However, this approach obscures the specifics of the mechanism occurring. In reality, there are two reactions occurring, one at each electrode of the cell. On the positively charged side of the fuel cell, oxygen gas will be reduced to water:

$O2 + + 4\,H^+ + 4\,e^- \longrightarrow 2\,H2O$, $E^\circ = 1.23$ V, and on the negative side, hydrogen gas is reduced to hydrogen ions $H2 \longrightarrow 2\,H^+ + 2\,e^-$, $E^\circ = 0$V,

Adding the two cell potentials will once again result in a standard potential of 1.23 V. However,both charging and discharging efficiencies are due to deviations from the theoretical standard cell voltage. Deviations from this theoretical standard cell voltage will be due to either pressure loads, or high flow rates.

3.3.2 Effects of High Pressure

Pressure loads can affect forward efficiencies by affecting the cell voltage of the reaction (E_{cell}). This relationship is given by the Nernst equation, as shown below

$$E_{cell} = E^\circ - \frac{RT}{zF} ln(\frac{\alpha_{H2O}}{\frac{P_{H2}}{P^\circ}(\frac{P_{O2}}{P^\circ})^{0.5}}), \tag{3.7}$$

where α_{H2O} is the activity of water (1), P_{H_2} is the partial pressure of the hydrogen gas, P_{O_2} is the partial pressure of the hydrogen gas, and P° is the standard pressure, P_{atm}. Plugging in values will give:

$$E_{cell} = 1.23 + 0.0128 ln(\frac{P_{H_2}}{P_{atm}}(\frac{P_{O_2}}{P_{atm}})^{0.5}). \tag{3.8}$$

While there will be a rise in voltage necessary at higher pressures, this effect is very negligible. High pressure operation does not affect efficiency of actuator operation. Instead the upper bound on pressure limits is the gas crossover of the Nafion membrane, about 5 MPa.

3.3.3 High Flow: Overpotentials

The main source of inefficiency in charging and discharging is associated with high gas flow or currents through the fuel cell. This inefficiency is expressed in terms of overpotential, defined as the amount of additional voltage needed during electrolysis, and amount of voltage lost during fuel cell operation. There are three sources of overpotentials in an electrochemical cell (see Figure 3-4): activation overpotentials, ohmic overpotentials, and mass transport overpotentials. Taking into account all overpotentials, the voltage needed to charge the fuel cell (electrolysis) will be

$$V_{charge} = E_{cell} + \eta_{act} + \eta_{ohm} + \eta_{trans}, \tag{3.9}$$

where η_{act} is the activation overpotential,η_{ohm} is the ohmic overpotential, and η_{trans} is the mass transport overpotential. Similarly, the voltage the fuel cell will discharge at will be

$$V_{discharge} = E_{cell} - \eta_{act} - \eta_{ohm} - \eta_{trans}. \tag{3.10}$$

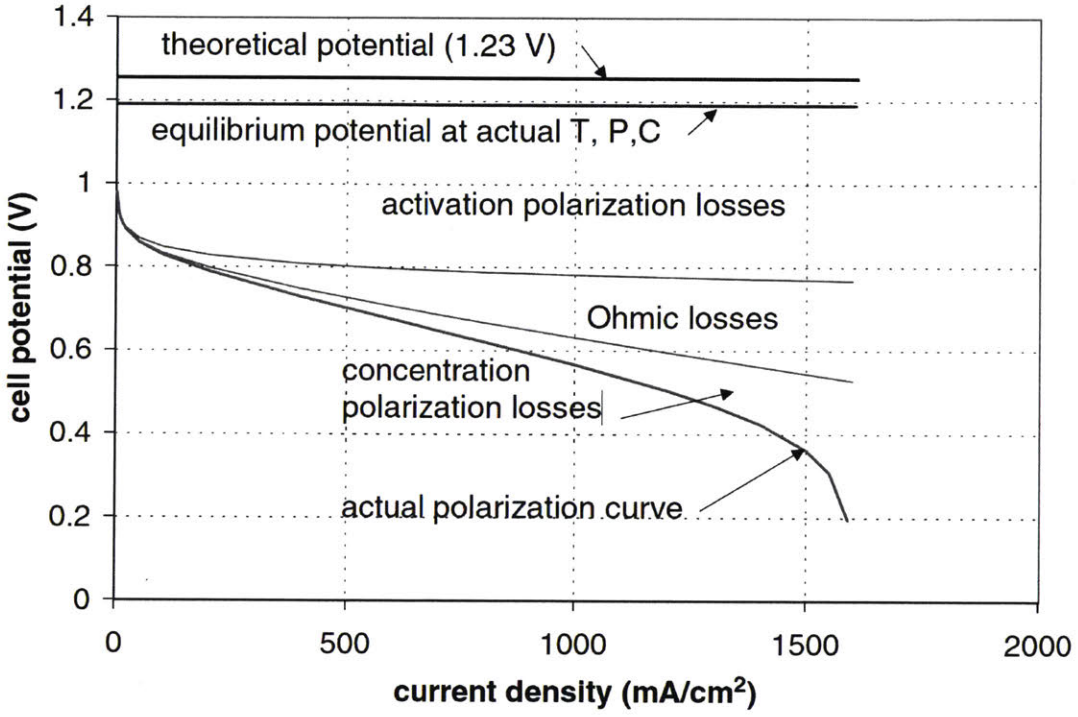

Figure 3-4: Sources of overpotential in a fuel cell. At low current, activation overpotentials dominate, with ohmic overpotentials dominating at mid level currents, and mass transport overpotentials dominating at the highest currents. Image taken from [54]

Activation Overpotentials

Activation overpotentials are the first to occur, and are due to the kinetics of the reaction. Every electrochemical reaction will have some free reaction rate, that can be measured as i_0. This value i_0 is determined by the catalyst type and catalyst surface area. To create currents greater than i_0, the potentials at each electrodes must be either raised or lowered to further encourage reaction in a particular direction. The amount the potential must be increased or decreased at a particular electrode is described generally by the concentration-overpotential equation:

$$i = i_0[\frac{C_{Osurf}(t)}{C_{Obulk}} e^{-\alpha \frac{F}{RT}\eta_{act}} - \frac{C_{Rsurf}(t)}{C_{Rbulk}} e^{(1-\alpha)\frac{F}{RT}\eta_{act}}], \tag{3.11}$$

where $C_{Osurf}(t)$ is the surface concentration at the electrode of the species being oxidized,$C_{Rsurf}(t)$ is the surface concentration at the electrode of the species being reduced, C_{Obulk} is the bulk concentration of the species being oxidized,C_{Rbulk} is the bulk concentration of the species being reduced, and α is the transfer coefficient, which will range from 0-1 depending on the the specific activation complex of the reaction (but it is often left as 0.5). If mass-transport effects are not an issue, the concentration of species at the electrode surface are the same as the concentration in the bulk, simplifying to

$$i = i_0[e^{-\alpha \frac{F}{RT}\eta_{act}} - e^{(1-\alpha)\frac{F}{RT}\eta_{act}}]. \tag{3.12}$$

This equation is known as the Butler-Volmer equation. As mentioned earlier, this equation must be solved for overpotentials at both the electrodes in a fuel cell. However, the reaction rate at the oxygen electrode is much slower than the reaction at the hydrogen electrode, making the overpotentials at the oxygen electrode much more pertinent.

Activation overpotentials are the largest source of inefficiency, and are mainly due to high activation energies of the oxygen reduction reaction. These overpotentials are mostly improved by choice of catalyst, and are outside the scope of the current work for improvements.

Ohmic Overpotentials

Ohmic overpotentials are due to contact resistance and ohmic resistance to the flow of protons through the selectively permeable membrane. Ohmic overpotentials are easily defined by Ohms law, and are described as

$$\eta_{ohm} = iR_{cell}, \tag{3.13}$$

where R_{cell} is the over all cel resistance. Ohmic overpotentials can be reduced by improving contact resistance, choosing a more conductive ion membrane, or simply operating at lower currents.

Mass Transport Overpotentials

At very high reaction rates, the reaction becomes limited by mass transport effects. Specifically, the reactive species will not be able to diffuse to the catalyst surface fast enough to support the consumption of the species. Instead, a concentration gradient will form, decreasing the concentrations of species at the electrode surface and resulting in an increase of the overpotentials seen in Equation 3.11.

Another mass transport related issue in the fuel cell is flooding of the oxygen side cathode. As water is produced, it will start to take up space and prevent access of the catalyst by oxygen gas, hindering fuel cell performance. One solution would be to use a hydrophobic coating on the catalyst so water will be transported quickly from the catalyst surface. However, this does not work well in the current design, as the same device is used for electrolysis and fuel cell operation: During electrolysis, a hydrophobic coating will hinder access to water and production of hydrogen gas. This overpotential is more apparent when actuator is used in fuel cell operation for a long time at high currents.

3.3.4 Measured i-V curve

A standard current-voltage curve of the fuel cells used is shown below in Figure3-5. The curve was measured using a VMP2 Potentiostat with a sweep rate of 10 mV/s.

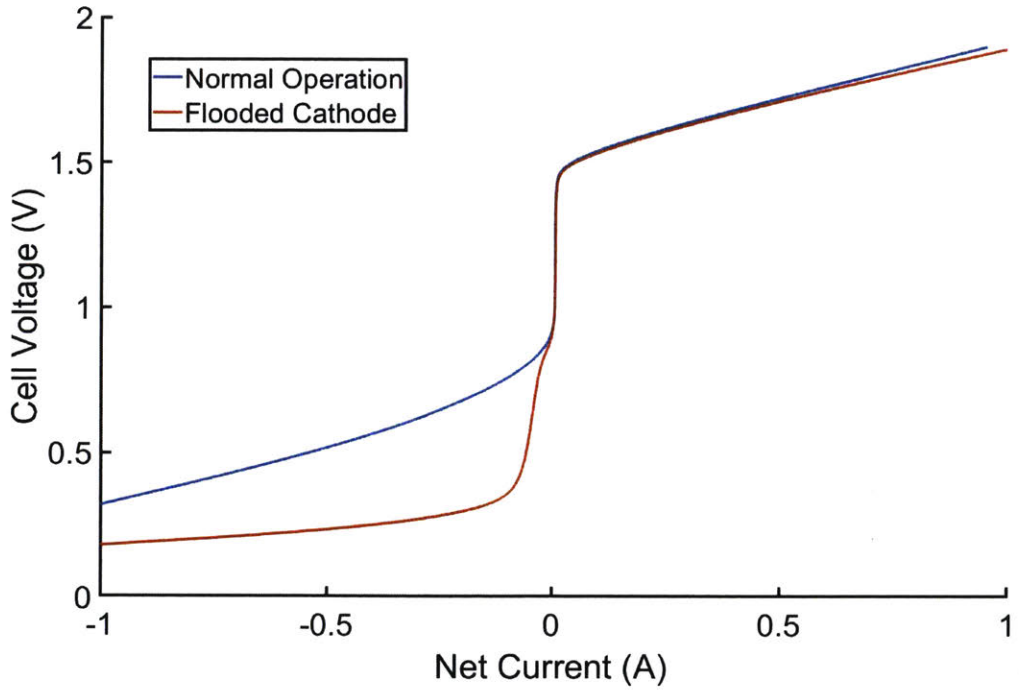

Figure 3-5: Measured i-V curve of fuel cell[55]. Both normal operation (blue) and operation when the oxygen side cathode is flooded (orange) are shown. Negative currents correspond to fuel cell operation, while positive currents correspond to electrolytic operations

While high current operation are allowable for a short period of time, eventual flooding of the cathode will reduce performance.

It can be seen that even when the oxygen electrode is not flooded, both charging and discharging efficiency are affected mainly by overpotentials. The overall efficiency of the actuator will be

$$n_{tot} = \frac{\frac{E^\circ}{V_{charge}} \frac{RT}{\Delta G^\circ}}{1 - \frac{V_{discharge}}{E^\circ}(1 - \frac{RT}{\Delta G^\circ})}, \tag{3.14}$$

where V_{charge} and $V_{discharge}$ are the charging and discharging voltages of the cell, respectively.The electrolytic actuator will be more efficient at lower current and low flow rates. However high leak rates may require higher currents, affecting efficiency. At a current of 0.7 A, a flow rate of 87.5 $\times$ 10 $^{-3}$ mL/s mL/min is created, which is large enough to reduce pressure even at the maximum designed leak rate 3 mL/min.

3.4 Fuel Cell Structure

While many different fuel cell types exist, a proton-exchange membrane (PEM) based fuel cell was used to minimize profile. To learn how to minimize the profile of such an actuator, it is important to know the function of the various components of a PEM fuel cell.

3.4.1 PEM Membrane

The most distinct portion of the PEM fuel cell is the proton exchange membrane itself. The purpose of this membrane is to selectively allow only hydrogen protons to cross the membrane. The PEM must have high specificity (allows only hydrogen ions through) as well as high mobility (allows hydrogen ions to pass through quickly). The most common proton exchange membrane is Nafion, due to its high specificity, high mobility, and thermal and mechanical stability. Despite the high specificity, there will still be some crossover of hydrogen gas to the oxygen electrode. This crossover rate will be dependent on both the thickness of the Nafion membrane, and the pressure differential across the membrane.

3.4.2 Catalyst

The catalyst is the most important component in determining the efficiency of the fuel cell. While conversion of hydrogen and oxygen into water is thermodynamically favorable, the process will still happen slowly due to the activation energy of the reaction. A catalyst is used to lower the activation energy by allowing a site for the reaction complexes to bind to during the reaction. A common catalyst is a noble metal such as platinum. The ideal catalyst should allow for easy binding of various reaction complexes, but also for easy release of the finished product.

In fuel cell operation, the oxygen reduction reaction is the rate-limiting step of the process. While an idcal catalyst for oxygen reduction is still an active area of research, iridium rubidium oxide and platinum is a commonly used catalyst for oxygen reduction, while platinum is used on the hydrogen electrode. To improve available

surface area, rather than a sheet, a fine powder of catalyst (such as Platinum Black) is used. For the device a pre-assembled Nafion 115 membrane coated with these catalysts (Horizon Fuel Cell)[55] was used.

3.4.3 Gas Diffusion Layer

The gas diffusion layer is often times a thin, conductive, and porous sheet that allow for hydrogen and oxygen diffusion to the catalyst while still allowing of transfer for electrons from the electrode. These requirements result in the gas diffusion layer being a porous carbon based structure such as carbon cloth, or graphite felt. However, gas diffusion layers do not work well in assemblies that are meant to be run both as a fuel cell and electrolyzer (known as a unitized, regenerative fuel cell), as electrolysis causes oxidation of the carbon as well, reducing electrical contact and performance of the device. A gas diffusion layer was not used in the PEM fuel cell used, instead opting for a wire mesh current collector.

3.4.4 Current Collector/Electrode

The current collector, or electrode provides the electrical contact to the PEM fuel cell assembly. The current collector must have high conductivity, and be able to withstand compressive forces which will be use in assembling the device. The fuel cell assembly used utilized a platinum coated wire mesh, which allows for high conductivity, structural integrity, as well as a porous structure for gas diffusion.

3.5 Incorporation of an Electrochemical actuator into NPWT model.

The model from the previous section can be further refined to include the electrochemical actuator and bellow system. Because the force of the actuator is supplied by the pressure of the gas inside the chamber,P_c, the force balance can be adjusted as follows:

$$P_c(h)A_c = P_w(h)A_p - P_{atm}(A_p - A_c), \tag{3.15}$$

where we also can solve for P_c as a function of both h and the number of gas molecules added, n to the chamber:

$$P_c(h) = \frac{1}{h}(P_{atm}h_0 + \frac{nRT}{A_c f_c}), \tag{3.16}$$

where h_o is the initial dead space height of the actuator, and f_c is the space-filling factor of the actuator (different from the pump). For each region before, the $P_w(h)$ can be found to determine the While the general energy will not change, there are some key limitations for the electrolytic actuator. First, the actuator can only push, not pull, meaning that the force on the actuator may never be negative, meaning that there is a limit on how small the contact area A_c may be. Specifically,

$$A_c \geq A_p \frac{P_{atm} - P_{wdes}}{P_{atm}}. \tag{3.17}$$

To reach a final pressure of 80 kPa, A_c must be approximately greater than one-fourth of A_p, meaning the diameter of the actuator must be at least half the diameter of the larger piston. Additionally, it is no longer possible to have a perfectly sized pump. ($h_f = h_0$) This is because the initial dead space in the actuator will prevent complete retraction of the actuator. The minimum retraction height will be determined by the wound pressure and initial dead space, and will occur when all molecules of hydrogen gas have been consumed by the actuator.

$$h_f \geq \frac{P_{atm}A_c}{P_{wdes}A_p - P_{atm}(A_p - Ac)}h_0. \tag{3.18}$$

Now, to make sure the pump has retracted enough ,the maximum pump height, h_{max} will be:

$$h_{max} = \frac{P_{wdes}(V_w - A_p(f_p \frac{P_{atm}A_c}{P_{wdes}A_p - P_{atm}(A_p - Ac)}h_0)) - P_{atm}V_w}{A_p(P_{atm}(1 - f_p) - P_{wdes})}, \tag{3.19}$$

and the total energy will now be

$$\begin{aligned} W_{stroke} = & -P_{atm}(A_p - A_c))h_0(\frac{P_{wdes}A_p - P_{atm}A_p}{P_{wdes}A_p - P_{atm}(A_p - Ac)}) \\ & + [V_w + A_p(h_{max} - f_p h_0)](h_{max} - f_p h_0)P_{atm}ln(\frac{P_{atm} + P_{crack1}}{P_{atm}}) \\ & + A_p(P_{atm} + P_{crack1})(h_2 - \frac{1}{f_p}[h_{max} - \frac{P_{atm}}{P_{atm} + P_{crack1}}(h_{max} - f_p h_0)]) \\ & + [V_w + A_p h_{max}(1 - f_p)\frac{(P_{atm} + P_{crack1})}{P_{atm}})]P_{atm}ln(\frac{P_{wdes}}{P_{atm} + P_{crack1}}). \end{aligned} \tag{3.20}$$

The contact area between the actuator and the wound interface will now play a role in determining how much net energy is needed by the actuator. For simplicity in initial work, the pumping bellow of the pump was made the same as the actuation bellow of the actuator ($A_p = A_c$). This will simplify the equation to:

$$\begin{aligned} W_{stroke} = & [V_w + A_p(h_{max} - f_p h_0)](h_{max} - f_p h_0)P_{atm}ln(\frac{P_{atm} + P_{crack1}}{P_{atm}}) \\ & + A_p(P_{atm} + P_{crack1})(h_2 - \frac{1}{f_p}[h_{max} - \frac{P_{atm}}{P_{atm} + P_{crack1}}(h_{max} - f_p h_0)]) \\ & + [V_w + A_p h_{max}(1 - f_p)\frac{(P_{atm} + P_{crack1})}{P_{atm}})]P_{atm}ln(\frac{P_{wdes}}{P_{atm} + P_{crack1}}), \end{aligned} \tag{3.21}$$

where

$$h_{max} = \frac{P_{wdes}(V_w - A_p(f_p\frac{P_{atm}}{P_{wdes}}h_0)) - P_{atm}V_w}{A_p(P_{atm}(1 - f_p) - P_{wdes})}. \tag{3.22}$$

This total work is reflected in the energy recovered when consuming the moles of hydrogen again. However, this small amount of work is dwarfed by the energy loss due to the inefficiencies in energy recovery.

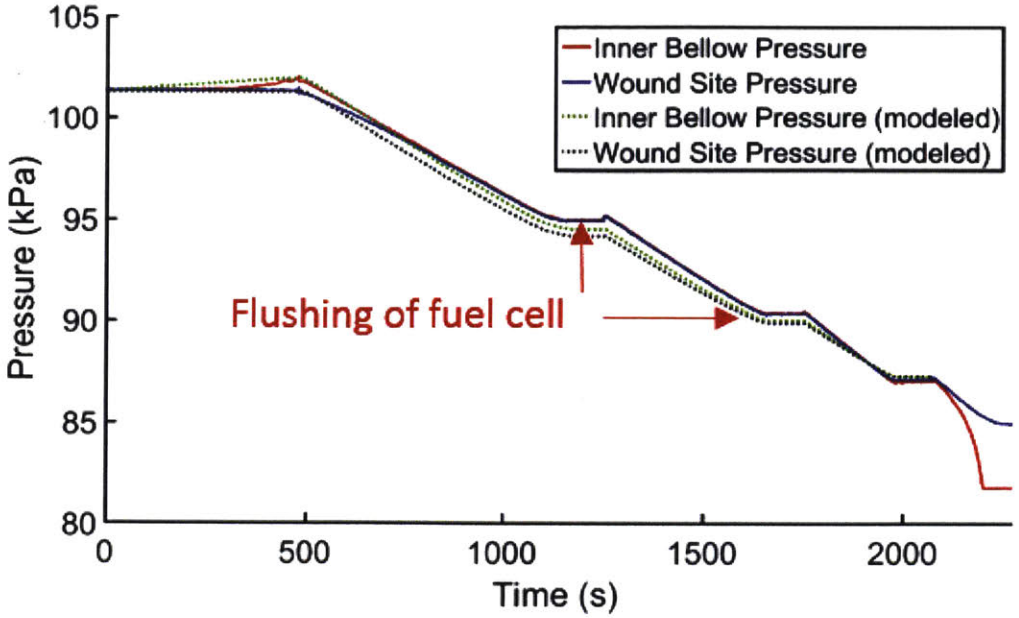

Figure 3-6: Initial setup for testing of an electrochemical actuator. A 50 mL bellow was expanded via electrolysis into a 250 mL chamber and sealed. The bellow was then retracted via fuel cell operation to generate a negative pressure.

3.6 Benchtop Feasibility Tests

To test the feasiblility of such a design, multiple configurations of a bellow in chamber were tested. A unitized regenerative fuel cell (Horizon[55]) was used during the tests. Wound chambers were simulated by a sealed container, and various molded and sheet-style bellows were tested. A 250 mL container was used to hold a a 50 mL capacity, bonded-sheet nominally closed bellow (see Figure 3-6). The bellow was brought to filled with hydrogen via electrolysis, and after fully filled, the 250 mL container was connected to a pressure sensor and closed to the atmosphere. The unitized fuel cell was then switched to fuel cell operation, bleeding the current through a set resistor. This concept was tested to test the possibility of operation on large wound volumes, and ignore any effects of hydrogen leakage in the containers.

As can be seen in Figure 3-7, the chamber was capable of reaching negative pressure. However large volumes wounds would need to be halted due to flooding of the oxygen cathode during fuel cell operation.

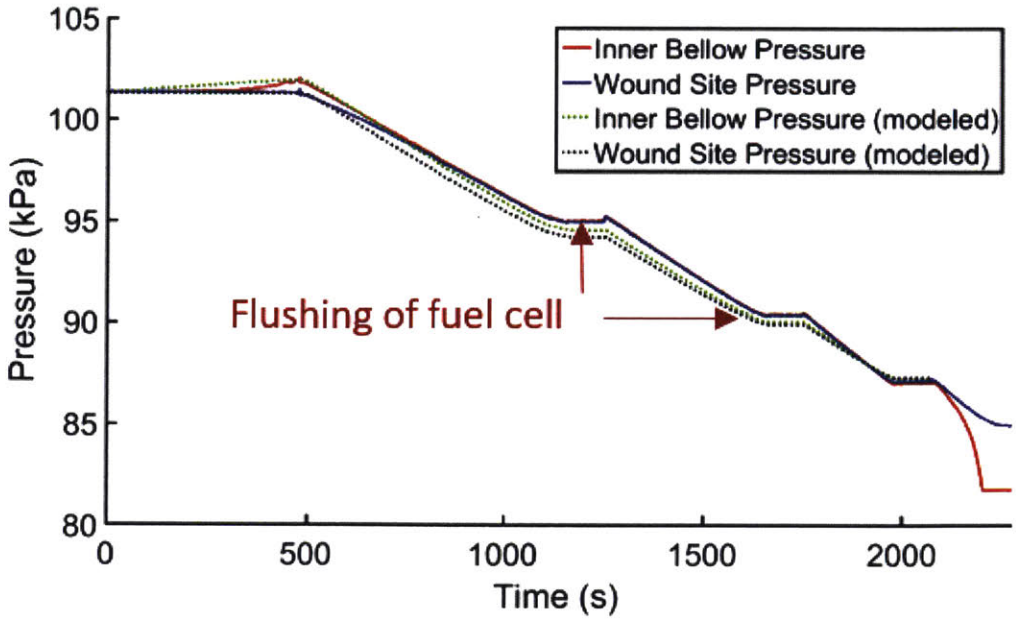

Figure 3-7: Results from initial testing of an electrochemical actuator. A 50 mL bellow was expanded via electrolysis into a 250 mL chamber and sealed. The bellow was then retracted via fuel cell operation to generate a negative pressure.

3.7 Custom Bellow Construction

In addition to reducing the profile of the fuel cell assembly, a bellow structure must be created to allow for storage of the hydrogen gas.

3.7.1 Bellows versus Piston and Cylinder

A bellow was chosen over a piston-cylinder assembly for multiple reasons. While a bellow will have more inefficiencies due to inefficient space-filling as it expands, a piston-cylinder assembly will have very high inefficiencies due to the friction of its sliding sea, particularly when comparing this friction force to the force necessary to overcome the 20 kPa pressure differential. Additionally, the maximum possible strain of a standard piston cylinder assembly is 100%, while the folding mechanism of a bellows allows for much higher strains.

3.7.2 Bellows Dead Space

Dead space, or the initial internal volume of the bellow contributes to inefficiencies in quite a few ways. First, the dead space is the lower limit for how compact the actuator can get. Minimizing dead space is key to achieve high strain rates while still maintaining a low profile.

Additionally, dead space contributes to loss of available hydrogen recovery. If the dead space is assumed to be dry air, a certain percentage of the air will contain oxygen gas, which will react with the produced hydrogen to produce water. If this water is in liquid form, this will affect the amount of PV work that can be done in expansion. Additionally, this produced hydrogen is lost, and will not be recoverable in retraction of the actuator.

Lastly, the dead space in the actuator will affect the amount of vacuum that can be generated. As shown in Equation 3.19, the amount the actuator will be able to retract is determined by the amount of dead space in the actuator. For a fixed size of pump, the initial dead space will limit the amount of retraction possible, and pressure that can be generated.

3.7.3 Bellows Stiffness

This stiffness of the bellow acts as an effective spring element that stores mechanical energy when expanding, and the releases energy when retracting. However, due to the energy recovery inefficiency of the electrolytic actuator, the energy from the expanded bellow is not all recovered as electrical energy. Additionally the low electromechanical efficiency of the actuator will mean that a lot of excess energy that is used to extend the bellow will not be recovered. For this reason, it is desired that bellow stiffness be as little as possible.

3.7.4 Pressure Ratings

The maximum pressure before bursting will affect bellow design and limit the maximum pressure attainable by the actuator. The main failure modes here will be due

to imperfections in the bellow, and along attachments of the bellow. The minimum vacuum rating of the bellow will be 80 kPa, and the minimum pressure rating must be higher than the cracking pressure of the check valves.

3.7.5 Hydrogen leakage

The primary purpose of the bellow is storage of hydrogen. Any leakage of hydrogen through the bellow will also leak through the wound volume. This results in inefficiencies in bellow expansion, and limits the amount of energy that can be recovered in bellow contraction. To reduce hydrogen leakage, metallized mylar sheets were used in final bellow construction. However, it is important to note that once fully expanded, the hydrogen leakage from the bellow will cause a decrease in wound pressure, and potentially counteract low leak rates into the wound site.

3.7.6 Modeling

A first order of bellow expansion was done to find the amount of space that could be filled by the bellows. Bellows were modeled as a 2D radially symmetric, thin membrane. The lower limit of the bellow shape was given by straight, triangular convolutions, while the upper limit was given by elliptical convolutions. A constant perimeter assumption was used: the shape of the bellow was adjusted so that the total perimeter of the bellow did not change. While this model does not capture bellow stiffness, it is useful in first order design when calculating the space-filling capabilities of different bellow geometries (see Figure 3-8).

3.7.7 Molded bellows

Silicone bellows were molded from Smooth-On Ecoflex 30 [56] (see Figure 3-9) . While these bellows had very high expansions, they could not be made thin enough to reduce dead space in the bandage. Minimum thickness of the bellows without tearing was 1 mm, creating too much dead space in the limited profile needed for the bandage.

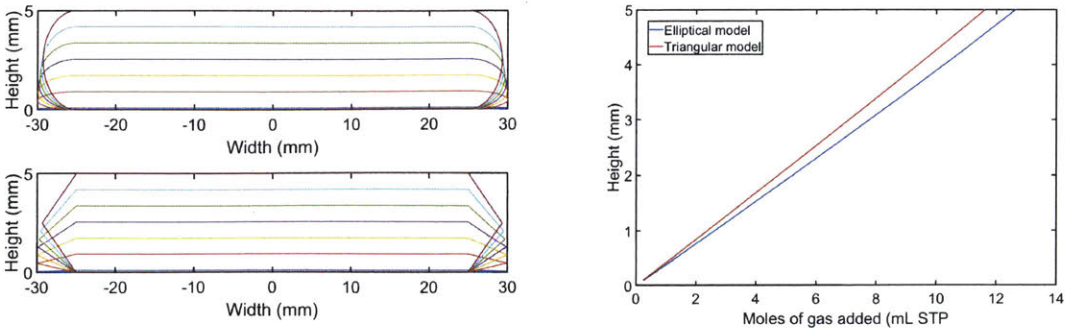

Figure 3-8: Modelling of Bellow Design. A constant perimeter assumption was used to model the space-filling factor of various bellows. Left: Both the best case (elliptical, top) and worst case (triangular, bottom) models of the bellow expansion were considered, and the height-to-gas added relationship was calculated.

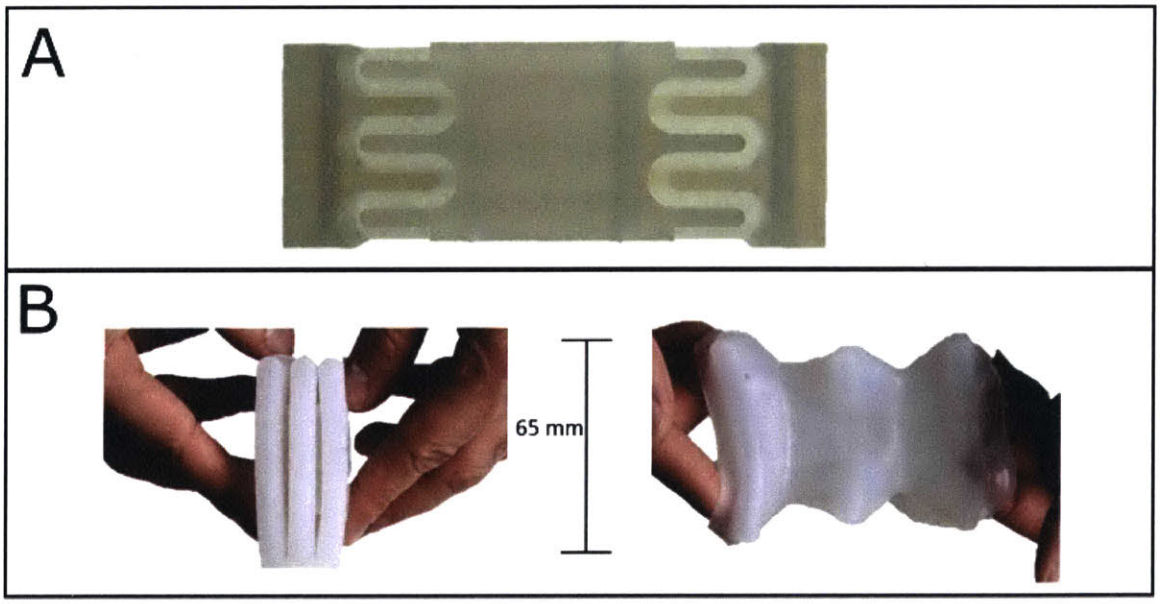

Figure 3-9: 3D printed mold (A) to make silicone bellows, and resulting bellow strain (B)

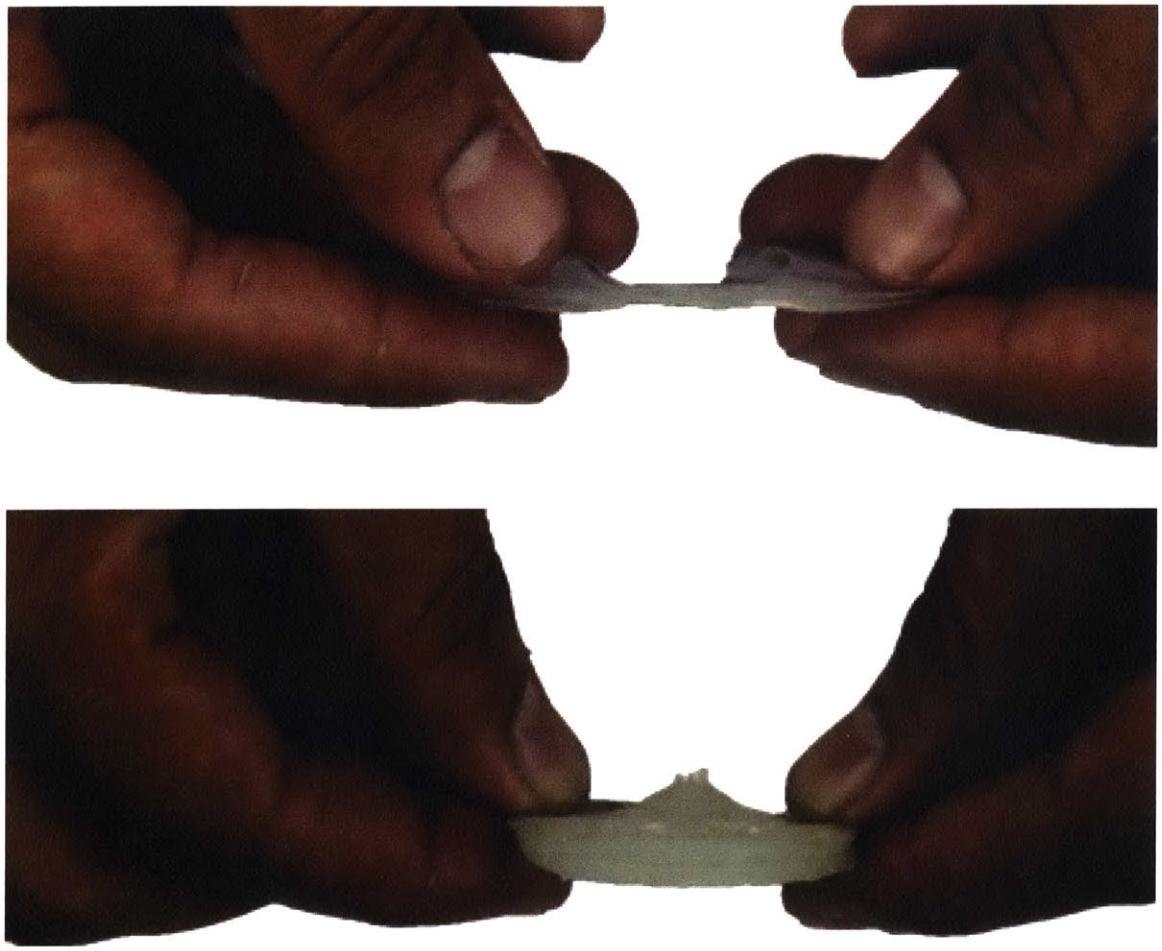

Figure 3-10: Thickness of molded (bottom) and bonded-sheet bellows. Molded bellows had a minimum thickness of 5 mm, while the bonded-sheet bellows had a sub-millimeter thickness

3.7.8 Bonded-sheet bellows

Alternatively, flat sheet bellows were made by bonding plastic sheets. While these bellows are slightly stiffer, and need more convolutions for the same strain, they have the advantage of being much slimmer, and with minimal dead space.

Bellow sheets were made with both polyethylene and metallized mylar sheets. Sheets were bonded together via thermal welding. While there are multiple high resolution methods to do this in industry such as ultrasound heating or laser welding, prototypes were made via heat sealing.

Heat sealing uses the effect of heat as well as pressure to create a satisfactory seal. Two methods of heat sealing were explored. Semicircle shaped Nichrome wire was

Figure 3-11: Fixtures used to thermally bond the polyethylene sheets. Two polyethylene sheets were clamped against the fixture and current was run through the nichrome wires briefly.

used to create low width thermal seals (see Figure 3-11). Sheets were clamped against the Nichrome wire, current was applied (6.3 A for 30 seconds), and then the sheets were unclamped after cooling. While this technique worked well for polyethylene, it did not work well for metallized mylar bellows, as much higher temperatures of the Nichrome were needed for sufficient heat transfer to the sealing layer of the metallized mylar. Additionally, the clamping of the metallized mylar to the raised profile of the shaped Nichrome created small cracks that would fail easily when under pressure. Metallized bellows were made using a flat iron to provide an even distributed heat and clamping force to the entire sheet. A mask made of polyimide tape was kept between metallized mylar layers to maintain the desired shape of the bellow.

3.7.9 Multiple convolution bellows

Metallized mylar sheets are only generally heat-sealable on one side, making multi layer bellows more challenging to make. Multi layer bellows were made of the metallized mylar membranes by carefully layering heat sealable mylar sheets. Alternatively, multiple convolutions of the bellow were attached to each other using 3M double sided tape (1509). Regardless of how the convolutions were created, the final attachment

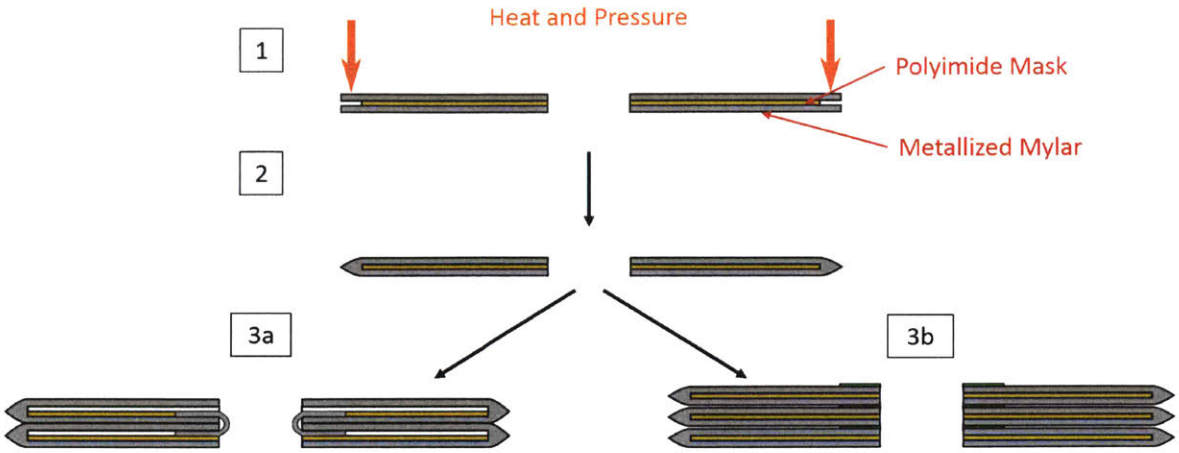

Figure 3-12: Mechanism to assemble multiple convolution of metallized bellows. A thin polyimide mask is used to ensure that only the outer edges of the bellow are sealed when heat and pressure are applied to create a single convolution of the bellow. (Steps 1 and 2) Each single convolution is then attached through more metallized mylar (3a) or via double sided adhesive (3b)

of the bellow to the actuator was done via double sided tape. With a 180° pull force of 600 N/m, a 40 mm diameter ring of tape could withstand 75 N of force, which would correspond to a wound pressure of 75 kPa in the current bellow designs (60 mm outer diameter of bellow). While this is close to the desired wound pressure of 80 kPa, the testing of the tape has been done as a 180° pull of the tape, while the loading conditions of the adhesive in the system will be a much smaller angle, improving adhesion properties further.

3.8 A thin profile actuator

For ease of manufacture, an off-the shelf unitized regenerative fuel cell was used for prototyping (Horizon). The PEM assembly was removed from the mechanical clamping, and a smaller profile actuator was constructed.

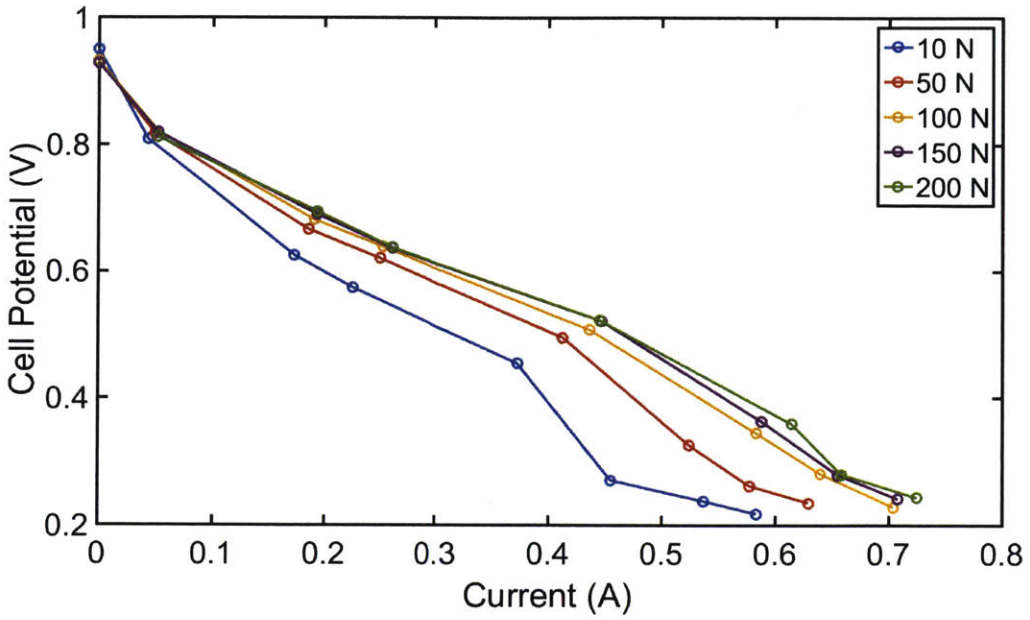

Figure 3-13: Clamping Force on the fuel cell versus fuel cell performance. Forces from 50 N to 200 N were tested.

3.8.1 Clamping Force

The largest challenge in construction a low profile actuator was providing the clamping force necessary for efficiency operation. The clamping force provides two functions: reducing the contact resistance between the components in the PEM fuel cell and compressing the rubber seals in the assembly to prevent gas leakage or crossover. A test was done on a bare PEM assembly to determine the optimal clamping force to reduce contact resistance. As seen in Figure 3-13 It was found that 100 N was sufficient in reducing the contact resistance of the cell. While additional force would be necessary to compress any gasket material such that a seal is maintained, this could be obviated through the use of a gap-filling epoxy or filler.

3.8.2 Thin Profile Assembly

To reduce the profile as much as possible, one of the sides of the PEM assembly was in contact directly with a custom built PCB, while the other was in contact with a stamped copper clip. The PEM assembly was placed on the PCB, lined with epoxy,

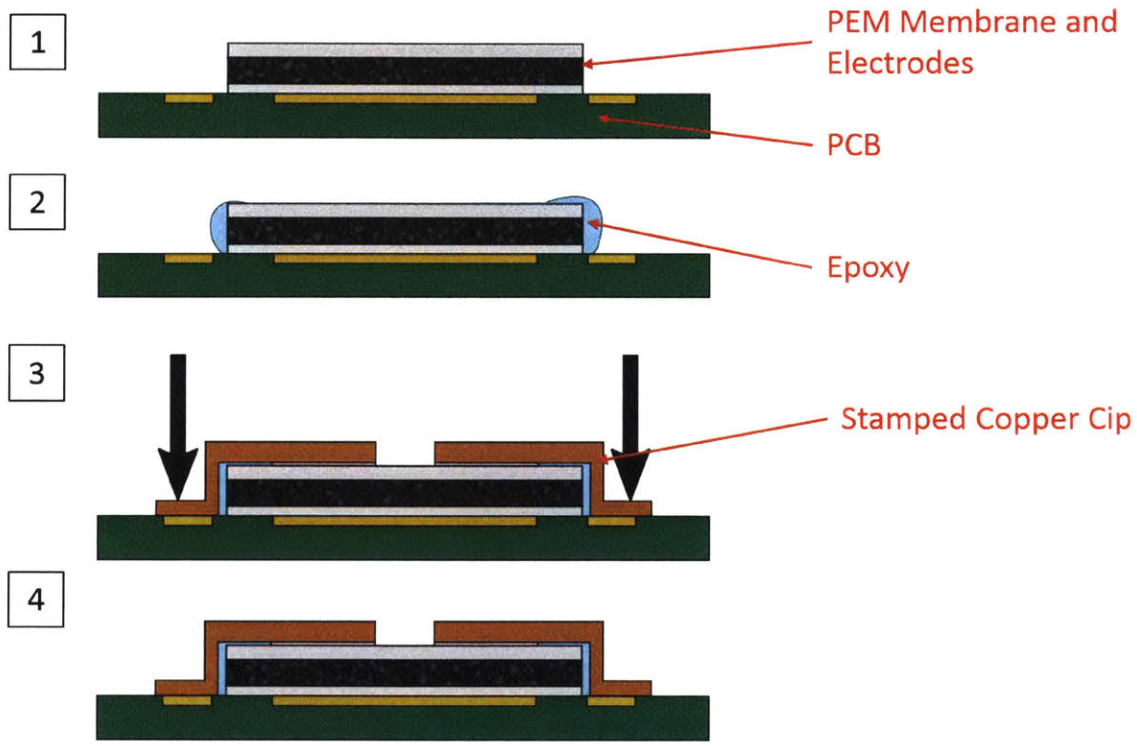

Figure 3-14: Assembly process of thin actuator. A PEM membrane and electrode assembly is positioned onto a custom PCB (1) and then lined with gap-filling epoxy (2). A custom stamped copper clip is then pressed against the assembly (3). After curing of the epoxy, the copper clip is removed (4). Fusion of the epoxy between the PCB and copper clip maintains the necessary compressive force on the membrane to reduce contact resistances, and the gap-filling epoxy eliminates gas leakage.

and then clamped via screws with the copper clip to apply a preload force. After the epoxy had set, the clamping screws were removed, but the compression on the membrane was maintained by the hardening an fusion of the epoxy to the PCB and copper clip. The epoxy setting process was done over a saturated salt solution at 70% RH to prevent drying of the membrane. The fuel cell was tested in free air to ensure that performance did not degrade. While the fuel cell performance was lower than future fuel cell assemblies used, it did not degrade due to the assembly process (see Figure 3-16). After the assembly process, the fuel cell assembly was left in free air to simulate drying in the environment. After 3 days of drying, fuel cell performance started to decrease. The profile of the entire assembly was 3 mm. Initial assembly had the copper clip soldered directly to the PCB, while in later attempts the clip was attached to epoxy to avoid possible breakdown of the Nafion membrane at high temperatures.

3.8.3 Actuator Comparisons

Now that a thin actuator has been assembled, it can be compared to the actuators from the previous section. The maximum strain and stress are gotten from the volume change of water to hydrogen gas (1300×), and the maximum pressure of the Nafion membrane (5 MPa), allowing for calculation of work density as well. Mechanical efficiency was calculated using the theoretical cell voltage: overpotentials were ignored, but so was any possible energy recovery. Power density and specific power were limited by overpotentials of the measured fuel cell/electrolyzer [55], with a current limit of 1 A being used for the 25 mm by 25 mm cell. It is important to not that while the actuator can only vary a positive force (since it is producing gas), it's retraction is still controllable by consuming hydrogen gas molecules. Additionally, while this reaction is thermodynamically favorable, creating an effective catch state.

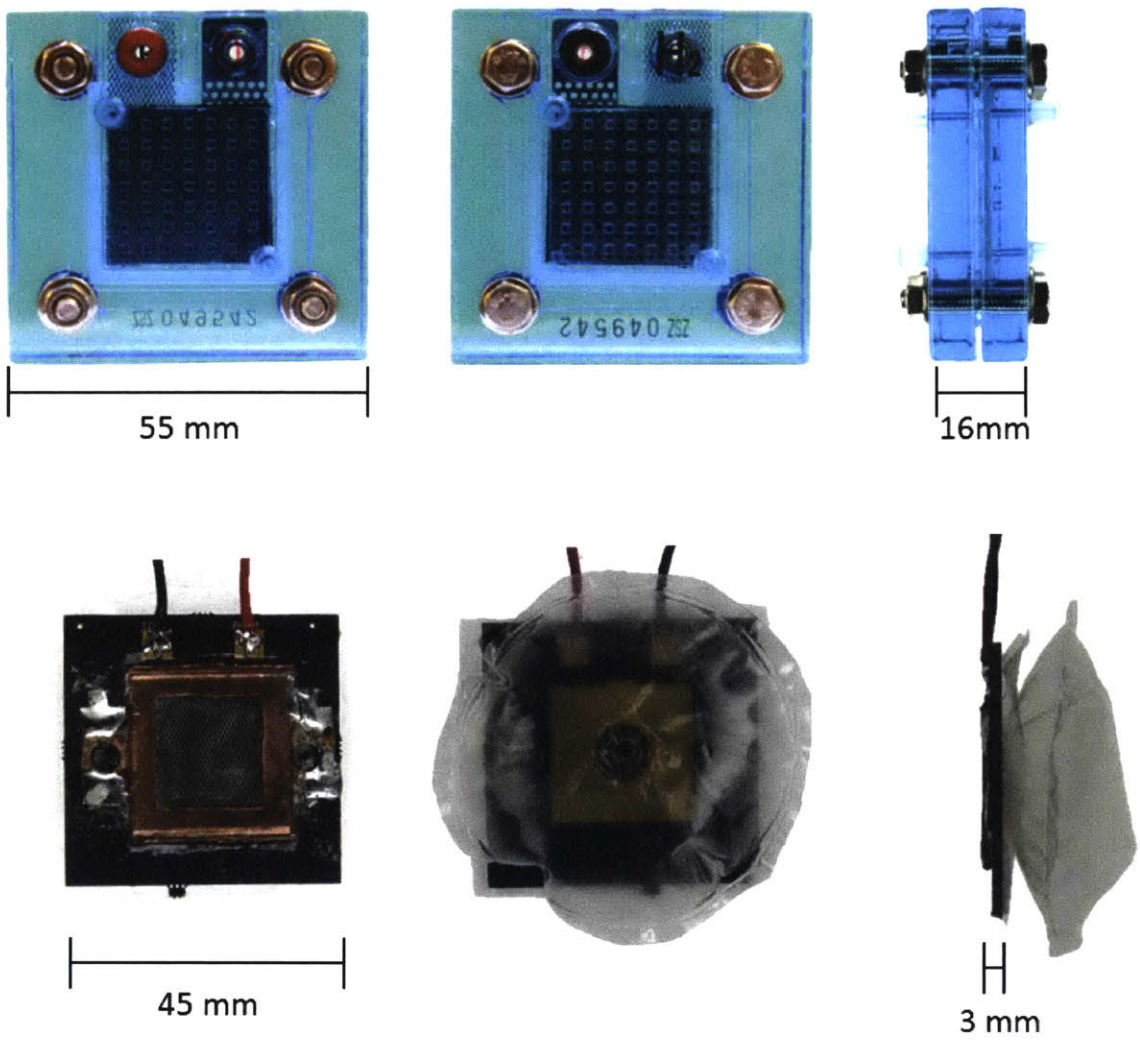

Figure 3-15: Initial attempts toward a thin electrolytic actuator.The PEM assembly from a commercially available fuel cell [55] (top) was repackaged into a much thinner assembly (bottom). Minimum profile height was reduced from 16 mm to 3 mm.

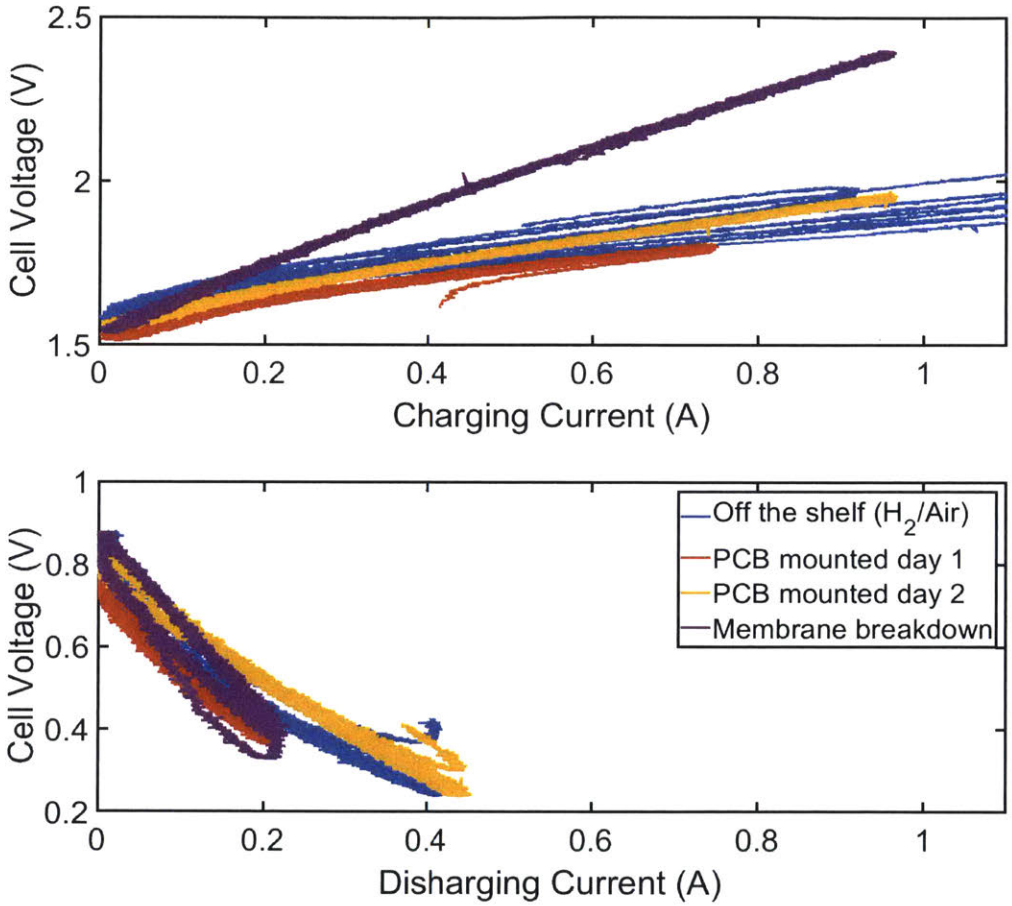

Figure 3-16: Fuel cell performance was tested before and after mounting onto a custom PCB actuator. After 3 days of drying ,fuel cell performance degraded

Metric	Desired Quality	Electromagnetic Actuator	Piezoelectric Actuator	Constant Force Spring	Electrolytic Actuator
Mechanical Efficiency	0.6%	80-90%	1-10%	-	1%
Power Density	0.023 kW/m^3	100 kW/m^3	70 kW/m^3	-	4.1 kW/m^3
Specific Power	0.1 W/kg	200 W/kg	10 W/kg	-	10 W/kg
Work Desnity (10 min cycle)	56 kJ/m^3	20 kJ/m^3	35 kJ/m^3	56 kJ/m^3	5000 kJ/m^3
Max Strain (10 min cycle)	280%	100%	0.1%	2000%	130,000%
Nominal Voltage	< 4 .2 V	< 12 V	> 100 V	Passive	1.2-2.5 V
Controllable in both directions	Yes	Yes	Yes	No	Yes
Catch State	Yes	No	Yes	No	Yes
Smallest dimension	< 10 mm	13.15 mm	3.8 mm	30 mm	5 mm

Table 3.1: Inclusion of Electrolytic actuator in actuator comparisons for NPWT application. Electromagnetic and Piezoelectric specifications were from Hollerbach, et al[50].

Chapter 4

Fluid Management

4.1 Humidity, Moisture, and the Wound Environment

Humidity and moisture of the wound environment is key to wound recovery [57][58]. While a moist wound is helpful, some moderation is needed: A wound that is saturated with water will suffer from tissue maceration, while a wound site that is too dry will inhibit growth of the granular tissue needed for wound healing. One way of controlling the moisture in the wound environment is by tuning the water permeability of the material covering the wound site so that the optimal amount of water is allowed to evaporate from the wound site [59]. This water permability is given by the water vapor transmission rate (WVTR) of the material , which is defined as the amount of water that will evaporate through a membraneof given area over a specific time. Tuning of this water vapor transmission rate is critical to ensure proper wound healing. For murine models, the ideal vapor transition rate has been found to be approximately 2000 g/(m^2 $\times$ 24 hours) [60], which corresponds to an evaporation rate of 6.38 $\times$ 10^{-5} mL/s for a 1.5 $\times$ 10^{-3} m^2 wound area. While the ideal WVTR may be different for human chronic wounds, this was used as a first ballpark for what the ideal WVTR should be.

4.2 Removing the fluid trap

Currently, management of fluid exudate is a limiting factor to the success of NPWT devices [36], as devices must either be constrained to smaller, low exuding wounds, or must have a separate canister to contain exudate. While canister-less NPWT exist [35][42][33][31], they are limited in the materials they can use: they must first collect fluid in the bandage itself, and then allow for evaporation. The materials that are currently used fall short of the desired WVTR (only 600 g/(m^2 $\times$ 24 hours) [61]) , and are unable to evaporate as much fluid as desired. However, the use of evaporation is still key to eliminating the fluid trap and allowing for a self-contained bandage, as not only will it cut down on bandage size, but will relax the power requirements of our pump since it will not have to pump out fluid.

To truly determine whether the fluid trap can be removed, two questions must be answered. First, what are the upper limits of the amount of water that can be removed from the wound site via evaporation? Secondly, can the WVTR of the barrier materials used in NPWT be improved?

4.2.1 Evaporation Rate: Theory

While the thermodynamics of evaporation can be easily found from the heat of vaporization of a liquid, evaporation rate can be much more difficult to find theoretically, as it is affected by so many environmental factors. A common equation for free evaporation to account for both theory and epirical data is the Hertz-Knudsen equation:

$$\frac{dm}{dt} = \frac{\alpha\sqrt{M}(P^*(1-RH))}{\sqrt{2\pi RT}}A, \tag{4.1}$$

where $\frac{dm}{dt}$ is the rate of mass flow of the liquid, α is an experimentally determined "sticking coefficient" ($0< \alpha <1$), M is the molar mass of the liquid molecule, P^* is the equilibrium vapor pressure of the liquid at a particular temperature, RH is the relative humidity of the air ($0< RH <1$), A is the area of liquid that is open to the atmosphere, R is the ideal gas constant, and T is the temperature of the surroundings. It can be found that at a 25 mm diameter opening, at 298 K and 50%

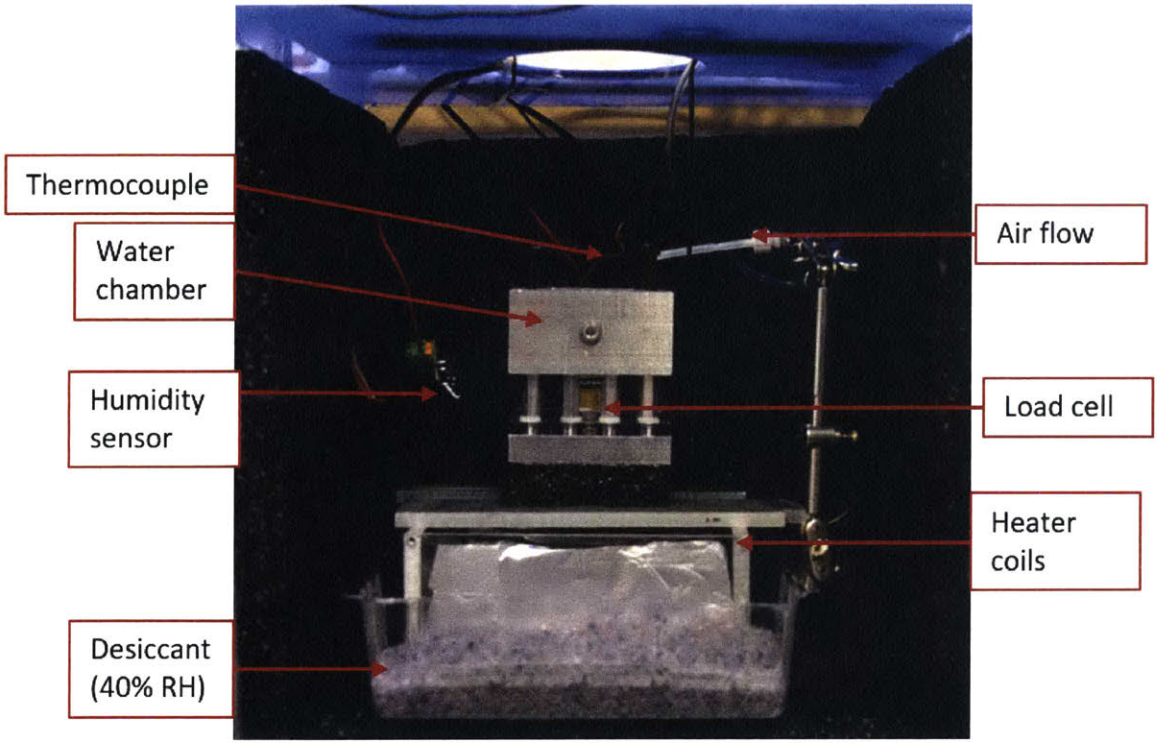

Figure 4-1: Custom environmental chamber used for evaporation testing. Humidity was maintained at 40% using desiccant, and temperature was maintained using a heater coil and thermocouple in closed loop control. Water evaporation was measured as loss of mass from the water chamber by a load cell. The opening of the water chamber was 40 mm in diameter

Relative Humidity, the amount of water evaporated could be from 58.3 to 583,000 $\times$ 10 $^{-5}$ mL/s, depending on the sticking coefficient, α. While this does imply that even in the worst case scenarios, enough water should be able to evaporate from the wound, this large range necessistates experimental measurments.

4.2.2 Evaporation Rate: Experiments

To get a more accurate rate of evaporation rate, a climate control chamber was constructed to ensure repeatably of testings. Relative humidity was maintained at 40% via desiccant and was confirmed by humidity sensor, surface temperature was controlled via a nichrome heating element and thermocouple in closed loop control. Lastly, surface air flow was provided if desired via an motorized air pump. Evaporation rate was measured via a low-load fuel cell.

Evaporation rates were done at 30 °C, 40 °C, and at 30 °C with surface air flow to determine the possible effects on evaporation rate, and if they were necessary for bandage operation.

Conditions	Evaporation rate (mL/s)
30 °	3.33×10^{-5} mL/s
40 °C	8.33×10^{-5} mL/s
30 °C with airflow	14.2×10^{-5} mL/s

Table 4.1: Results from evaporation tests at various conditions. All tests were done at 40 %RH, through a 40 mm diameter container.

It was found that the evaporation rate at 30 °C, 3.33×10^{-5} mL/s , was sufficient for the first pass of the bandage, and no additional work in heating up the water or blowing over the bandage surface was necessary. In the case of a highly exudating wound, excess fluid could be pushed out through the pumping mechanism of the bandage, after which it would be able to evaporate freely.

4.3 Graphene Oxide: the ideal membrane

4.3.1 Need for an ideal membrane

While evaporation of fluid exudate provides an ideal solution to both reduce the pumping power needed by the NPWT pump and eliminating the bulkiness of a fluid trap, the effectiveness of this idea is limited by the barrier properties of the membrane covering the bandage. The ideal membrane for a NPWT bandage would be highly permeable only to water vapor and no other gas molecule. However, a membrane with high permeability to water vapor will usually have high permeabilities to other gas molecules, resulting in an air leak into the wound site.

Fortunatley, recent investigation into the properties of the nanomaterial graphene oxide (GO) have found that its membranes would be the ideal barrier membrane for NPWT. Experiments on graphene oxide sheets have shown nearly unimpeded permeation of water vapor through the membrane, while not allowing for any other gas molecule to pass [62][63].

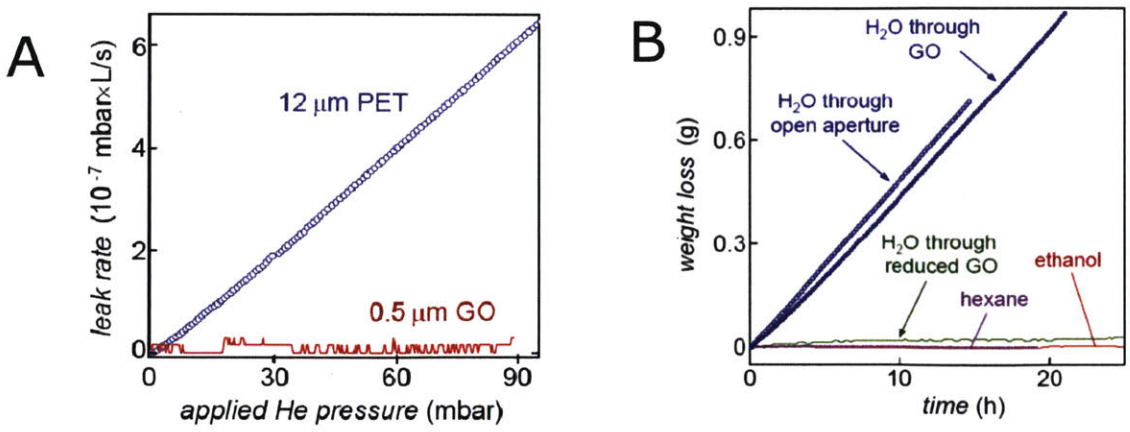

Figure 4-2: Graphene Oxide Barrier Properties as reported by Nair, et al. [62] Most gases, inlcuding Helium ar unable to pass through the GO membranes (A), but water vapor is virtually unimpeded to pass through (B).

The reason for this phenomenon is thought to be explained by the nanostructure of the GO sheets [62]. Graphene is a perfectly flat sheet, two dimensional structure of carbon atoms, and can very easily assemble in stacks of sheets known as graphite through Van der Waal bonds. This results in a space approximately 36 pm [64], too small for gas molecules to pass through [63]. However when graphene sheets are doped with oxygen, the resulting graphene oxide will have small kinks of oxygen molecules above and below the planar sheet of carbon atoms. This causes the spacing of the GO sheets at certain regions to be slightly larger, about 72 pm [65]. It is theorized that water molecules, with both their polarity and size, are just the ideal size to prop open the spaces between the layers of graphene oxide to approximately 84 pm [65], allowing for flow of molecules through the layers [62]. However, other molecules are either too large to pass through the spacing or are unable to prop open these layers to allow for flow of molecules (see Figure4-3).

While there are limitations to the size of GO sheets that can be made, even creating small windows of these membranes in the bandage would allow for evaporation of exudate from the wound site directly, without any loss in negative pressure.

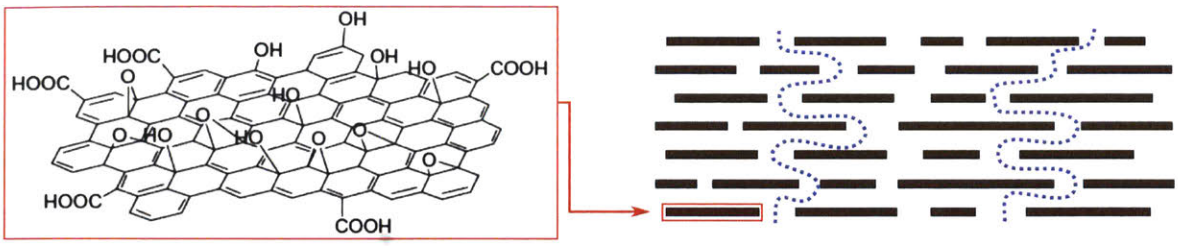

Figure 4-3: Structure of GO sheets. Graphene Oxide sheets have slight imperfections due to the oxide groups bonded to the 2D carbon sheets (left). These sheets stack together imperfectly, creating pores and channels that are the ideal spacing for water molecules to pass through (right). Left image from [66], and right image as adapted from [62]

4.3.2 Fabrication of GO sheets

While graphene oxide will easily for small flakes through the Hummers method [67], getting larger sheets of the material is an area of active research. Potential methods include spin or spray coating [62][63], and vacuum filtration [68][69]. Due to ease of the process, GO sheets were fabricated via vacuum filtration using either 0.22 µm pore-size mixed cellulose ester (MCE) or polycarbonate filters. The slow filtration process allows the suspended GO sheets to slowly form layers across each other, and can be easily made up to 47 mm in diameter [70].

Multiple 25 mm wide GO sheets were made in parallel using a custom setup as shown in Figure 4-4. The thickness of the GO sheets were controlled by the initial concentration of GO solution through the vacuum filtration process. Structure of GO sheets were viewed under SEM, and confirmed using Raman Spectroscopy, by comparing the amplitude the D and G peaks in the Raman spectrum. While the exact ratio may vary on the amount of reduction [71], graphene oxide sheets are indicated by their relatively equal D and G peaks [72][73][74].

GO sheets were then attached via double sided tape to an acrylic spacer. The portion of the acrylic spacer directly below the membrane had small holes to allow the passage of air, and was backed with a coarse glass fiber filter to provide backing for the GO membrane.

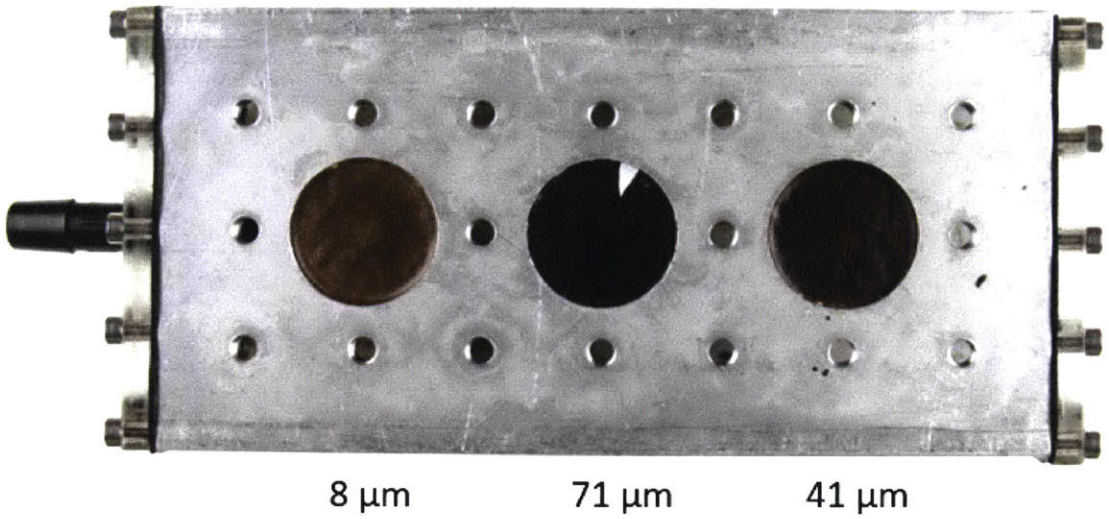

Figure 4-4: Custom vacuum filtration setup. The thickness of the GO membrane made was controlled via initial concentration of GO flakes in the solution

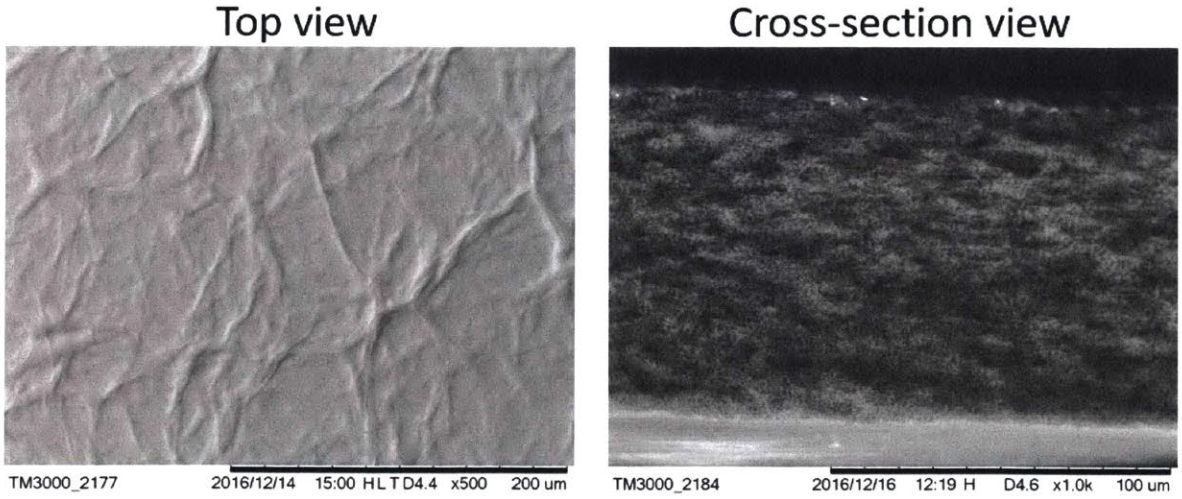

Figure 4-5: SEM (scanning electron microscopy) Image of graphene oxide sheets. Both a planar (left) and cross-sectional (right) view were taken.

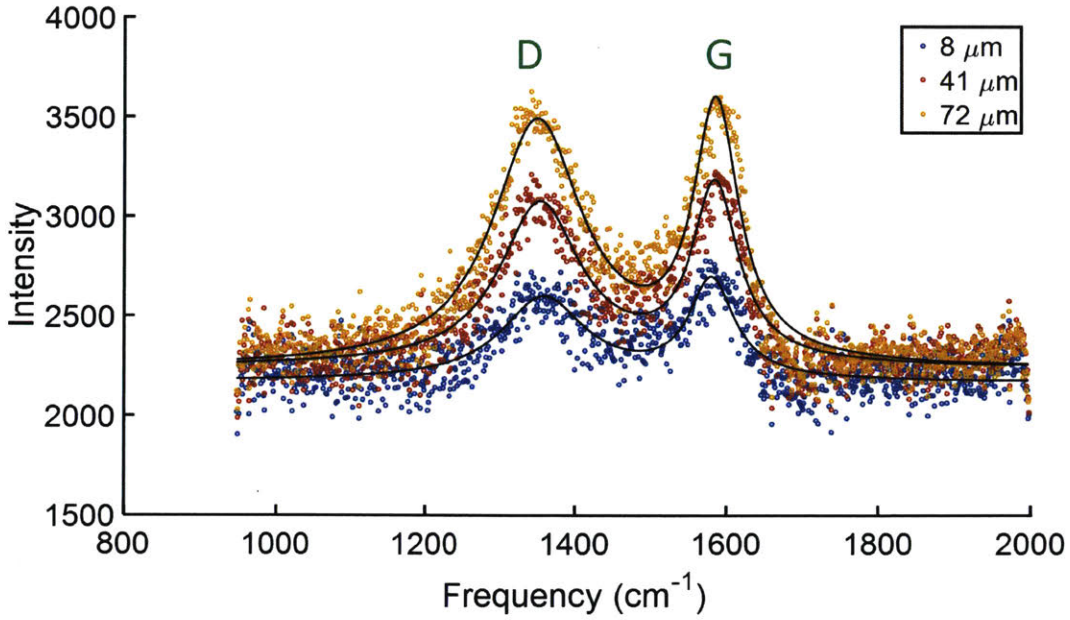

Figure 4-6: Raman spectroscopy of graphene oxide sheets. All sheets exhibited high D band peaks ($1350cm^{-1}$) and G band peaks ($1580cm^{-1}$)

4.3.3 Barrier properties of GO sheets

Pressure integrity

Acrylic spacers with GO membranes were rigidly attached to an aluminum chamber, resulting in a hermetic seal inside the aluminum chamber. The pressure of the chamber was then reduced via retraction of a syringe connected to the chamber, and the internal pressure chamber of the chamber was recorded to determine if any leakage was occurring. As shown in Figure 4-7, no noticeable air leak was found, indicating that the GO membranes were effectively impermeable to air over the time scales desired.

Water transmission

Water transmission rate was compared to free air by placing the GO membrane between two aluminum chambers, one containing a saturated NaCl solution and the other containing a humidity sensor. The air within the chamber with the saturated NaCl solution had a relative humidity of 70 %RH, while the chamber with the hu-

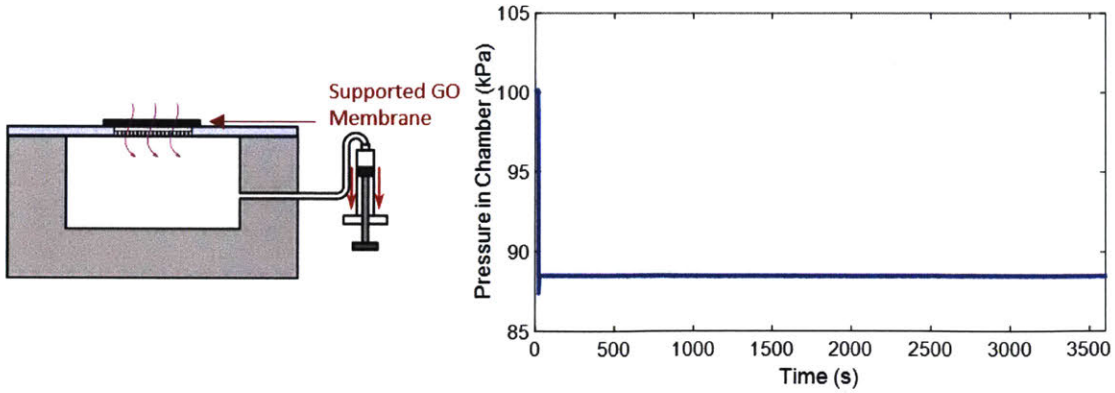

Figure 4-7: Pressure testing graphene oxide sheets. Sheets were supported on an acrylic sheet, and attached to an aluminum chamber (left). Pressure was decreased by retracting a syringe, and the pressure of the chamber was measured over time to assess leakage of gas into the chamber (right).

midity sensor was initially dried to 20 % RH via desiccant. Flow of water vapor over time from the high humidity chamber to the low humidity chamber was measured via humidity sensor. As can be seen from Figure 4-8, the change in humidity of the top chamber over time when a GO barrier was used was similar to that of free air, indicating that the WVTR was quite high.

These results were further confirmed by evaporation tests. One uncovered 40 mm petri dish filled with 5 mL water, as well as one GO-covered dish was placed in a constant temperature oven at 30 °C. The mass of the dish was measured in approximately 1 hour increments. As can be seen from Figure 4-9, while the evaporation rate would vary from day to day, the evaporation rate of the GO membrane ($1.95 \pm 0.56 \times 10^{-5}$ mL/s) was consistently 80% of free air ($2.5 \pm 0.83 \times 10^{-5}$ mL/s).

High humidity environments

One possible risk was that in high humidity environments, the presence of water molecules would prop open the channels between the GO sheets to allow for other gas molecules to travel as well. There has been some work suggesting helium permeability increases at high humidity environments [62]. Pressure integrity at high humidity environments was tested by repeating the pressure integrity tests with a saturated

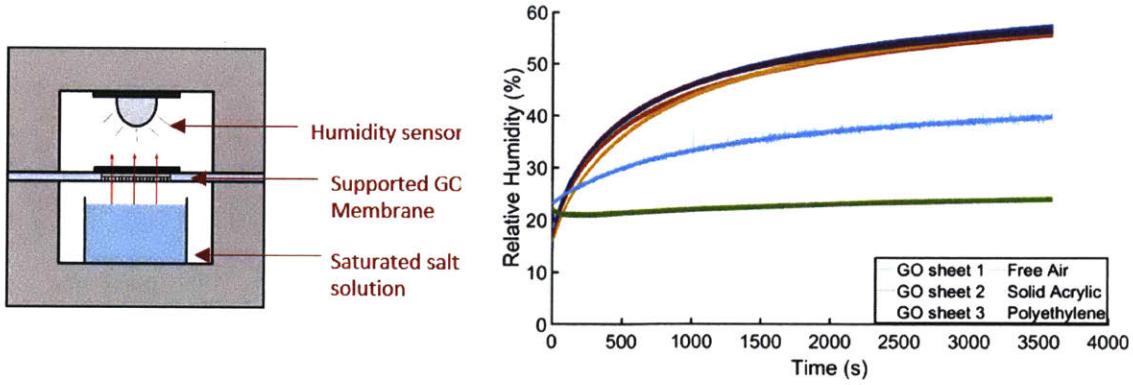

Figure 4-8: Water vapor transmission rate testing (WVTR)of graphene oxide sheets. Sheets were supported on an acrylic sheet, and attached between an aluminum chamber containing a saturated NaCl solution and an aluminum chamber containing a humidity sensor (left). Change in humidity in the top chamber was measured over time (right). Solid acrylic and Polyetheylene sheet, and free air was also tested.

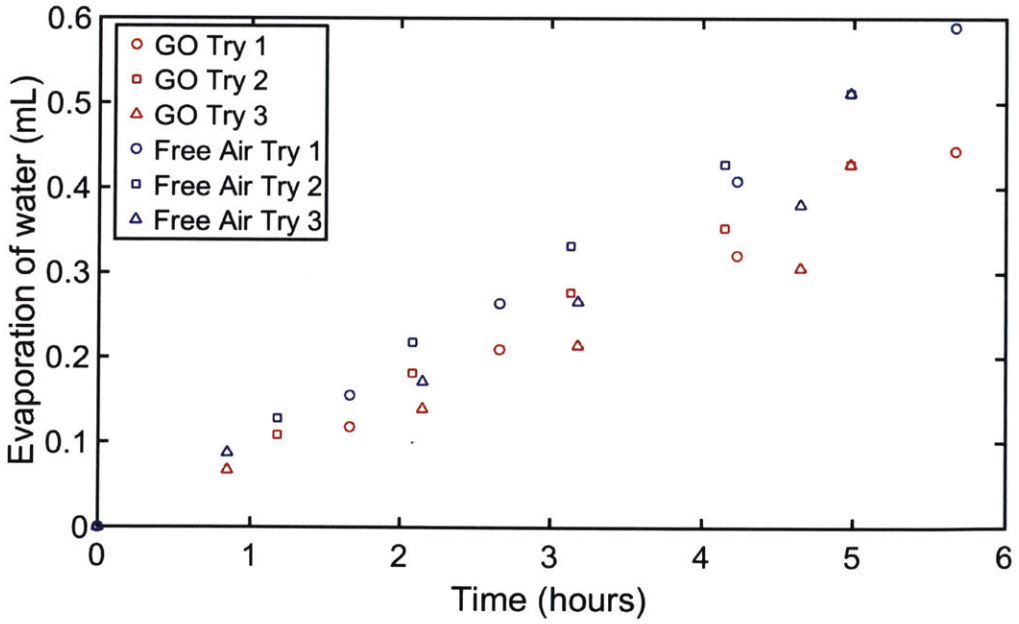

Figure 4-9: Evaporation studies of GO versus free air. 5 mL of water were kept both in a free air container, as well a GO-covered container. Both containers were kept in a 30 °C oven, and the mass of the container and water was measured approximately every hour.

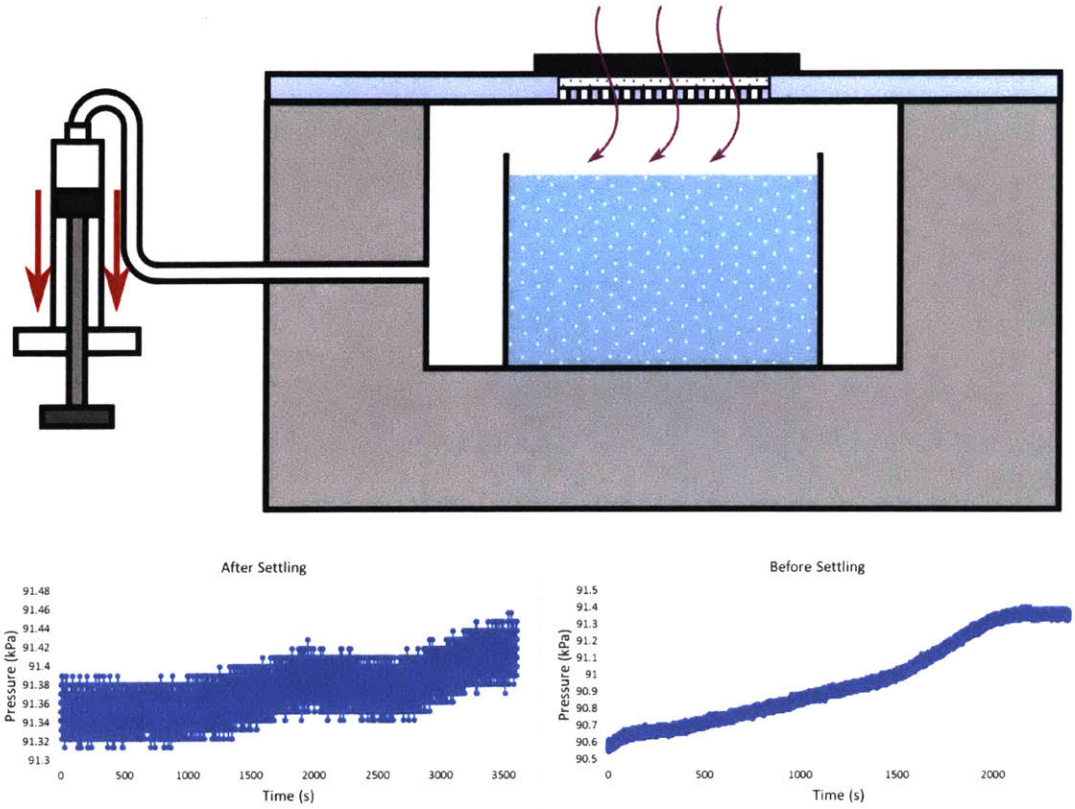

Figure 4-10: Pressure testing Graphene Oxide sheets at high humidity. Sheets were supported on an acrylic sheet, and attached to an aluminum chamber containing a saturated NaCl solution, and pressure was decreased by retracting a syringe (top). After an initial settling period (bottom right), the pressure in the chamber was constant (bottom right).

NaCl solution placed in the chamber.

After an initial increase in pressure due to adjustment of the NaCl solution to a lower pressure, the pressure in the chamber did not change. This may be because the majority of gas molecules in the chamber were oxygen or nitrogen molecules, rather than very small helium molecules.

Fortification against water

Another large risk is the possible breakdown of GO sheets in water. While it was initially unclear why some GO sheets would dissolve in water, while others would maintain integrity, it was determined that small impurities of aluminum from the filtration process provided cross-linking of the GO sheets to prevent breakdown. A

soaking process of aluminum nitrate [70] after the filtration of the GO solution into the water was shown to maintain integrity when submerged in water with light shaking.

4.4 Conclusions

After testing both free water evaporation rates, and confirming the barrier properties of graphene oxide first reported by Nair et al. [62], it can be determined that evaporation is a sufficient way to handle fluid exudate from the bandage. First it was confirmed that the free evaporation rate at 30 °C would be enough to handle the majority of fluid exudate. Next, the barrier properties of graphene oxide, specifically its water vapor transmission rate, and general gas permeability, were confirmed in the lower pressure, high humidity conditions of NPWT, indicating that it would be the ideal barrier material for use in NPWT. The majority of exudate would be able to evaporate freely though any GO windows in the NPWT devices, while excess fluid would be pumped outside the bandage, and be able to evaporate freely as well.

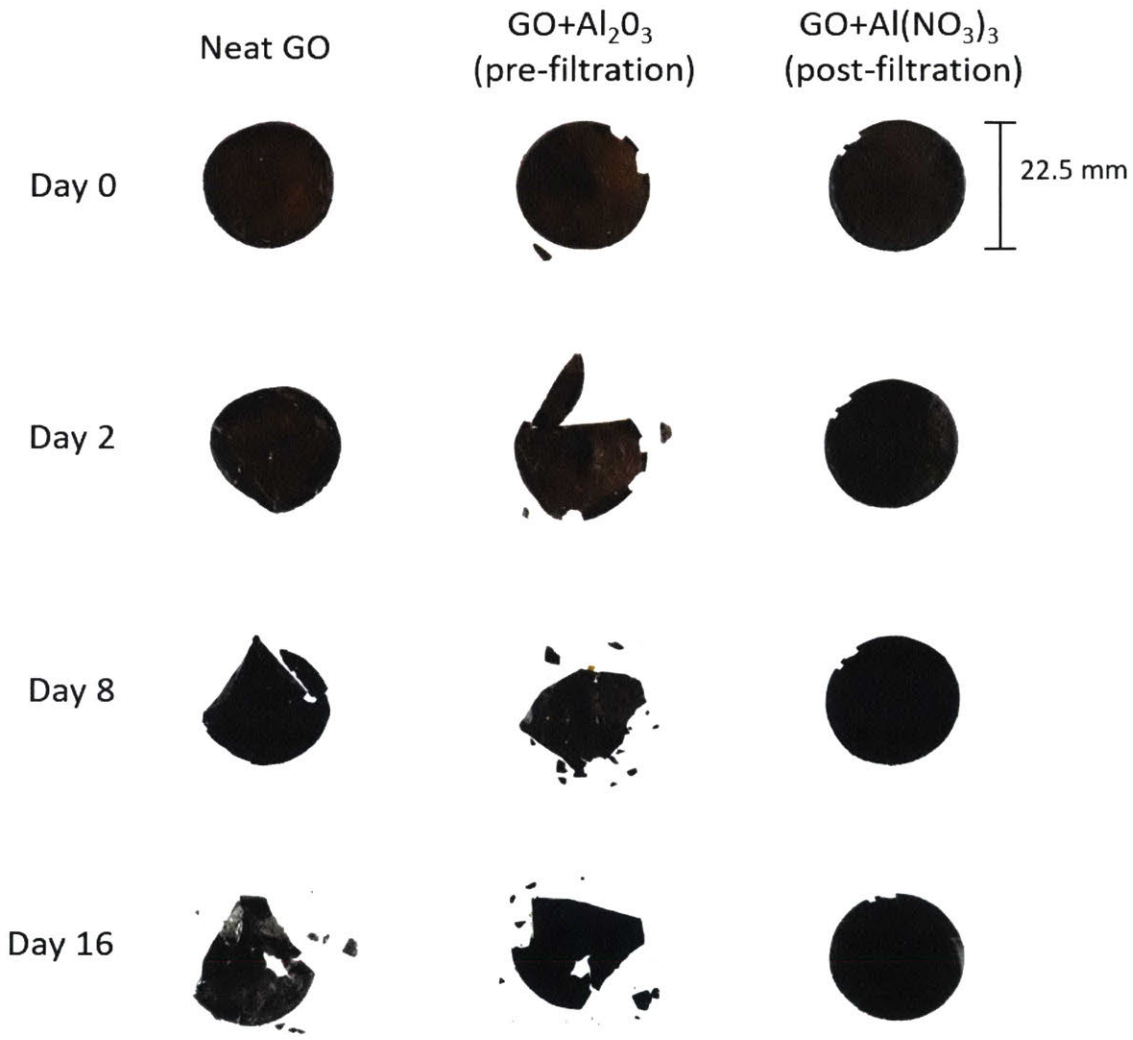

Figure 4-11: Integrity of graphene oxide sheets in water. Neat GO Sheets, and pre-filtration AlNO3-GO flake mixture, and post-filtration AlNO3 soaked GO sheets were left in water with light shaking. Neat GO sheets broke down by 1 week, and pre-filtration AlNO3 mixed sheets broke down within a day. Post-filtration AlNO3 soaked sheets did not break down.

Chapter 5

Device Construction and Improvements

5.1 Proposed device operation

The proposed device is as follows (see Figure 5-1): First foam filler and the bandage are applied to the wound bed. Once the bandage has been pressed against the skin to create a seal, hydrogen production of the electrolytic actuator will begin, expelling air from the bandage-wound environment as the bellow expands. Once the bellow is fully expanded, it will begin fuel cell operation, consuming the produced hydrogen, and reducing the pressure within the bandage-wound site. As air leaks into the bandage, the bellow can continue to retract to maintain negative pressure. Conversely, expanding the bellow will raise the pressure in the bandage-wound site if variable pressure therapy is desired.

The design of this bandage followed many iterations, each one testing and sequentially incorporating both improvements from the chapters before, as well as other design decisions that will be explained in greater depth here.

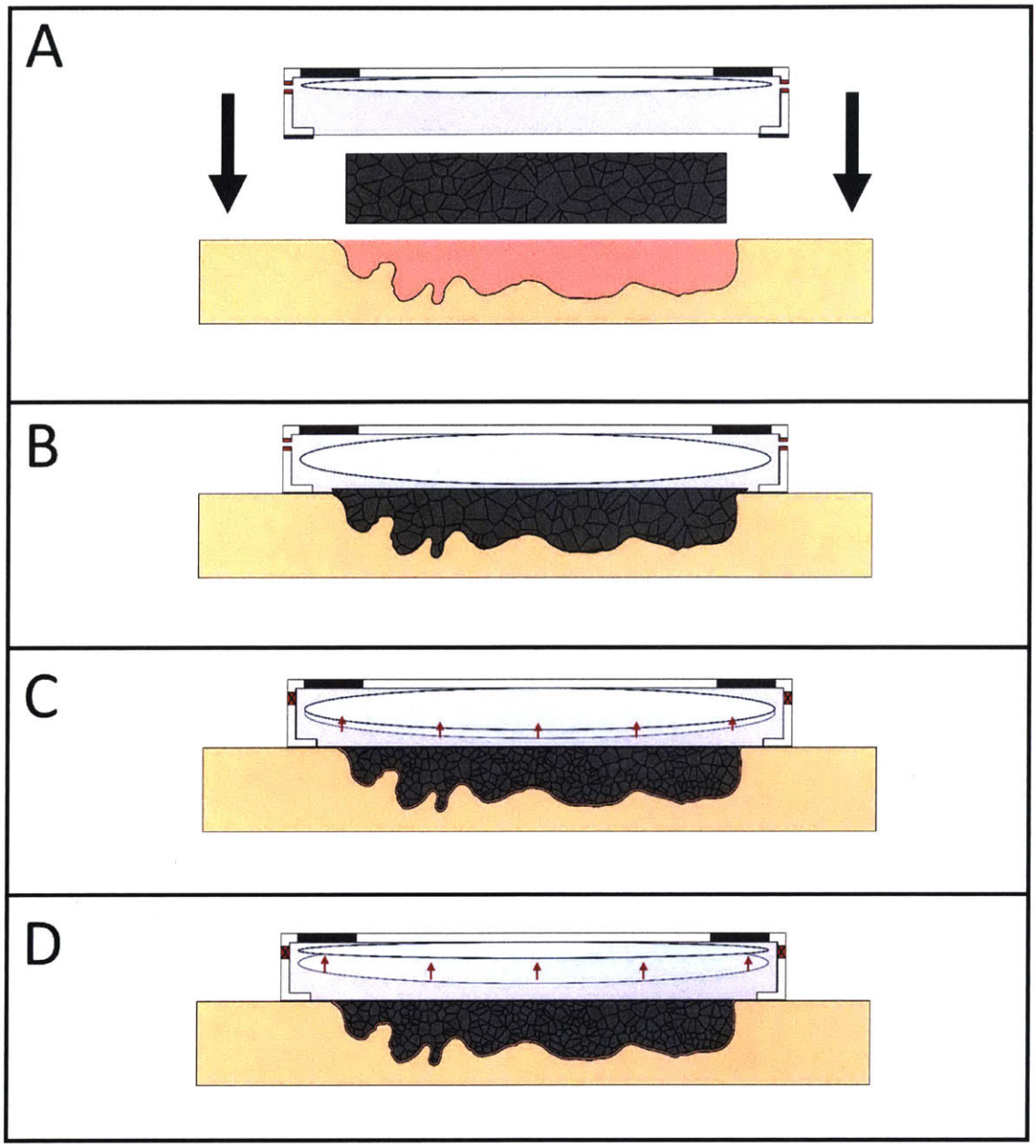

Figure 5-1: Negative pressure generation mechanism. (A) Foam and bandage are applied to wound bed. Air can escape as the bandage is pressed down due to passive check valves. (B) After attachment, the gas chamber is expanded via electrolysis. Passive check valves are forced open meaning displaced gas can freely exit the wound cavity. (C) As hydrogen production ends the gas chamber is retracted via fuel cell operation. As chamber volume decreases, pressure inside the wound site decreases as well. Energy is recovered in this process. (D) As air leaks into the bandage, the gas chamber can be further retracted via fuel cell operation, further recover energy from the stored hydrogen.

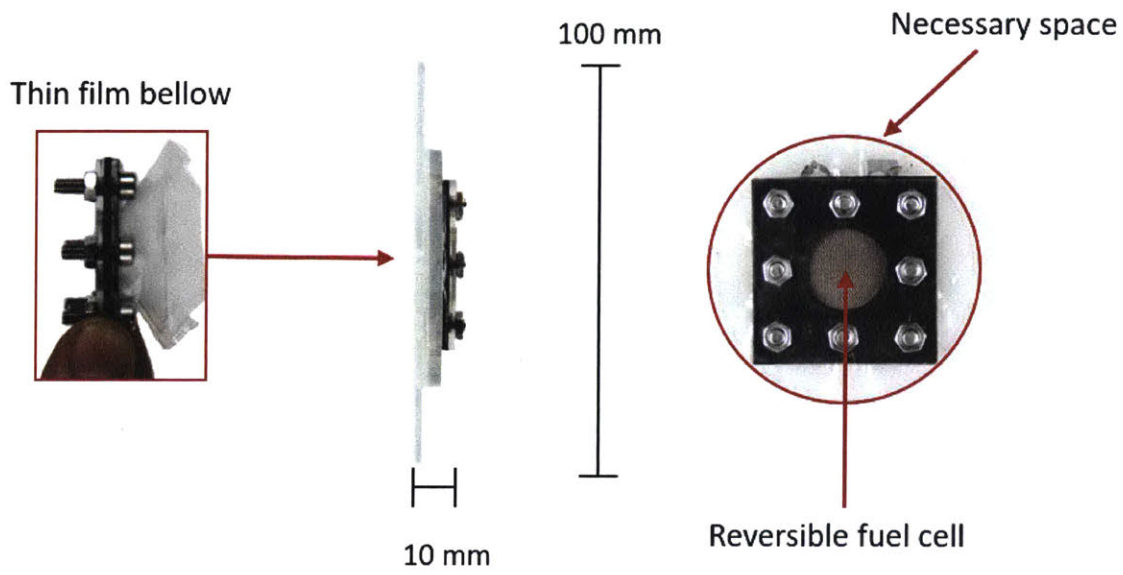

Figure 5-2: Prototype for Iteration 1. A rigid 3D-printed structure was made with a PEM assembly clamped directly to the bandage.

5.2 Iteration 1

5.2.1 Initial Construction

A first iteration of this device was created to test the capability of bellows and actuator to create the negative pressure in the desired space. A 10 mm tall bandage structure was printed, and a PEM fuel cell assembly was mechanically clamped directly to the a single convolution, polyethylene bellow. This assembly was attached directly to the 3D printed bandage, and the entire bandage was clamped to an acrylic spacer representing a 20 mL of wound area. Control of the fuel cell was done via a switch between a power supply and a bleed resistor.

5.2.2 Iteration 1 Results

This first iteration showed the ability of the pumping mechanism to create the desired negative pressure, as well as provide variable pressure therapy within a small profile. However, as can be seen in the final cycles of Figure 5-3, leakage of hydrogen gas reduced the ability to provide variable pressure for many cycle. This leakage could

be attributed to both the mechanical sealing of the bellow, as well as the leakage of hydrogen through the polyethylene bellow. Additionally, this iteration was able to achieve success because the polyethylene bellow was able to squeeze into space of the wound bed. While this may be have potential in the future as a potential replacement to granular foam filling the wound bed, it was deemed undesirable. Lastly, check valves had not yet been added to the device preventing device reset.

5.3 Iteration 2

5.3.1 Check valve design

A check valve is a passive valve that allows for flow of air in only one direction. These valves are normally preloaded to be nominally closed, and a certain amount of pressure (cracking pressure) is needed to overcome the preload on the valve and allow passage of air through the valve. This preload is either provided by a weighted mass, such as the case in a ball valve, or a stretched spring elastomer, as is the case in a diaphragm valve. This preload provides the sealing force, which prevents gas leakage when the valve is closed [75]. Generally, a high preload (and sealing force) results in a higher cracking pressure of the valve, as a greater force will be needed to overcome the higher preload.

As mentioned in Chapter 2, it was critical to have a check valve with extremely low cracking pressure, while still maintaining low leakage. While the relationship between leakage rate and sealing pressure is complex, leakage rate will generally decrease with sealing pressure [75]. Thus the first design criterion was that he check valve must have enough of a preload to prevent gas leakage. To reduce the cracking pressure as much as possible, geometric advantages were utilized. Specifically, by utilizing larger areas over which the cracking pressure could be applied, and using beam-bending like techniques to maximize the strain on the valve, the cracking pressure could be kept low while having sufficiently high sealing pressures and low leak rates. Two custom shaped check valves were created through which the preload was provided via

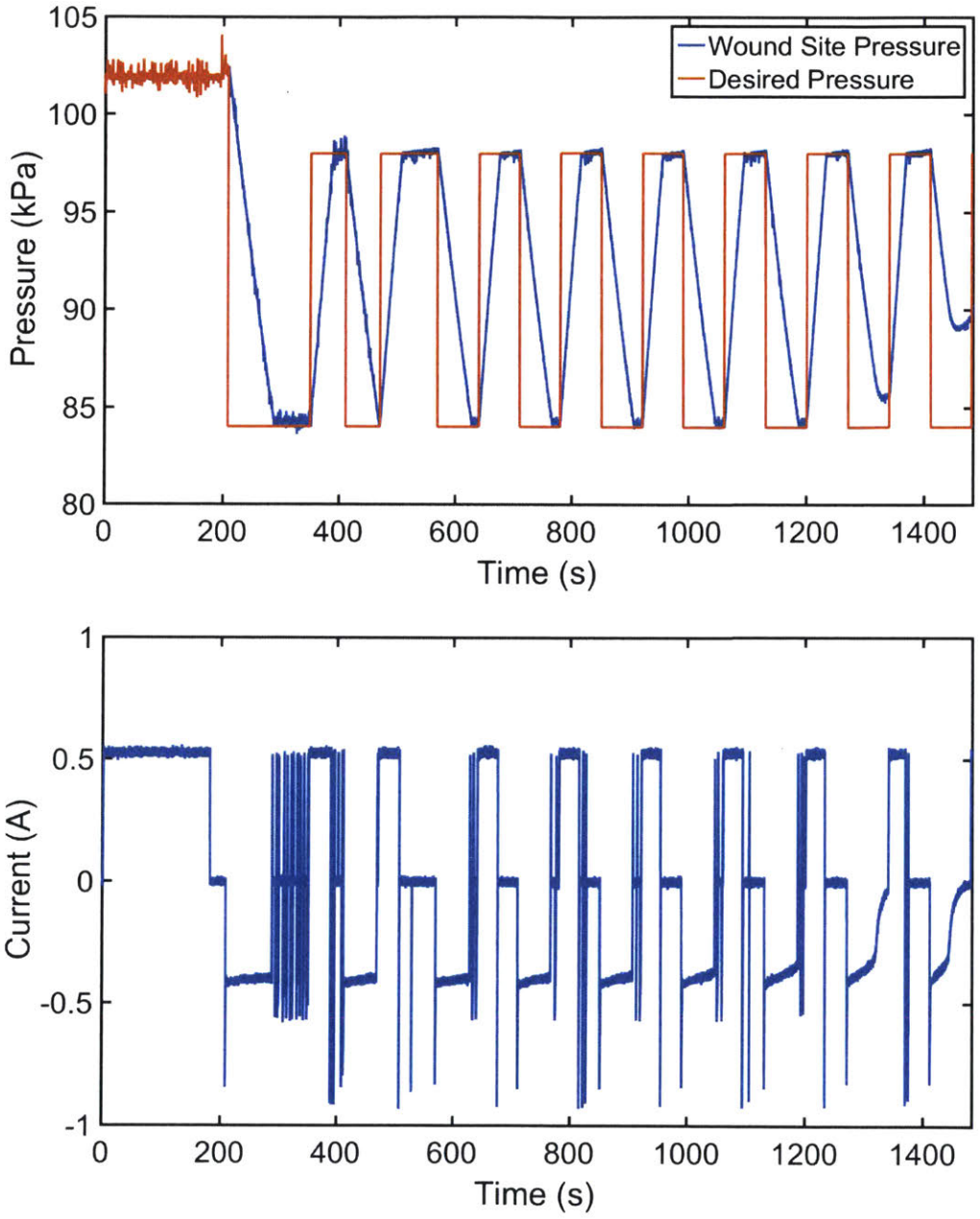

Figure 5-3: Experimental results of iteration 1. Fuel cell was charged directly though a power supply and then pump was connected to a 20 mL wound volume phantom after it was fully inflated. In reverse pump operation, fuel cell was discharged through a bleed resistor. Closed loop control to determine when the desired pressure was reached.Variable pressure application was also demonstrated

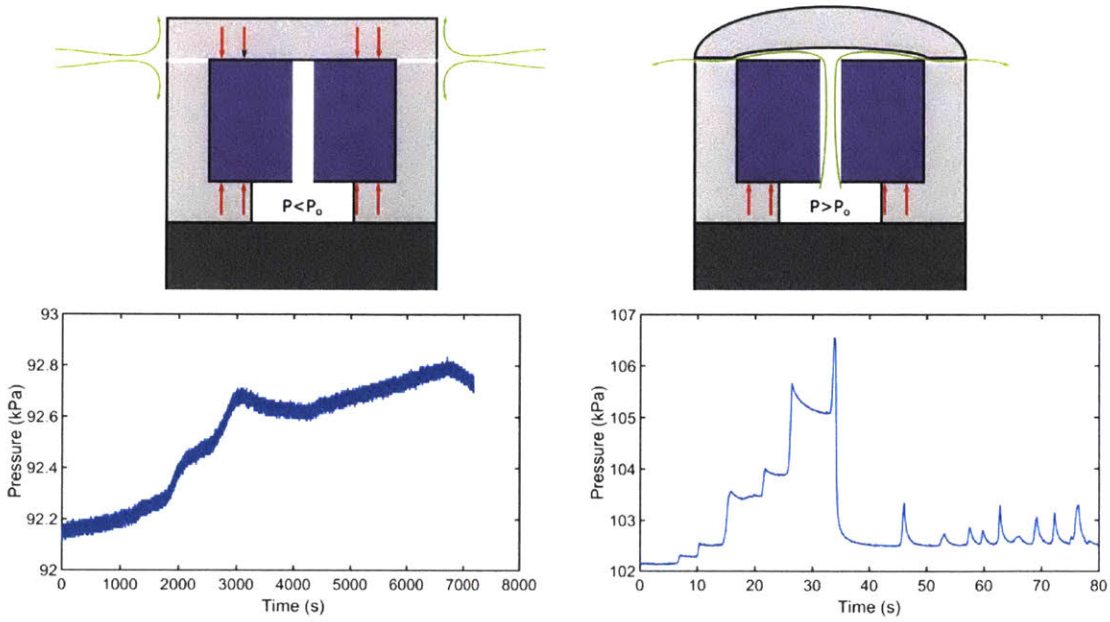

Figure 5-4: Check valve design 1. When the pressure in the chamber is less than the cracking pressure (top left), the chamber is hermetically sealed (bottom left). When the cracking pressure increases, the top of the elastomeric seal deforms and allows air to pass through the sides. (top right).After an initially high cracking pressure, the subsequent cracking pressure was found to be less than 4 kPa.

stretching of an elastomeric membrane over rigid acrylic structure.

Design 1

The first design was made through stretching an elastomer membrane in the axial direction over an acrylic disc. Air could pass through the acrylic disc, but could not pass through the elastomer unless it lifted the elastomer to escape through the sides. This valve was prototyped using Smooth-On Ecoflex 50 silicone [56] ,and was success full in providing a cracking pressure of 4 kPa without any noticeable gas leakage.

Design 2

A second check valve design was made by stretching an elastomeric ring in the radial direction around an acrylic ring. Air was allowed to escape radially by deforming the elastomeric membrane and passing through the side. The cracking pressure could be tuned by adjusting the width of the channel when it was in contact with the elastomer

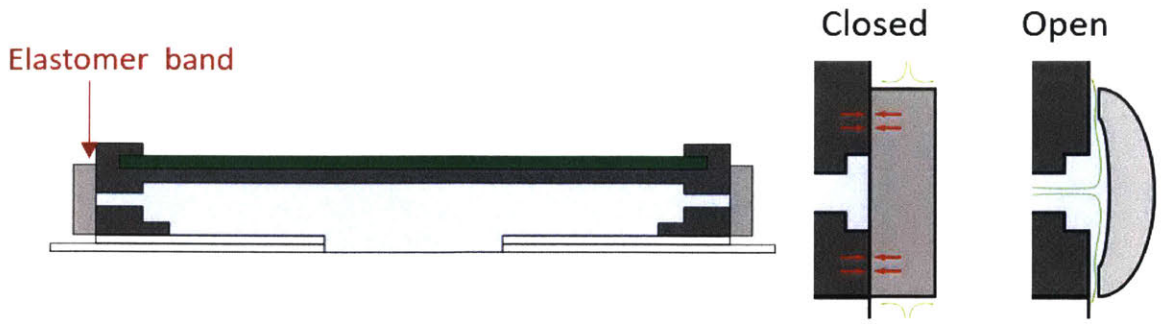

Figure 5-5: Check valve design 2. An elastomer band is stretched around the bandage so that it seals any air channels (left). When the pressure in the chamber is less than the cracking pressure (middle), the chamber is hermetically sealed. When the cracking pressure increases, the center of the elastomeric ring is deformed, allowing air to escape through the top and bottom of the band (right) Tuning the width of the groove at the elastomer interface will tune the cracking pressure of the seal.

seal. Increasing the width of this channel increased the contact area of the gas with the seal, reducing the cracking pressure necessary to deform the elastomeric seal, as seen in Table 5.1

Groove Width	Cracking Pressure (kPa)
No Groove (1 mm hole)	2.5-3.5
2 mm	1.2-1.7
4 mm	1.3

Table 5.1: Tuning of Check Valves. Varying the groove size directly at the elastomeric seal interface was used to lower the cracking pressure as desired.

5.3.2 Low profile fuel cell integration and integrated sensing

In between iterations, the fuel cell clamping was improved to the low profile actuator style as mentioned in Chapter 3. This thin profile actuator was bonded directly to a sensor board PCB in a monolithic structure as seen below:

Additionally, both pressure and humidity sensing was added to this design for closed loop control on pressure. While this design reduced profile thickness, the monolithic design proved difficult to manufacture, as failure of any component part would require reassembly of the entire bandage.

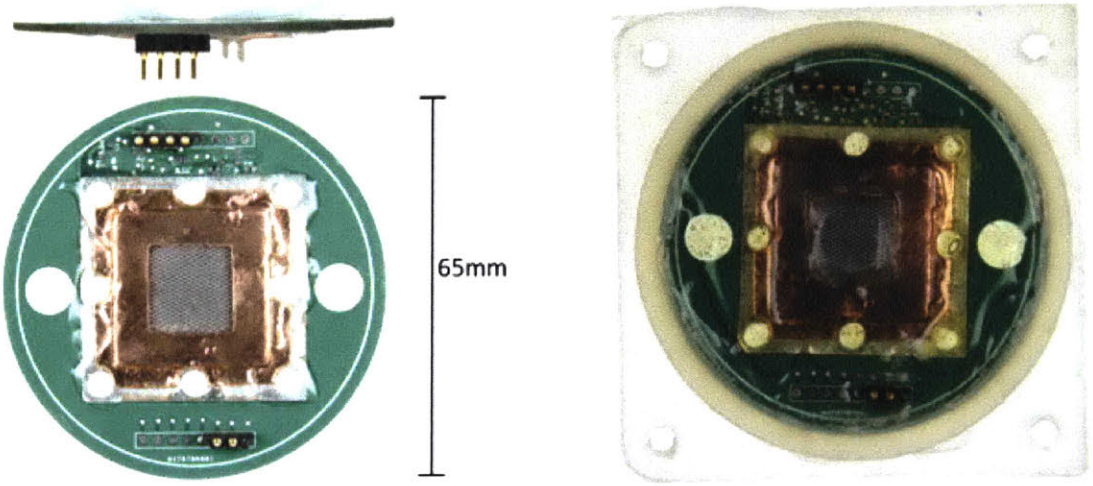

Figure 5-6: Iteration design 2. A custom PCB with integrated fuel cell and bellow mechanism, as well as pressure and humidity sensing was attached to a flexible bandage structure.

5.3.3 Flexible structure

To integrate check valve design 1, a flexible structure for the bandage was made of Ecoflex 30 Silicone [56]. The silicone was allowed to stretch around the flexible PCB, allowing for a venting function similar to that shown in check valve design 1.

5.3.4 Iteration 2 Results

Unfortunately, this iteration was not able to reach pressures desired for two reasons. Two possible reasons contributed to this failure. First, the flexible silicone base of the bandage noticeably deformed, contributing to pumping inefficiency. Secondly, a single convolution bellows was used, resulting in a much lower fill factor, which also contributed to pumping inefficiency.

Investigation into bandage stiffness

To test the hypothesis of bandage stiffness contributing to loss in pumping efficiency, the stiffness of the pump structure was added to the model of the pump. The constitutive equations were originally

$$P_w[V_w + A_p(h_{max} - f_p h)] = P_{atm}[V_w + A_p h_{max}(1 - f_p], \tag{5.1}$$

where as before, P_w is the wound (and bellow) pressure, A_p is the area of the bellow, f_p is the space filling efficiency of the bellow, h_{max} is the maximum height of the bellow, h is the current height of the bellow, P_{atm} is the atmospheric pressure, and V_w is the volume of the wound. However, now the constitutive equation becomes

$$P_w[V_w + A_p(h_{max} - f_p h)(1 + \frac{P_w - P_{atm}}{K(P_w)})] = P_{atm}[V_w + A_p h_{max}(1 - f_p], \tag{5.2}$$

where K is the bulk modulus of bandage material.Thsi equation implies that part of the work done by the bandage when retracting the bellows goes to compression of the bandage structure, rather that soley reducing the pressure at the wound site, meaning that pump will be less effective in reducing pressure. The Ecoflex 30 material was tested in a Dynamic Mechanical Analyzer (DMA), and its stress-strain relationships were incorporated into simulations to determine their effect on negative pressure generation. As can be seen from Figure 5-7, the inclusion of bandage deformation explained most of the deviation from origninally modeled behavior.

5.4 Iteration 3

5.4.1 Multiple Convolution Bellows

Bellow manufacturing techniques were improved to allow for multiple convolutions and geometries with more convolutions, as explained in Chapter 2. By switching to multi-convolution bellows, the fill factor, f_p of the bellow was improved from 0.57 to 0.85, as measured via video analysis (see Figure 5-8).

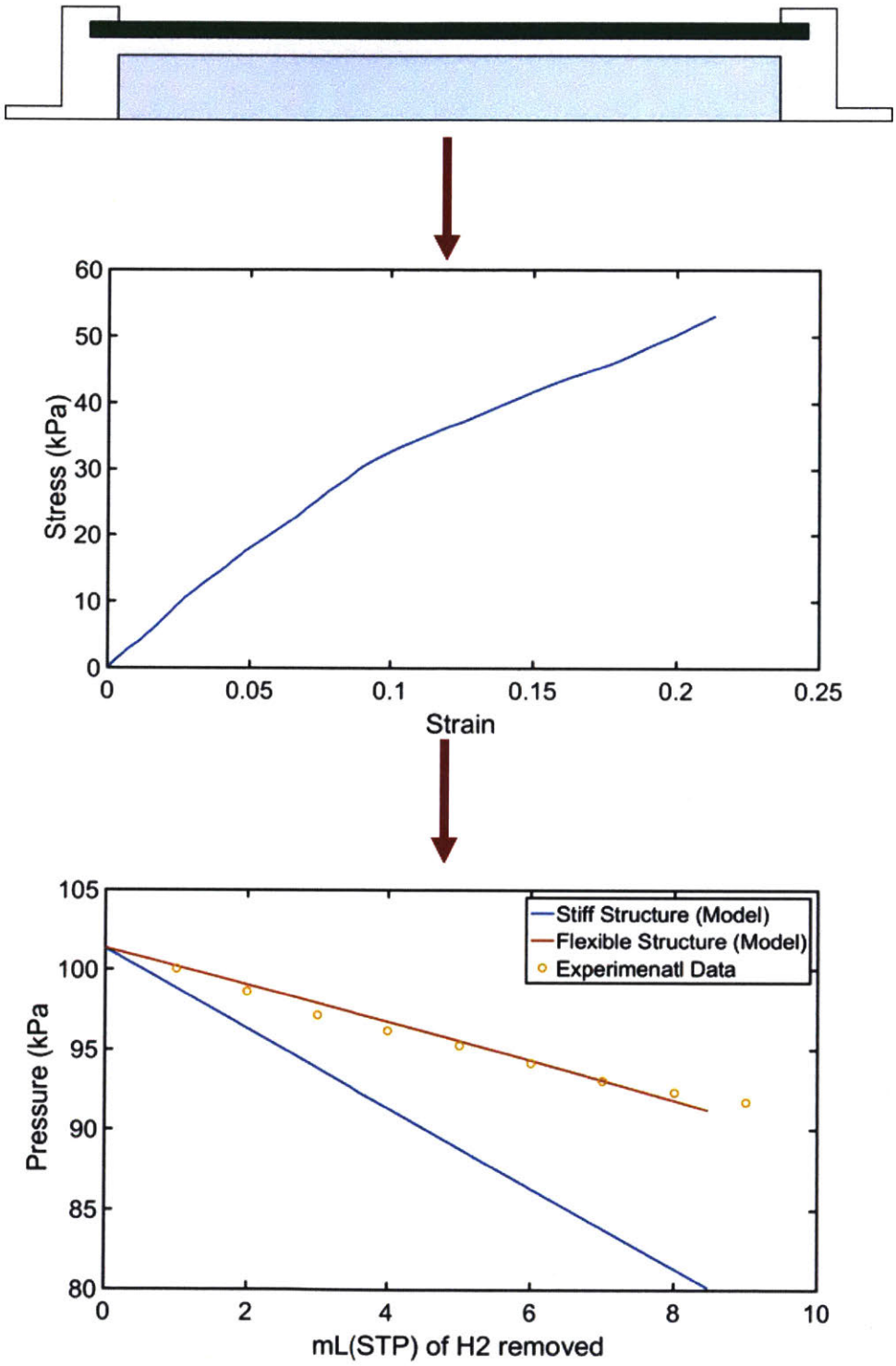

Figure 5-7: Effect of flexible bandage structure (top) on pressure generation. Stress-strain of silicone material (middle) was incorporated to a model and compared to experimental results (bottom)

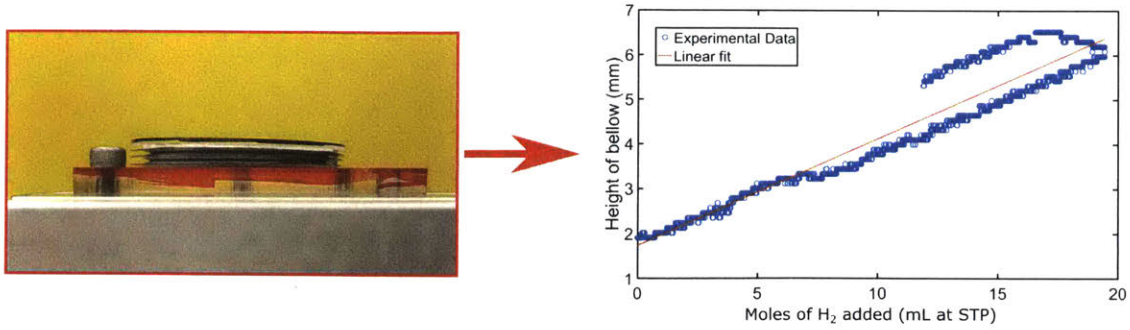

Figure 5-8: Measurements of Bellow Expansion. Video analysis was used to determine the height-to-gas added relationship of the multiple convolution bellow

5.4.2 Bandage structure

The bandage was now switched back to a rigid structure design. To allow for flexibility in wound application, a soft flexible layer could be added to the bottom of the bandage to allow for large radius of curvature, as shown in Figure 5-9:

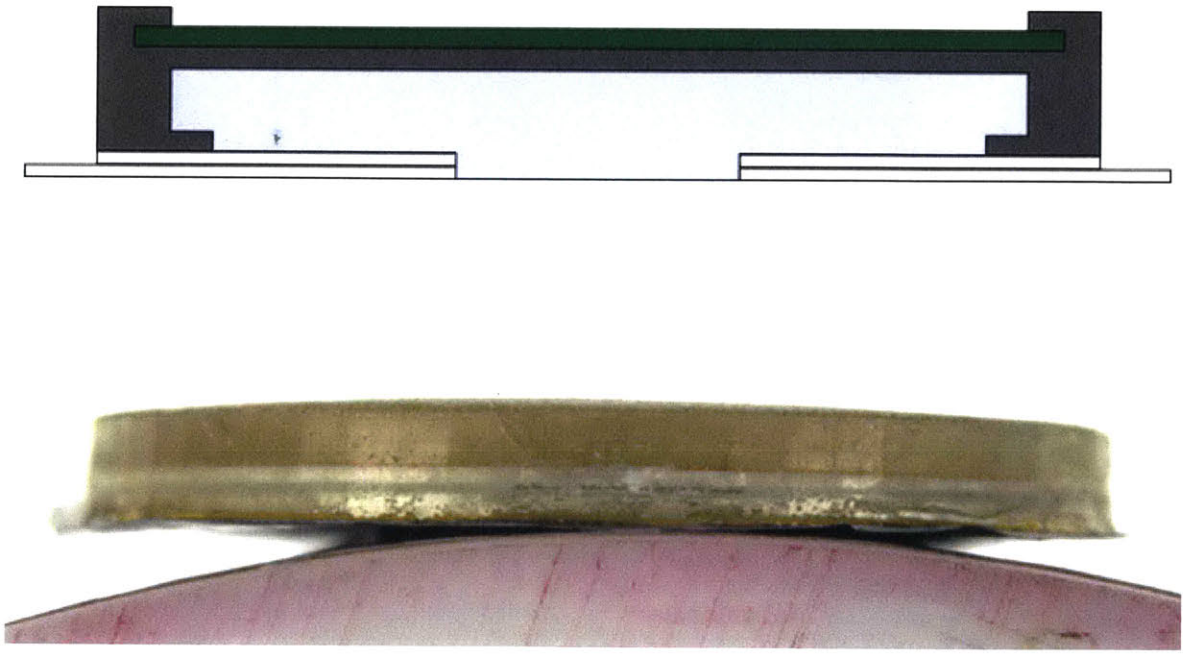

Figure 5-9: Rigid bandage design. A bonded sheet below the rigid component allows for flexible application of the bandage.

5.4.3 Check valve design

Check valves were not made following check valve design 2, in which the solid acrylic ring would be the structural base of the bandage.

5.4.4 Energy Recovery

To improve efficiency, energy recovery circuitry was implemented. Traditionally, hydrogen fuel cells provide a challenge in energy recovery due to there low cell voltage (1.2 V) compared to that of other energy storage technologies, such as lithium ion (4.2 V). To overcome this potential difference, fuel cells are usually kept in series as a stack to increase the voltage to a usable level. Because a voltage stack would be too bulky to implement, a DC-DC type switching boost converter was used to recover charge from the fuel cell to the battery, while a separate buck converter was used to charge the fuel cell. The resulting I-V characteristics are shown in Figure 5-10. The switching converter seems to be performing at least as well as the standard discharge characteristics of the fuel cell.

Both the duty cycle to current relationship (Figure 5-11) and duty cycle to efficiency were measured as well (Figure 5-12). Fuel cell to battery charge transfer efficiency dropped to 40% at high currents. While this is acceptable for a first pass, this can be improved in further iterations by further tuning of inductor sizes, and more precise controlling of MOSFET switching.

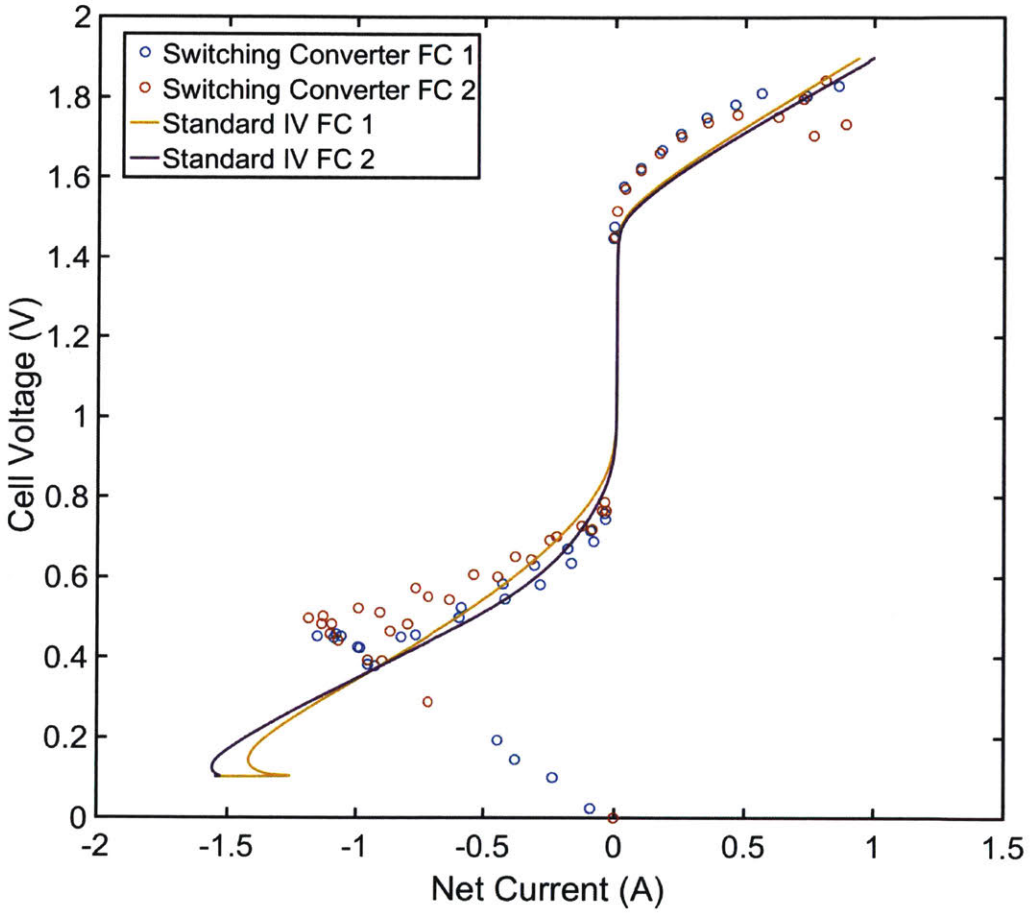

Figure 5-10: I-V characteristics of the switching circuitry versus standard chage/discharge of the fuel cell. Switching circuitry mostly followed I-V behavior of standard charge/discharge

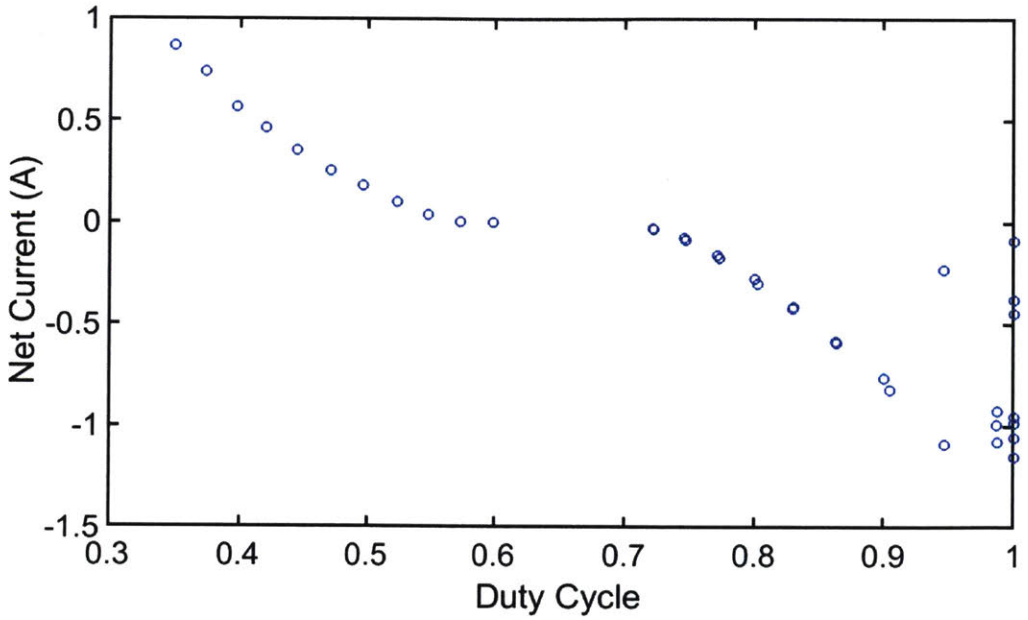

Figure 5-11: Switching duty cycle in buck and boost converter versus current. Positive currents corresponded to fuel cell charging, and negative currents corresponded to fuel cell discharging.

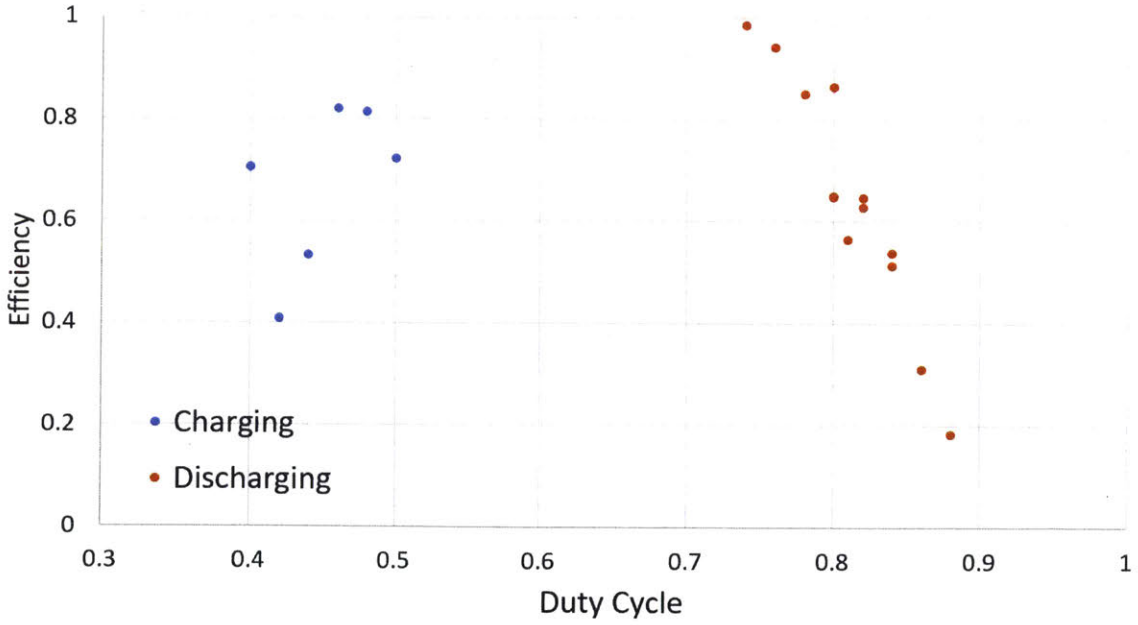

Figure 5-12: Efficiency of switching circuitry to transfer charge from the fuel cell to the lithium ion battery. Blue dots indicate charging of fuel cell and discharging of battery via buck converter, and orange dots indicate discharging of fuel cell and charging of the battery via a boost converter

5.4.5 Iteration 3 Results

To separate the effects of each addition to the base design, this design was tested modularly, with the electronics and check-valve as a separate component that could be swapped in as desired. The results are discussed as follows, and will be summarized in Table 5.2.

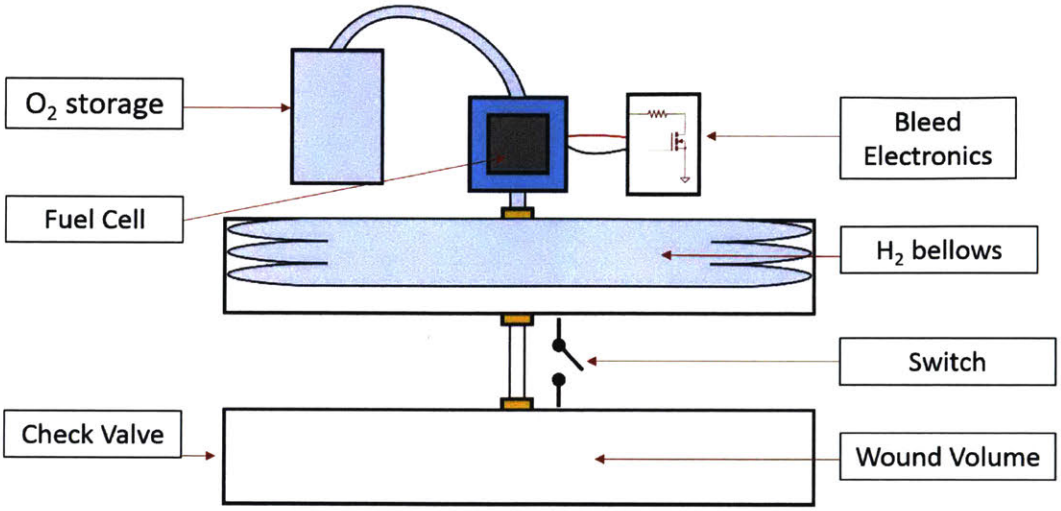

Figure 5-13: Experimental setup of base case of iteration 3. Fuel cell was charged directly though a power supply and then pump was connected to a 20 mL wound volume phantom after it was fully inflated. In reverse pump operation, fuel cell was discharged through a bleed resistor. Closed loop control to determine when the desired pressure was reached.

Base Case

For the base case, the multiple convolution bellows pump was attached to a PEM fuel cell assembly for hydrogen storage. A power supply was used to provide the desired current to expand the bellows system. Once the bellows system was fully expanded, it was connected to a 20 mL chamber used to represent the wound volume. To reduce pressure, the bellow was retracted by running the fuel cell in reverse through a bleed resistor. The entire setup can be seen in Figure 5-13. and a representative data set is shown in Figure 5-14. Te device was successful in creating the desired pressure l (82.4 $\pm$ 0.2 kPa), and still had 5 mL of H_2 remaining for further reduction of pressure. The pressure rate was 0.19 $\pm$ 0.04 kPa/s, and needed 185 $\pm$ 16 J to create the desired

pressure. Once taking into account that the actuator still had 5 mL more of travel, the total work that could be performed would be 0.14 J, resulting in an overall efficiency of approximately 0.076%.

Energy Recovery Circuitry

Next, the bleed circuitry was replaced by energy recovery circuitry, while the rest of the assembly was kept the same (see Figure 5-15). Once again, the device was successful in creating the desired pressure differential of 81.7 ± 0.5 kPa (see Figure 5-16). The rate of pressure decrease was the same as before (0.18 ± 0.02 kPa/s), and the device had still had 5 mL of H_2 still available for further reduction of pressure. However now that energy could be recovered, the total energy when the additional 5 mL of H_2 is used would be 152 ± 12 J, resulting in an efficiency of approximately 0.092 %.

Check valve results

Next a check valve following design 2 was added to the system (see Figure 5-17). As can be seen from Figure 5-18, the device was still able to reach the desired pressure. The flow rate of the pump did not change significantly from before (76.6 ± 16.8 × 10^{-3} mL/s before to 76.6 ± 6.0 × 10^{-3} mL/s after), indicating that there was little noticeable leakage from the check valve ($p > 0.05$). However the amount of energy requirement of the device did increase due to the additional cracking pressure of the check valve, meaning that the energy if the chamber was fully utilized would be 161 ± 9.5 J, resulting in an efficiency of approximately 0.087%.

Variable Pressure Therapy

The base case was also used to test the ability of variable pressure therapy (see Figure 5-19). Similarly to iteration 1, the device was able to provide variable pressure therapy from 82 to 95 kPa, at a rate of 0.19 ± 0.04 kPa/s, significantly faster than the necessary rate (0.06 kPa/s).

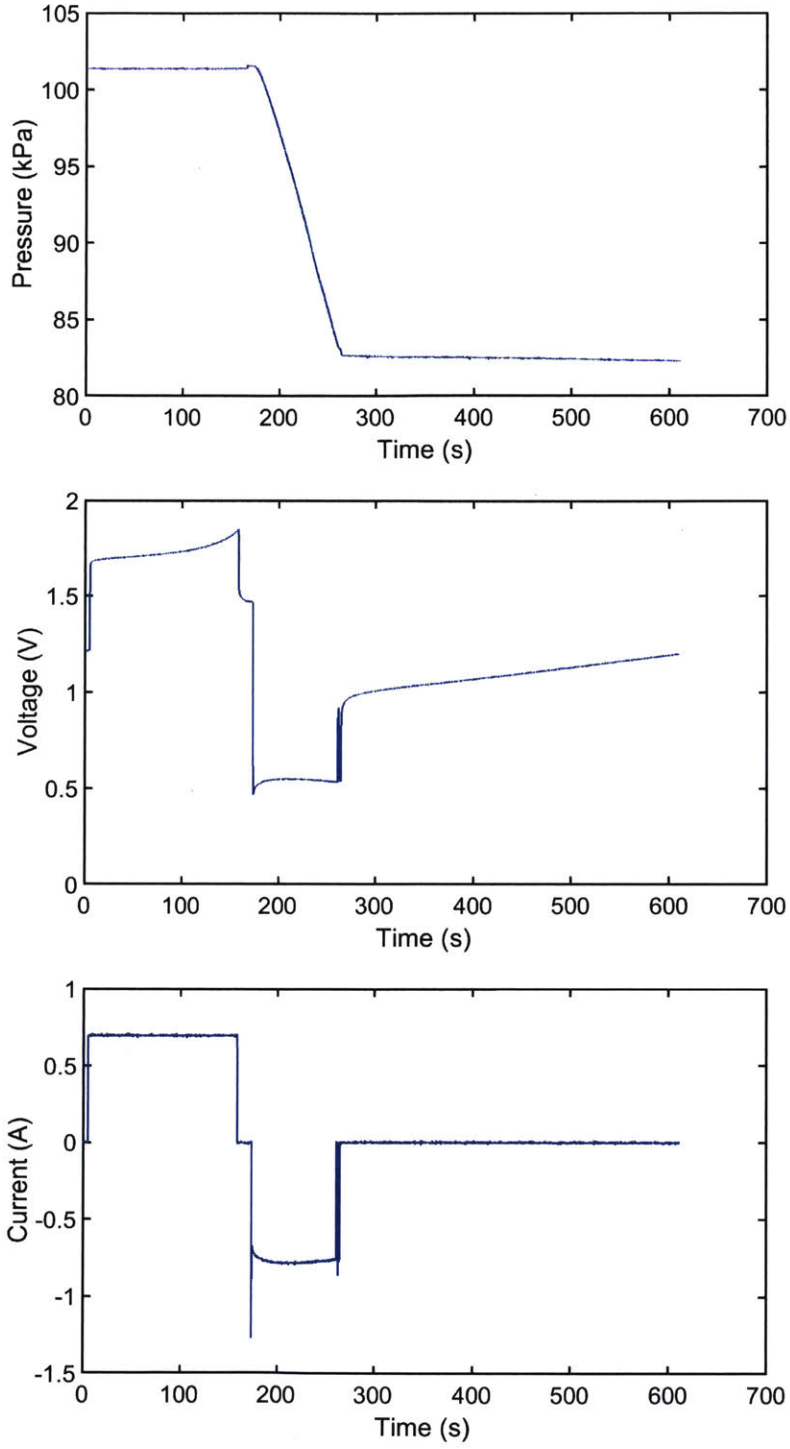

Figure 5-14: Experimental results of base case of iteration 3. Fuel cell was charged directly though a power supply and then pump was connected to a 20 mL wound volume phantom after it was fully inflated. In reverse pump operation, fuel cell was discharged through a bleed resistor. Closed loop control to determine when the desired pressure was reached.

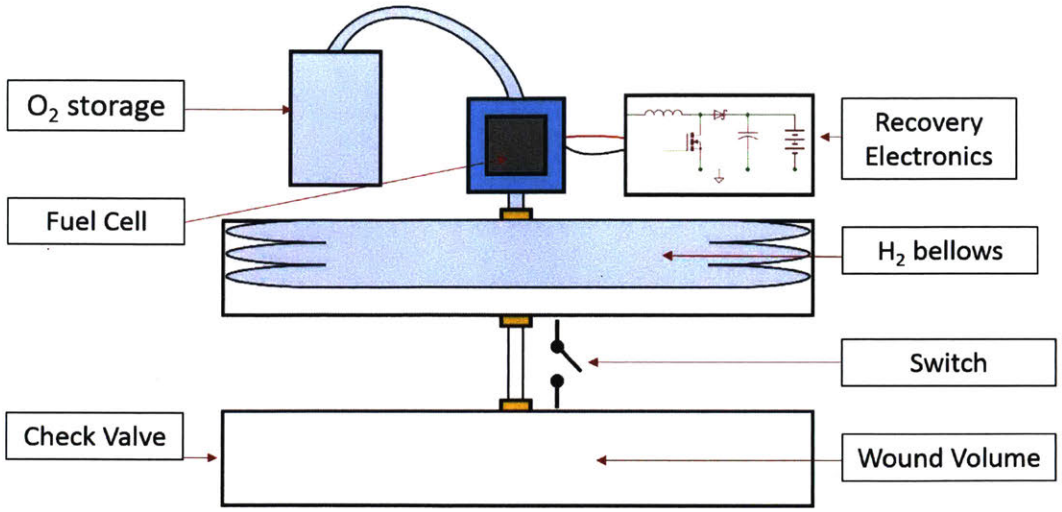

Figure 5-15: Experimental setup of iteration 3 with energy. Fuel cell was charged by battery via buck converter and then pump was connected to a 20 mL wound volume phantom after it was fully inflated. In reverse pump operation, fuel cell was discharged via boost converter back to battery. Closed loop control to determine when the desired pressure was reached.

Leak testing

The final device was tested at both at a high leak rate to simulate worst case scenarios. A leak rate was created through an adjustable needle valve (see Figure 5-21). The high leak rate was measured to be 66.7 $\times$ 10^{-3} mL/s at the lowest pressures (85-90 kPa) , while average leak rate was 25.0 $\times$ 10^{-3} mL/s (85-100 kPa).As can be seen in Figure 5-21, the current device is less successful at these faster leak rates. While it is able to reach 84-86 kPa (-125 mm Hg), it can only hold this pressure for about 5 min before it must be restarted. Current failure in the device was a combination of hydrogen depletion due to recombination of hydrogen with oxygen in the dead space of the actuator, and flooding of the fuel cell after excessive running of the fuel cell.

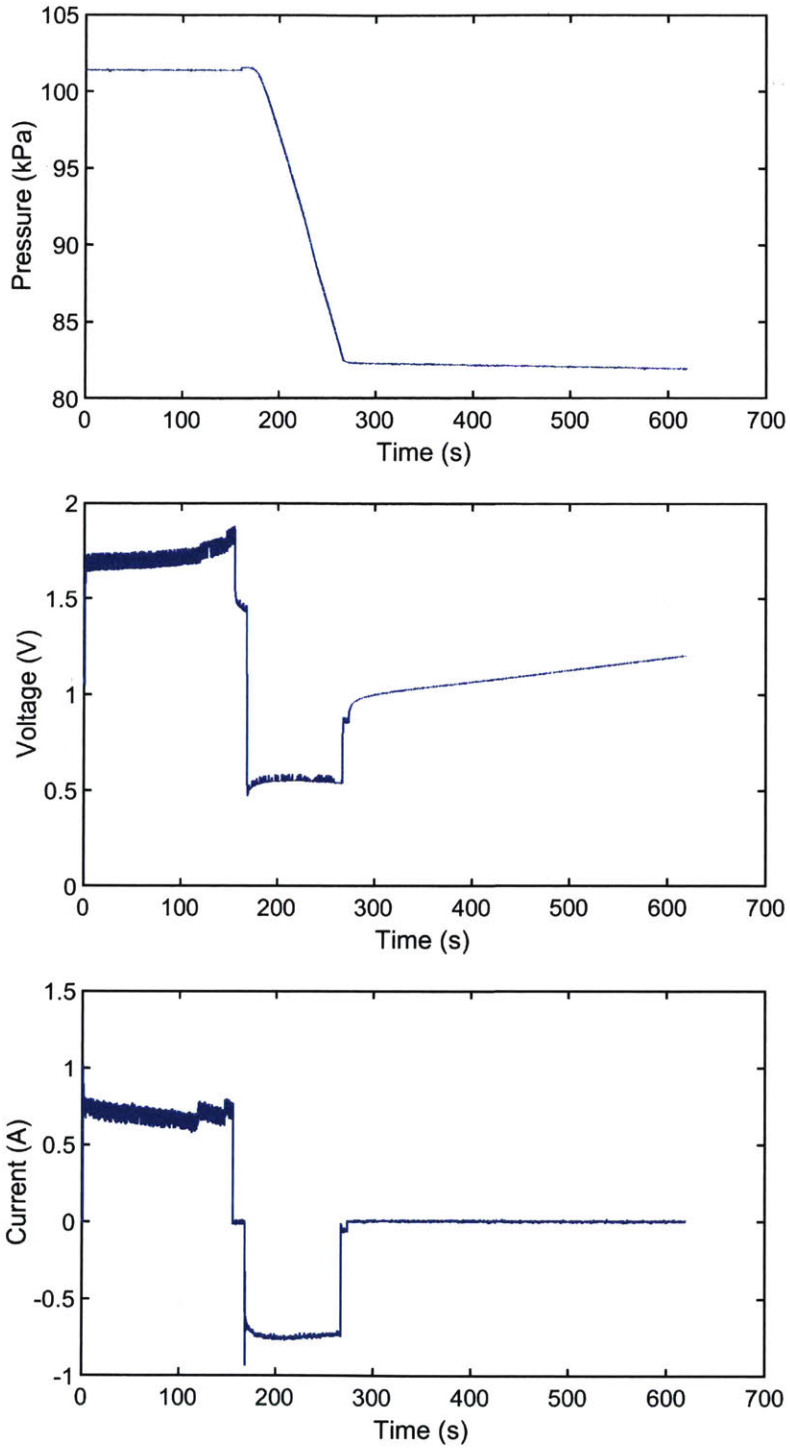

Figure 5-16: Experimental results of iteration 3 with energy recovery. Fuel cell was charged by battery via buck converter and then pump was connected to a 20 mL wound volume phantom after it was fully inflated. In reverse pump operation, fuel cell was discharged via boost converter back to battery. Closed loop control to determine when the desired pressure was reached.

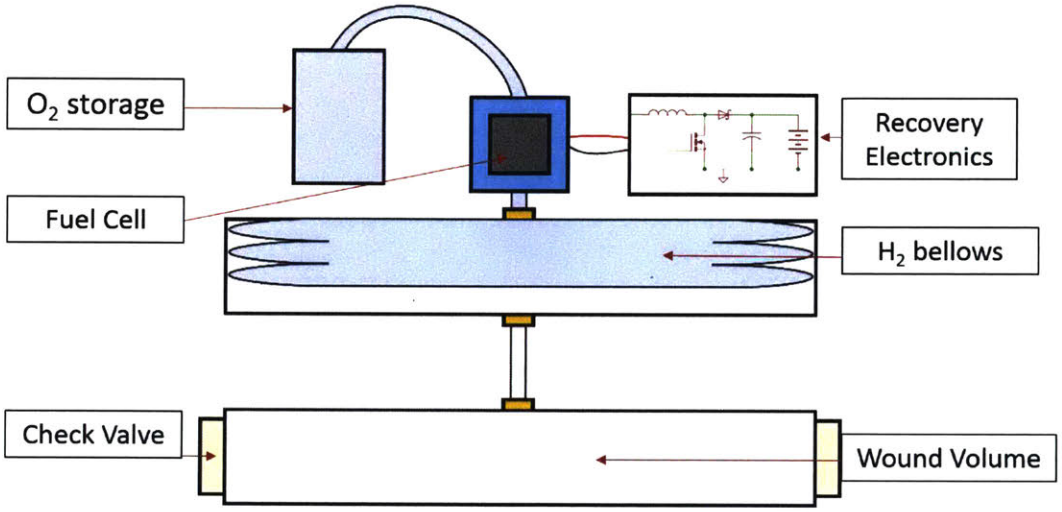

Figure 5-17: Experimental setup of iteration 3 with energy recovery and check valve. Fuel cell was charged by battery via buck converter, and pump was continuously connected to the 20 mL wound volume phantom, and a check valve (design 2) was incorporated to allow for air to escape when bellows were expanding. In reverse pump operation, fuel cell was discharged via boost converter back to battery. Closed loop control to determine when the desired pressure was reached.

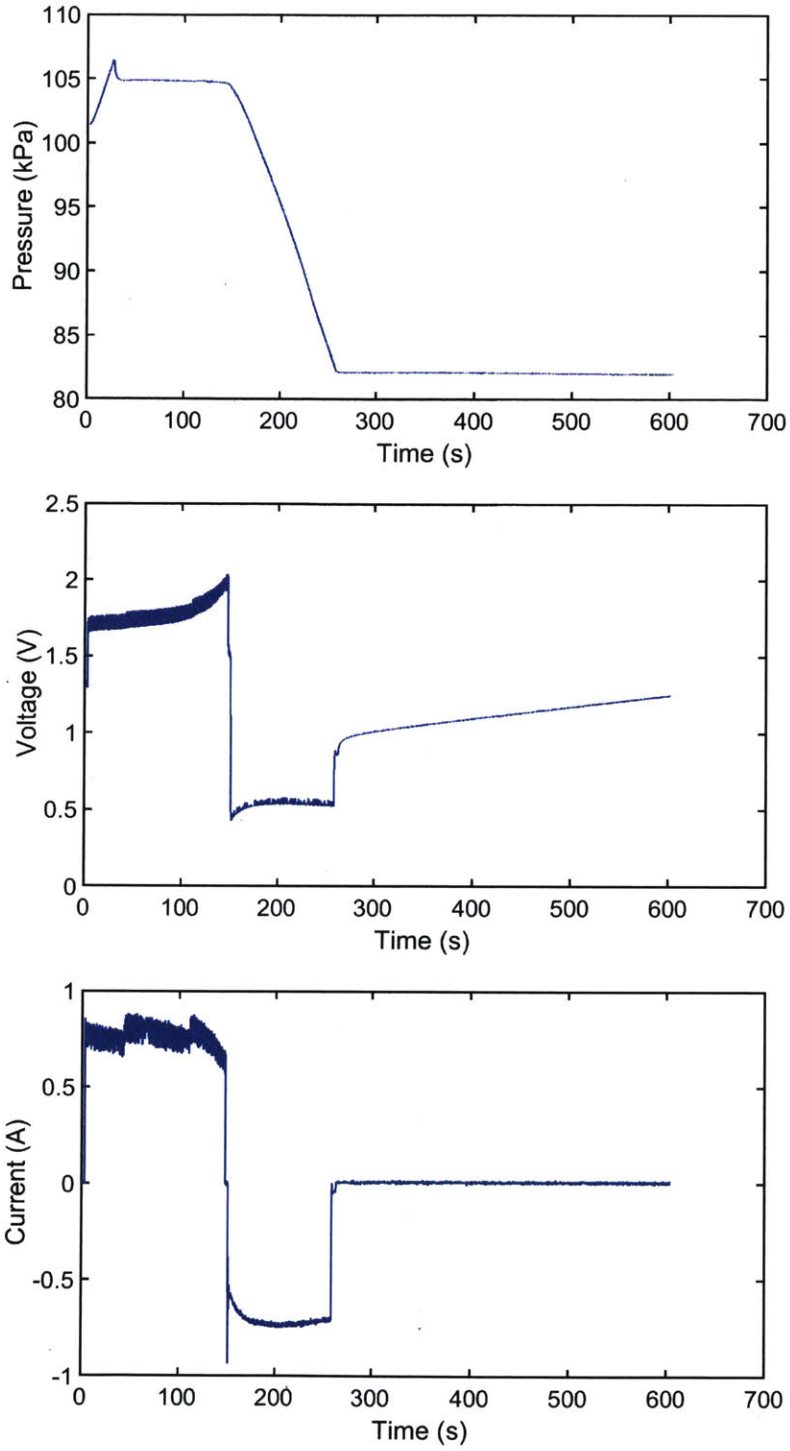

Figure 5-18: Experimental results of iteration 3 with energy recovery and check valve. Fuel cell was charged by battery via buck converter, and pump was continuously connected to the 20 mL wound volume phantom, and a check valve (design 2) was incorporated to allow for air to escape when bellows were expanding. In reverse pump operation, fuel cell was discharged via boost converter back to battery. Closed loop control to determine when the desired pressure was reached.

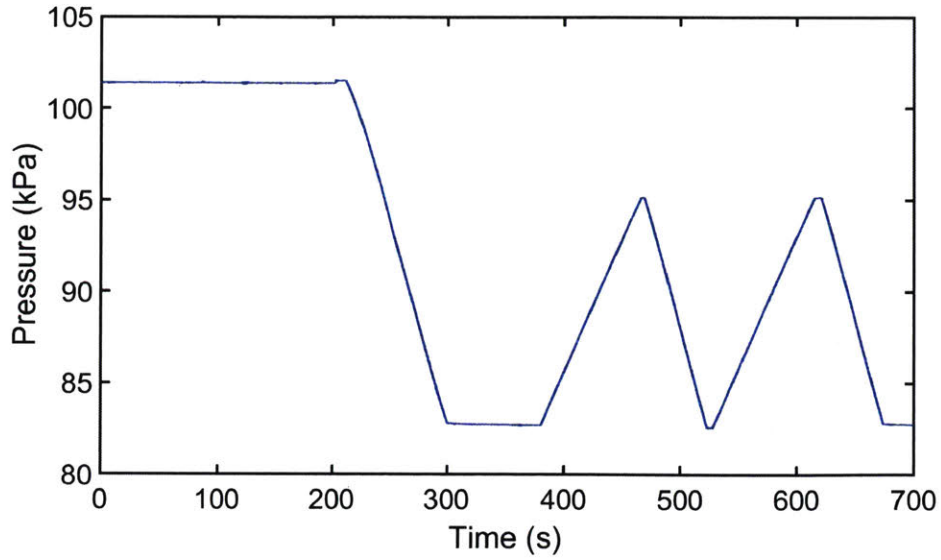

Figure 5-19: Variable Pressure operation of Bandage. Fuel cell was charged directly though a power supply and then pump was connected to a 20 mL wound volume phantom after it was fully inflated. In reverse pump operation, fuel cell was discharged through a bleed resistor. Closed loop control to determine when the desired pressure was reached and provide variable pressure.

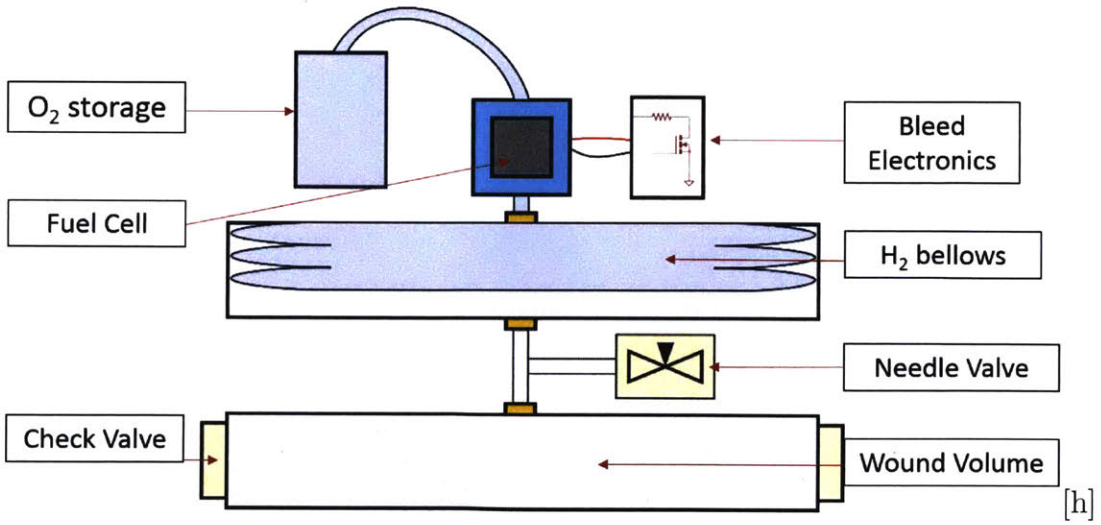

[h]

Figure 5-20: Experimental setup of iteration 3 at high leak rates. Fuel cell was charged by battery via buck converter, and pump was continuously connected to the 20 mL wound volume phantom and a needle valve to introduce a leak rate. A check valve (design 2) was incorporated to allow for air to escape when bellows were expanding. In reverse pump operation, fuel cell was discharged via boost converter back to battery. Closed loop control to determine when the desired pressure was reached.

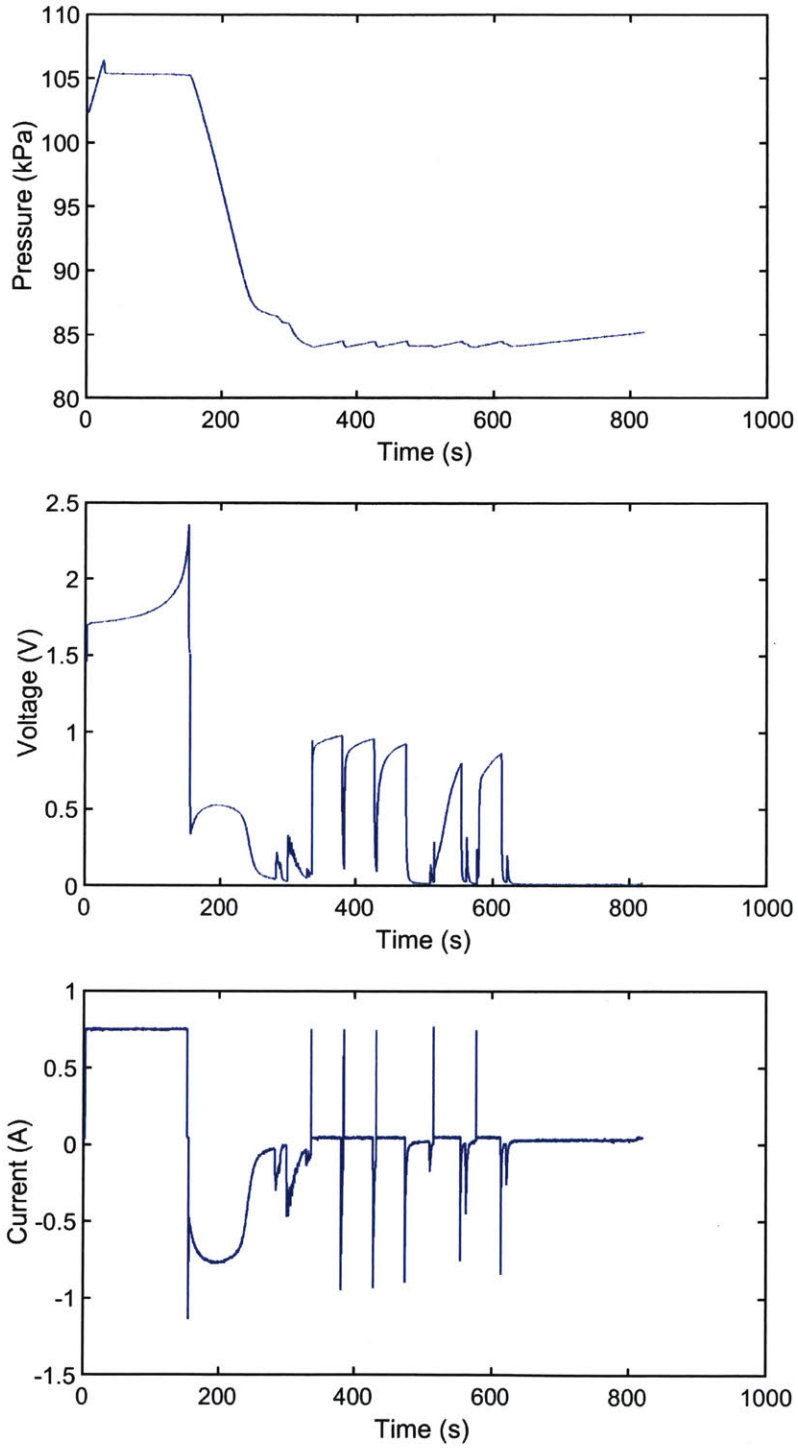

Figure 5-21: Experimental results of iteration 3 at high leak rates. Fuel cell was charged by battery via buck converter, and pump was contrinously connected to the 20 mL wound volume phantom and a needle valve to introduce a leak rate. A check valve (design 2) was incorporated to allow for air to escape when bellows were expanding. In reverse pump operation, fuel cell was discharged via boost converter back to battery. Closed loop control to determine when the desired pressure was reached.

Module Added	Base Case	Recovery Electronics	Check Valve	High Leak Rates
Final Pressure (kPa)	82.4 ± 0.23	**81.8 ± 0.47**	**82.4 ± 0.57**	**85.2 ± 2.84**
Total Charging Energy (J)	185 ± 16.7	191 ± 13.0	**199 ± 7.8**	198 ± 9.9
Recovered Energy (J)	0	**15.3 ± 1.0**	15.1 ± 1.4	15.9 ± 5.3
Net Energy (J)	185 ± 16.7	**161 ± 12.3**	**168 ± 8.7**	167 ± 18.6
Effective Pumping Rate ($\times 10^{-3}$ mL/s)	76.6 ± 16.8	73.3 ± 8.50	77.0 ± 6.00	**50.5 ± 7.12**
Variable Pressure Rate (kPa/s)	0.19 ± 0.04	0.18 ± .02	0.19 ± 0.02	**0.12 ± 0.02**
H_2 in reserver (mL at STP)	3.5 ± 2.35	**4.70 ± 0.38**	4.65 ± 0.53	4.93 ± 2.04
Maximum Mechanical Work (J)	0.110 ± 0.047	0.134 ± 0.007	0.133 ± 0.0011	0.138 ± 0.04
Net Energy of Round Trip (J)	185 ± 16.7	**152 ± 12.3**	**161 ± 9.29**	159.0 ± 18.2
Total Efficiency (%)	0.059 ± 0.023	**0.087 ± 0.006**	**0.082 ± 0.008**	0.087 ± 0.02

Table 5.2: Summary of results from iteration 3. Bolded values were statistically significant from the column preceding it ($p < 0.05$)

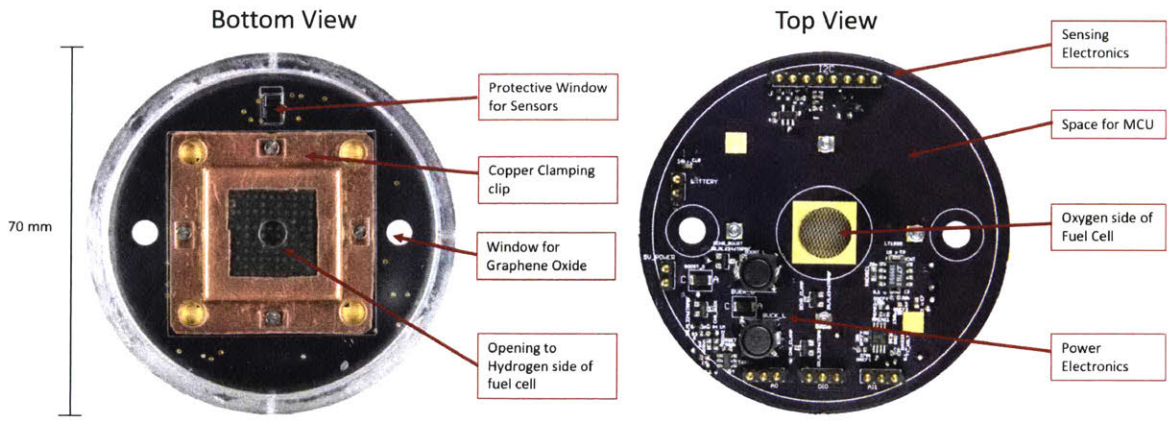

Figure 5-22: Final PCB board assembly for smart bandage. Board includes windows for Graphene Oxide integration, custom fuel cell clip, pressure and humidity sensing, as well as energy recovery switching circuitry

5.5 Work on future iterations

5.5.1 Integration onto a single PCB

A single PCB was constructed that now included integration of all power electronics needed for energy efficient operation of the fuel cell actuator. Space is still available for microcontroller operation in future iterations. This device was tested in expansion and contraction of the device to demonstrate that all modules could be functionally fit into a small, compact NPWT device.

5.5.2 Efficiency

While the device was able to reach desired pressures, the energy needed was higher than expected. Even with the energy recovery of the device, the best case overall efficiency of the device was approximately 0.09%, short of the goal of 0.6%. There are two large sources of inefficiency. First, there are area effects. Because the bellows is directly in contact with the bandage, with no vent to the atmosphere, it as if the contact area in Equation 2.32 is equal to the piston area in our model. This increases the theoretical work without energy recovery by an order of magnitude: from 0.04 J to approximately 0.5 J. Secondly, overpotentials in the actuator further increase the

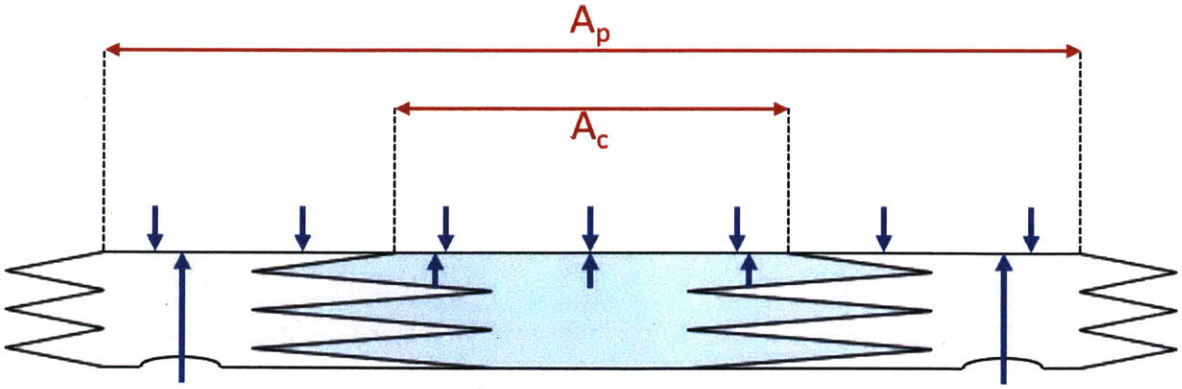

Figure 5-23: Nested Bellow Concept for electrolytic actuator. The electrolytic actuator now controls a smaller bellow that is nested in the larger bellow that is in contact with the wound site.

inefficiency, as the efficiency of charging ranged from 40-70% in charging, and 40-50% in discharging of the fuel cell. When coupled with the worst case inefficiencies of the recovery circuitry (40%), quite a bit of energy was never recovered from the device. This can be improved in future work by better PEM construction, as well as using our actuator in a more favorable regime.

5.5.3 Mechanical Amplifier

One source of inefficiency that could be improved is by reducing the amount of area, A_c, of the electrolytic actuator while still maintaining the larger pump area A_p. This will effectively be a nested bellow-in bellow system (see Figure 5-23). By having a smaller internal bellow (at a higher pressure) pushing the larger bellow, the amount of gas molecules needed to raise the bellow to height h_{max} is reduced. Remembering from chapter 3 that the pressure inside the actuator chamber can be solved to be

$$P_c(h)A_c = P_w(h)A_p - P_{atm}(A_p -_A c), \tag{5.3}$$

the number of moles of H_2 needed to reach a certain height when expanding will be

$$n_{H_2} = \frac{P_{check1}A_p + P_{atm}A_c}{RT} f_c h. \tag{5.4}$$

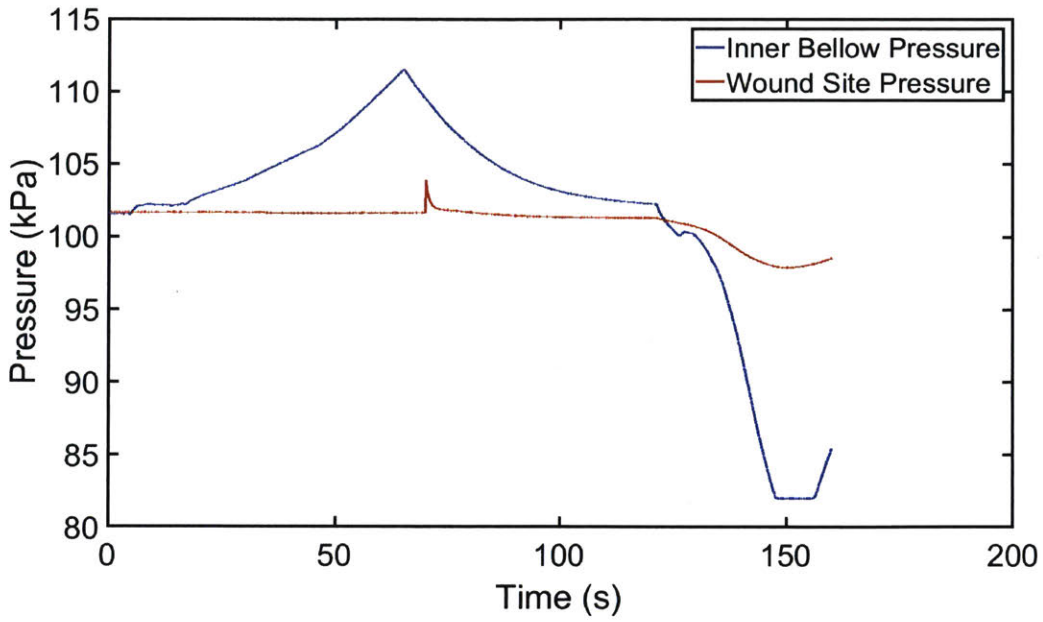

Figure 5-24: Results of nested bellow testing. The pressure of the inner bellow (blue) was much higher and lower than the pressure of the wound site (orange) during expansion and contraction, respectively. Some period after the pressure of the inner bellow dropped below the range of the pressure sensor, the seals in the nested bellow failed, resulting in an air leak and corresponding pressure increase.

Since the majority of energy is lost due to mechanical inefficiencies of the actuator, and poor energy recovery, reducing the amount of hydrogen gas necessary to be produced would improve efficiency of the device. This is similar to the concept explored in Chapter 2 regarding the contact area of the actuator. The smaller the contact area of the actuator, the less energy is needed to extend the actuator in the first place. To test this in practice, a nested bellows system in which the diameter of the inner bellow, D_c was half of the diameter of the outer bellow, D_p was constructed. This would result in an area ratio of 1:4. However, as can be seen from Figure 5-24, this design was unsuccessful in generating the negative pressure. As pressure of the inner bellow was reduced further and further, a failure in the bellow seals occurred, resulting in leakage of the device.

Possible reasons for this failure can be seen from the equations above. In the design, an ratio between the inner and outer bellow was approximately 1:4, meaning

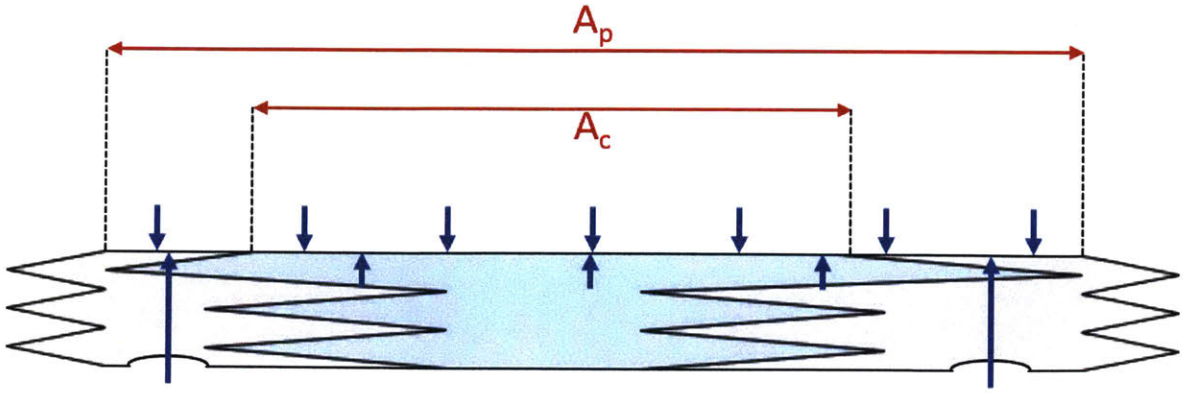

Figure 5-25: Nested Bellow Concept for electrolytic actuator. The electrolytic actuator now controls a smaller bellow that is nested in the larger bellow that is in contact with the wound site.

that inner bellow must reach an absolute pressure of 20 kPa. Additionally, a perfectly flat contact interface was assumed between the inner and outer bellow. If there is some lifting of the inner bellow, the contact area A_c will be much less than expected, limiting the amount of contact with actuator even further. The very low pressures needed to retract the actuator caused failure in the bellow seals.

Next, the inner bellow was changed to a conical shape, so that it had a much larger contact area, A_c, but a much smaller space filling efficiency f_c. This design (see Figure 5-25) would be able to reduce the amount of gas needed to expand the actuator, while avoiding the mechanical failures due to large pressure differentials. Unfortunately, this design was also unsuccessful, as seen in Figure 5-26.

This failure was slightly theorized to be due the dead space of the bellow. As seen from chapter 3, the maximum required extension of the bellow can be solved will be dependent on the initial height, h_0 and contact area, A_c of the inner bellow, as seen by:

$$h_{max} = \frac{P_{atm}V_w - P_{wdes}(V_w - A_p(f_p \frac{P_{atm}A_c}{P_{wdes}A_p - P_{atm}(A_p - Ac)} h_0))}{A_p(P_{wdes} - P_{atm}(1 - f_p))}. \tag{5.5}$$

The initial bellow height, h_0 was 1.5 mm, and the inner diameter of the conical bellow was 40 mm, meaning that the final height of the bellow when reducing pressure, h_f would be 2.8 mm, and the maximum bellow height, h_{max} must be 5.3 mm. Though the device was designed for a maximum extension of 6 mm, any imperfections in the

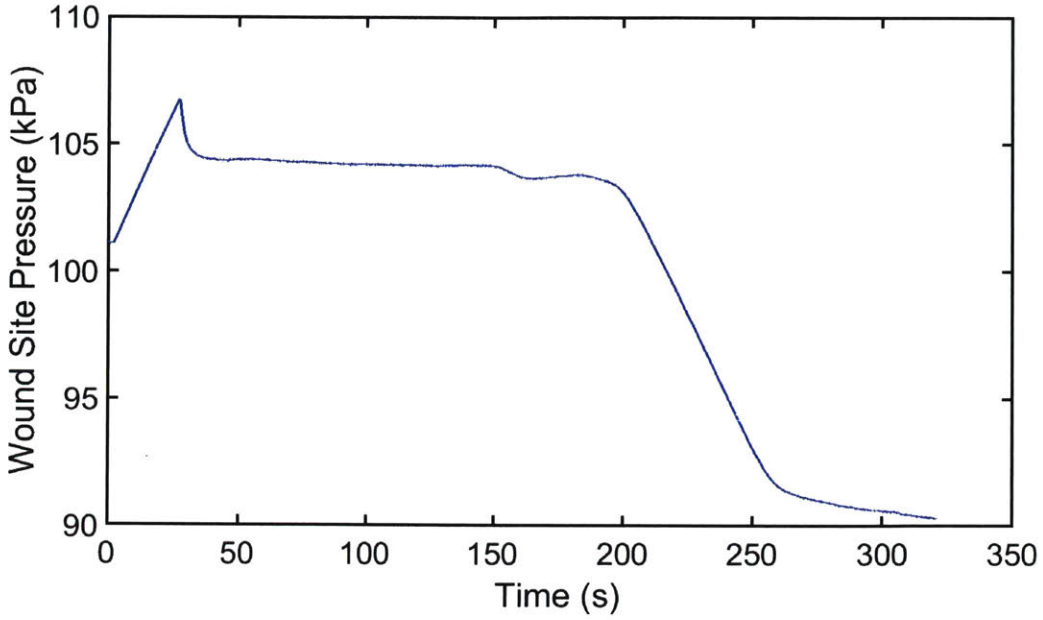

Figure 5-26: Results of nested conical bellow testing. The pressure of the wound site decreased to approximately 90 kPa, short of the desired pressure.

design or experiment that may prevent maximal extension would make it very difficult to reach the final pressure. Additionally, as the bellow is stretched, it is possible that A_c is further reduced, further limiting the possible retraction of the bellow. Further work in improvint the seals of the bellows mechanism will allow for more intricate bellow designs and implementation of this mechanical amplifier design.

Chapter 6

Conclusions

The aim of this work was to create a self-contained NPWT device. While there is still much work to do, the contributions in this thesis represent significant advances in NPWT design. First, a physical model of the wound bed was created to assess the pump and actuator requirements are necessary for self contained device. After no actuator was found to possess all the desired characteristics, an electrochemical actuator based on a reversible fuel cell was developed and characterized. Additionally, graphene oxide membranes were fabricated, tested, and added to the design to allow for fluid exudate handling. The final device was shown to be able to maintain to reach 82 kPa of pressure easily in no leak conditions, and was able to maintain 86 kPa of pressure in high leak rate conditions for 5 minutes at a time.

There is still much work to be done. With regards to NPWT applications, further work in improving the seals of the bellows will allow for more intricate bellows with higher space-filling efficiencies, and higher pressure ratings. This will allow for the implementation of the mechanical amplifier to further improve efficiency of the device. Additionally future work will focus on improving the current carrying capacity of the actuator, as well as improving charging/discharging efficiencies, which will result in higher power output and better electromechanical efficiencies of the actuator. Lastly, this actuator can be applied to many more applications, for example treatment of bed sores or portable delivery of insulin.

Chapter 7

Bibliography

[1] L. C. Argenta and M. J. Morykwas, "Vacuum-assisted closure: a new method for wound control and treatment: clinical experience.," 1997.

[2] M. J. Morykwas, L. C. Argenta, E. I. Shelton-Brown, and W. McGuirt, "Vacuum-assisted closure: A new method for wound control and treatment: animal studies and basic foundation," 1997.

[3] P. Blume, J. Walters, W. Payne, J. Ayala, and J. Lantis, "Comparison of Negative Pressure Wound Therapy Using Vacuum-Assisted Closure With Advanced Moist Wound Therapy in the Treatment of Diabetic Foot Ulcers A multicenter randomized controlled trial," *Diabetes Care*, vol. 31, no. 4, pp. 631–636, 2008.

[4] D. Mendonca, "Notice Warning Concerning," *Foot and Ankle International*, vol. 26, no. 9, pp. 761–766, 2005.

[5] GLEESON, LINDA and M. BOND, "Notice warning concerning copyright restrictions," *Wounds UK*, vol. 11, no. 2, 2015.

[6] H. E. Itani, "Notice warning concerning copyright restrictions," *British journal of community nursing*, vol. 20, no. 6, pp. S28–34, 2015.

[7] A. Bruhin, F. Ferreira, M. Chariker, J. Smith, and N. Runkel, "Systematic review and evidence based recommendations for the use of Negative Pressure Wound Therapy in the open abdomen," *International Journal of Surgery*, vol. 12, no. 10, pp. 1105–1114, 2014.

[8] N. K. Kanakaris, C. Thanasas, N. Keramaris, G. Kontakis, M. S. Granick, and P. V. Giannoudis, "The efficacy of negative pressure wound therapy in the management of lower extremity trauma: review of clinical evidence.," *Injury*, vol. 38 Suppl 5, pp. S9–18, dec 2007.

[9] C. Huang, T. Leavitt, L. R. Bayer, and D. P. Orgill, "Effect of negative pressure wound therapy on wound healing.," *Current problems in surgery*, vol. 51, pp. 301–31, jul 2014.

[10] J. Folkman and A. Moscona, "Role of cell shape in growth control," *Nature*, vol. 273, pp. 345–349, jun 1978.

[11] M. Heil and W. Schaper, "Influence of mechanical, cellular, and molecular factors on collateral artery growth (Arteriogenesis)," *Circulation Research*, vol. 95, no. 5, pp. 449–458, 2004.

[12] M. J. Morykwas, B. J. Faler, D. J. Pearce, and L. C. Argenta, "Effects of varying levels of subatmospheric pressure on the rate of granulation tissue formation in experimental wounds in swine," *Annals of Plastic Surgery*, vol. 47, no. 5, pp. 547–551, 2001.

[13] Smith & Nephew, "PICO Single use NPWT System."

[14] Kinetic Concpets, Inc., "V.A.C.ULTA Negative Pressure Wound Therapy System."

[15] Acelity L.P. Inc., "SNAP Therapy System," 2018.

[16] D. R. Zurovcik, *Development of a simplified negative pressure wound device.* Phd thesis, MIT, 2007.

[17] C. K. Sen, G. M. Gordillo, S. Roy, R. Kirsner, L. Lambert, T. K. Hunt, F. Gottrup, G. C. Gurtner, and M. T. Longaker, "Human skin wounds: a major and snowballing threat to public health and the economy.," *Wound repair and regeneration : official publication of the Wound Healing Society [and] the European Tissue Repair Society*, vol. 17, pp. 763–71, jan.

[18] O. Borgquist, R. Ingemansson, and M. Malmsjö, "The effect of intermittent and variable negative pressure wound therapy on wound edge microvascular blood flow.," *Ostomy/wound management*, vol. 56, no. 3, pp. 60–7, 2010.

[19] P. Dastouri, D. L. Helm, S. S. Scherer, G. Pietramaggiori, G. Younan, and D. P. Orgill, "Waveform modulation of negative-pressure wound therapy in the murine model," *Plastic and Reconstructive Surgery*, vol. 127, no. 4, pp. 1460–1466, 2011.

[20] S. S. Scherer, G. Pietramaggiori, J. C. Mathews, and D. P. Orgill, "Short periodic applications of the vacuum-assisted closure device cause an extended tissue response in the diabetic mouse model," *Plastic and Reconstructive Surgery*, vol. 124, no. 5, pp. 1458–1465, 2009.

[21] G. E. Glass and J. Nanchahal, "The methodology of negative pressure wound therapy: Separating fact from fiction," *Journal of Plastic, Reconstructive and Aesthetic Surgery*, vol. 65, no. 8, pp. 989–1001, 2012.

[22] S. G. Goss, J. A. Schwartz, F. Facchin, E. Avdagic, C. Gendics, and J. C. Lantis, "Negative pressure wound therapy with instillation (NPWTi) better reduces post-debridement bioburden in chronically infected lower extremity wounds than NPWT alone," *Journal of the American College of Clinical Wound Specialists*, vol. 4, no. 4, pp. 74–80, 2012.

[23] K. L. Derrick and M. C. Lessing, "Genomic and Proteomic Evaluation of Tissue Quality of Porcine Wounds Treated With Negative Pressure Wound Therapy in Continuous , Noncontinuous , and Instillation Modes," *Eplasty*, vol. 14, p. e43, 2014.

[24] L. A. Schneider, A. Korber, S. Grabbe, and J. Dissemond, "Influence of pH on wound-healing: A new perspective for wound-therapy?," *Archives of Dermatological Research*, vol. 298, no. 9, pp. 413–420, 2007.

[25] M. A. Khan, U. Ansari, and M. N. Ali, "Real-time wound management through integrated pH sensors: a review," *Sensor Review*, vol. 35, no. 2, pp. 183–189, 2015.

[26] T. R. Dargaville, B. L. Farrugia, J. A. Broadbent, S. Pace, Z. Upton, and N. H. Voelcker, "Sensors and imaging for wound healing: A review," *Biosensors and Bioelectronics*, vol. 41, no. 1, pp. 30–42, 2013.

[27] N. Mehmood, A. Hariz, R. Fitridge, and N. H. Voelcker, "Applications of modern sensors and wireless technology in effective wound management," *Journal of Biomedical Materials Research - Part B Applied Biomaterials*, vol. 102, no. 4, pp. 885–895, 2014.

[28] S. D. Milne, P. Connolly, H. A. Hamad, and I. Seoudi, "Development of wearable sensors for tailored patient wound care," *2014 36th Annual International Conference of the IEEE Engineering in Medicine and Biology Society, EMBC 2014*, pp. 618–621, 2014.

[29] H. J. Sismaet, A. Banerjee, S. McNish, Y. Choi, M. Torralba, S. Lucas, A. Chan, V. K. Shanmugam, and E. D. Goluch, "Electrochemical detection of Pseudomonas in wound exudate samples from patients with chronic wounds," *Wound Repair and Regeneration*, vol. 24, no. 2, pp. 366–372, 2016.

[30] D. Sharp, P. Gladstone, R. B. Smith, S. Forsythe, and J. Davis, "Approaching intelligent infection diagnostics: Carbon fibre sensor for electrochemical pyocyanin detection," *Bioelectrochemistry*, vol. 77, no. 2, pp. 114–119, 2010.

[31] D. A. Hudson, K. G. Adams, A. Van Huyssteen, R. Martin, and E. M. Huddleston, "Simplified negative pressure wound therapy: Clinical evaluation of an ultraportable, no-canister system," *International Wound Journal*, vol. 12, no. 2, pp. 195–201, 2015.

[32] K. D. Fong and W. A. Marston, "SNaP Wound Care System: Ultraportable Mechanically Powered Negative Pressure Wound Therapy," *Advances in Wound Care*, vol. 1, no. 1, pp. 41–43, 2012.

[33] C. Payne and D. Edwards, "Application of the Single Use Negative Pressure Wound Therapy Device (PICO) on a Heterogeneous Group of Surgical and TraumaticWounds," *Eplasty*, vol. 14, no. e20, pp. 152–166, 2014.

[34] K. D. Fong, D. Hu, S. Eichstadt, D. M. Gupta, M. Pinto, G. C. Gurtner, M. T. Longaker, and H. P. Lorenz, "The SNaP system: Biomechanical and animal model testing of a novel ultraportable negative-pressure wound therapy system," *Plastic and Reconstructive Surgery*, vol. 125, no. 5, pp. 1362–1371, 2010.

[35] M. Malmsjö, E. Huddleston, and R. Martin, "Biological effects of a disposable, canisterless negative pressure wound therapy system.," *Eplasty*, vol. 14, no. August, p. e15, 2014.

[36] C. Moffat, "The experience of patients with complex wounds and the use of NPWT in a home-care setting," *Journal of wound care*, vol. 20, no. 11, pp. 512–16, 2011.

[37] J. R. Burke, R. Morley, and M. Khanbhai, "Using portable negative pressure wound therapy devices in the home care setting," *Smart Homecare Technology and TeleHealth*, vol. 2, pp. 129–135, 2014.

[38] G. Spentzouris and N. Labropoulos, "The evaluation of lower-extremity ulcers," *Seminars in Interventional Radiology*, vol. 26, no. 4, pp. 286–295, 2009.

[39] J. Kantor and D. J. Margolis, "A multicentre study of percentage change in venous leg ulcer area as a prognostic index of healing at 24 weeks," *British Journal of Dermatology*, vol. 142, no. 5, pp. 960–964, 2000.

[40] M. Forlee, A. Rossington, and R. Searle, "A prospective, open, multicentre study to evaluate a new gelling fibre dressing containing silver in the management of venous leg ulcers," *International Wound Journal*, vol. 11, no. 4, pp. 438–445, 2014.

[41] S. Thomas, M. Fear, and J. Humphreys, "The effect of dressings on the production of exudate from venous leg ulcers," *Wounds*, vol. 8, pp. 145–150, jan 1996.

[42] T. Hurd, P. Trueman, and A. Rossington, "Use of a portable, single-use negative pressure wound therapy device in home care patients with low to moderately exuding wounds: a case series.," *Ostomy/wound management*, vol. 60, pp. 30–6, mar 2014.

[43] H. Birke-Sorensen, M. Malmsjo, P. Rome, D. Hudson, E. Krug, L. Berg, A. Bruhin, C. Caravaggi, M. Chariker, M. Depoorter, C. Dowsett, R. Dunn, F. Duteille, F. Ferreira, J. F. Martínez, G. Grudzien, S. Ichioka, R. Ingemansson, S. Jeffery, C. Lee, S. Vig, N. Runkel, R. Martin, J. Smith, and J. Smith, "Evidence-based recommendations for negative pressure wound therapy: Treatment variables (pressure levels, wound filler and contact layer) Steps towards an international consensus," *Journal of Plastic, Reconstructive & Aesthetic Surgery*, vol. 64, pp. S1–S16, sep 2011.

[44] S. Batacchi, S. Matano, A. Nella, G. Zagli, M. Bonizzoli, A. Pasquini, V. Anichini, V. Tucci, G. Manca, K. Ban, A. Valeri, and A. Peris, "Vacuum-assisted closure device enhances recovery of critically ill patients following emergency surgical procedures," *Critical Care*, vol. 13, no. 6, pp. 1–8, 2009.

[45] Kinetic Concpets, Inc., "V.a.c.via negative pressure wound therapy system."

[46] Parker Hannifin, "T2-05 Datasheet."

[47] KNF, "Micro Diaphragm Gas Sampling Pumps With High Performance," pp. 3–5.

[48] Bartels Mikrotechnik, "Bartels Micropumps Datasheet," 2014.

[49] B. N. Persson and C. Yang, "Theory of the leak-rate of seals," *Journal of Physics Condensed Matter*, vol. 20, no. 31, 2008.

[50] J. M. Hollerbach, I. Hunter, and J. Ballantyne, "A comparative analysis of actuator technologies for robotics," 1991.

[51] Parker Hannifin, "O-Ring Handbook," 2001.

[52] C. G. Cameron and M. S. Freund, "Electrolytic actuators: Alternative, high-performance, material-based devices," *Proceedings of the National Academy of Sciences*, vol. 99, no. 12, pp. 7827–7831, 2002.

[53] R. Sheybani, H. Gensler, and E. Meng, "A MEMS electrochemical bellows actuator for fluid metering applications," *Biomedical Microdevices*, vol. 15, no. 1, pp. 37–48, 2013.

[54] F. Barbir, *PEM Fuel Cells Theory and Practice.* 2013.

[55] Horizon Fuel Cells, "PEM Reversible Fuel Cell."

[56] Smooth-On Industries, "Ecoflex series sSuper-soft Additon Cure Silicone Rubbers."

[57] G. D. Winter, "Formation of the scab and the rate of epithelization of superficial wounds in the skin of the young domestic pig," *Nature*, vol. 193, no. 4812, pp. 293–294, 1962.

[58] G. D. Winter, "Effect of Air Exposure and Occlusion on Experimental Human Skin Wounds," *Nature*, vol. 200, no. 4904, pp. 378–379, 1963.

[59] D. Queen, J. D. Gaylor, J. H. Evans, J. M. Courtney, and W. H. Reid, "The preclinical evaluation of the water vapour transmission rate through burn wound dressings.," *Biomaterials*, vol. 8, no. 5, pp. 367–71, 1987.

[60] R. Xu, H. Xia, W. He, Z. Li, J. Zhao, B. Liu, Y. Wang, Q. Lei, Y. Kong, Y. Bai, Z. Yao, R. Yan, H. Li, R. Zhan, S. Yang, G. Luo, and J. Wu, "Controlled water vapor transmission rate promotes wound-healing via wound re-epithelialization and contraction enhancement," *Scientific Reports*, vol. 6, no. March, pp. 1–12, 2016.

[61] Basf SE, "Thermoplastic Polyurethane Elastomers Elastollan ® Material Properties."

[62] R. R. Nair, H. A. Wu, P. N. Jayaram, I. V. Grigorieva, and A. K. Geim, "Unimpeded permeation of water through helium-leak-tight graphene-based membranes," *Science*, vol. 335, no. 6067, pp. 442–444, 2012.

[63] Y. Su, V. G. Kravets, S. L. Wong, J. Waters, A. K. Geim, and R. R. Nair, "Impermeable barrier films and protective coatings based on reduced graphene oxide," *Nature Communications*, vol. 5, 2014.

[64] S. Pei and H. M. Cheng, "The reduction of graphene oxide," *Carbon*, vol. 50, no. 9, pp. 3210–3228, 2012.

[65] B. Rezania, N. Severin, A. V. Talyzin, and J. P. Rabe, "Hydration of bilayered graphene oxide," *Nano Letters*, vol. 14, no. 7, pp. 3993–3998, 2014.

[66] M. Nasrollahzadeh, F. Babaei, P. Fakhri, and B. Jaleh, "Synthesis, characterization, structural, optical properties and catalytic activity of reduced graphene oxide/copper nanocomposites," *RSC Adv.*, vol. 5, pp. 10782–10789, jan 2015.

[67] W. S. Hummers and R. E. Offeman, "Preparation of Graphitic Oxide," *Journal of the American Chemical Society*, vol. 80, pp. 1339–1339, mar 1958.

[68] D. A. Dikin, S. Stankovich, E. J. Zimney, R. D. Piner, G. H. B. Dommett, G. Evmenenko, S. T. Nguyen, and R. S. Ruoff, "Preparation and characterization of graphene oxide paper," *Nature*, vol. 448, no. 7152, pp. 457–460, 2007.

[69] R. K. Joshi, P. Carbone, F. C. Wang, V. G. Kravets, A. K. Geim, and R. R. Nair, "Precise and Ultrafast Molecular Oxide Membranes," *Science*, vol. 343, no. February, pp. 752–755, 2014.

[70] C. N. Yeh, K. Raidongia, J. Shao, Q. H. Yang, and J. Huang, "On the origin of the stability of graphene oxide membranes in water," *Nature Chemistry*, vol. 7, no. 2, pp. 166–170, 2015.

[71] A. A. King, B. R. Davies, N. Noorbehesht, P. Newman, T. L. Church, A. T. Harris, J. M. Razal, and A. I. Minett, "A new raman metric for the characterisation of graphene oxide and its derivatives," *Scientific Reports*, vol. 6, pp. 1–6, 2016.

[72] A. C. Ferrari, "Raman spectroscopy of graphene and graphite: Disorder, electron-phonon coupling, doping and nonadiabatic effects," *Solid State Communications*, vol. 143, no. 1-2, pp. 47–57, 2007.

[73] A. C. Ferrari and D. M. Basko, "Raman spectroscopy as a versatile tool for studying the properties of graphene," *Nature Nanotechnology*, vol. 8, no. 4, pp. 235–246, 2013.

[74] S. Stankovich, D. A. Dikin, R. D. Piner, K. A. Kohlhaas, A. Kleinhammes, Y. Jia, Y. Wu, S. B. T. Nguyen, and R. S. Ruoff, "Synthesis of graphene-based nanosheets via chemical reduction of exfoliated graphite oxide," *Carbon*, vol. 45, no. 7, pp. 1558–1565, 2007.

[75] B. N. Persson and C. Yang, "Theory of the leak-rate of seals," *Journal of Physics Condensed Matter*, vol. 20, no. 31, 2008.